Modeling fundamental plasma transport and particle-induced emission in a simplified Test Cell

by

Paul Nicholas Giuliano

A dissertation submitted in partial fulfillment
of the requirements for the degree of
Doctor of Philosophy
(Aerospace Engineering)
in the University of Michigan
2013

Doctoral Committee:

Professor Iain D. Boyd, Chair
Professor Alec Gallimore
Professor Mark Kushner
Justin Koo, Air Force Research Laboratory

Songs of Distant Earth (1986)

The world is like a ride in an amusement park and when you choose to go on it you think it's real because that's how powerful our minds are. The ride goes up and down, around and around; it has thrills and chills and it's very brightly colored and it's very loud and it's fun... for a while. Many people have been on the ride a long time and they begin to wonder, "Hey, is this real, or is this just a ride?" And other people have remembered and they come back to us and say, "Hey, don't worry; don't be afraid, ever, because this is just a ride." ... and we kill those people.

– Bill Hicks, *Revelations (1993)*

For Jaclyn

and for Grandpa and Papa.

ACKNOWLEDGEMENTS

First and foremost, I would like to thank my advisor, Prof. Iain Boyd, for all of his guidance, oversight, and patience during my time here at Michigan. Iain entrusted me to this research task within the large, collaborative MACEEP effort, throwing me in the deep end and allowing me to learn and mature through my failures and successes. It is astounding to think of how much knowledge I have acquired in the fields of rarefied gas dynamics, plasma physics, electric propulsion, and high performance computing under his supervision; now, as I am nearing the end, I am appreciative of it more than ever.

My committee members also deserve a major acknowledgement. Whether it was a conversation on research ideas/direction, an exciting MIPSE lecture, or an entire class on plasma propulsion or processes, my education in plasma science and engineering is most definitely attributed to the efforts of Profs. Gallimore and Kushner. Furthermore, something so simple as a weekly fifteen minute phone call with Dr. Justin Koo at Edwards AFB was enough to always keep me on track and second-guessing any of the recently-made assumptions of which I was so confident those fifteen minutes earlier. I am thankful that these committee members did exactly what I hoped for in a committee: they kept me on my toes as well as expanded my knowledge and appreciation for the fundamentals and diversity of my field.

No Aerospace Engineering dissertation is complete without the acknowledgement

of Denise, Cindy, Dave, and the rest of of the department's administrative and technical staff who often take care of issues that would otherwise cause many headaches.

I would like to extend my gratitude to the members of the Plasma & Space Propulsion Laboratory at UCLA, namely Prof. Wirz and his graduate students, Marlene, Lauren, and Jun, for being great collaborators in this joint research effort. Not only was the UCLA lab responsive to emails and phone calls but they truly believed in the collaborative, supportive relationship which is so important in this type of project. I wish them the best of luck in their endeavors with the Test Cell and future projects.

My experience at Michigan would not have been the same if it were not for the wonderful friendships I have made both in and out of NGPDL. I would like to start by giving a nod to Tyler, Kentaro, Brandon, Maria, and Horatiu, the other electric propulsion computationalists in NGPDL with whom I have had many an insightful conversation. We started as the minority but it seems as though we are growing every year. Also, I hope that Cyril and Kelly are able to take MONACO-PIC to new and greater heights (without too much spilled blood). Outside of NGPDL, there are too many names for a list so I will simply acknowledge that if it were not for the Michigan Delta Chi Chapter, LPWC, Aero Scotch Club, Aero Wine Club, Aero Trivia Group, and (my favorite) Aero Drunks, my life would have been infinitely less interesting over the past four and a half years.

My extended family has provided the well-needed encouragement through all of the ups and downs over these years. Not only have we grown through our experiences and successes during my time here in Ann Arbor but we have undergone the painful process of loss. This acknowledgment is also directed to all of the friends throughout my life who have stayed close through the good and bad. Sometimes family and

friends are the only ones who are crazy enough to understand exactly what you need.

Last but certainly not least, I would like to thank my wife, Jaclyn, for her undying support and unconditional love throughout the various phases of life that we have traversed together. It is extremely comforting when you realize that your co-pilot in life is the perfect person for the job.

PREFACE

This work involves the modeling of fundamental plasma physics processes occurring within environments that are similar to that of the discharge and plume regions of electric propulsion devices such as Hall effect thrusters. The research is conducted as a collaborative effort with the Plasma & Space Propulsion Laboratory at the University of California, Los Angeles (UCLA), as part of the University of Michigan/AFRL Center for Excellence in Electric Propulsion (MACEEP).

Transport physics, such as particle-particle collisions and particle-induced electron emission, are simulated within the UCLA experimental facility and its representative electric propulsion environment. Simulation methods employed include the direct simulation Monte Carlo (DSMC) and particle-in-cell (PIC) techniques for the kinetic simulation of charged, rarefied species on high-performance computing architectures.

Momentum- (MEX) and charge-exchange (CEX) collision cross-section models for Xe and Xe^+, both total and differential, are successfully validated at collision energies of 1.5 keV within the novel facility. Heavy-species collisional transport models are validated and the importance of scattering anisotropy in this collision-dominated environment is shown. The theory of particle-induced electron emission (PIE) is then investigated in the context of the relevant energies and environments of the UCLA facility and electric propulsion devices and diagnostics. Reduced, semi-empirical models for total yield and emitted electron energy distribution functions that are easily implemented in a DSMC-PIC code are developed for the simulation of secondary-electron emission due to low-energy ions and high-energy atoms, even in the case of

incomplete target-material information.

These models are important for the characterization of electric propulsion devices due to the problematic nature of low-temperature plasma diagnostic techniques in which the emission of electrons is physically indistinguishable from the collection of ions.

TABLE OF CONTENTS

LIST OF FIGURES

Figure

LIST OF TABLES

Table

LIST OF APPENDICES

Appendix

LIST OF ABBREVIATIONS

CEX	charge exchange
DSA	Data Set A
DSB	Data Set B
DSC	Data Set C
DSD	Data Set D
DSMC	direct simulation Monte Carlo
EP	electric propulsion
EEDF	electron energy distribution function
EO	Exit Orifice
EP	Exit Plate
HET	Hall effect thruster
IC	Inner Cylinder
KE	kinetic emission
KE EEDF	kinetically emitted electron energy distribution function
MEX	momentum exchange
MCC	Monte Carlo collision
NTC	No-Time-Counter
PIC	particle-in-cell
PIE	particle-induced electron emission
PE	potential emission
PE EEDF	potentially emitted electron energy distribution function

SEE	secondary electron emission
SPT	stationary plasma thruster
SDOS	surface density-of-states
TAL	thruster with anode layer
UP	Upstream Plate
VHS	Variable Hard Sphere

LIST OF NOMENCLATURE

α	accommodation coefficient
σ	cross-section
λ_D	Debye length
$\mathrm{d}\sigma/\mathrm{d}\Omega$	differential cross-section
ϕ	electric potential
$\vec{E}$	electric field
E	translational energy
ϵ_F	Fermi energy
q	elementary charge
m	element mass
g_0	gravitational acceleration at sea-level
b	impact parameter
$V(r)$	inter-atomic potential structure
Z	ion charge number
n_i	ion number density
μ	ion reduced mass as protons
Kn	Knudsen number
W_c	local cell weight
λ	mean free path
ω_p	plasma frequency
W_p	relative macroparticle weight

g_r	relative velocity
I_{sp}	specific impulse
$\rho(E)$	SDOS
W_ϕ	surface work function
Δt	time step
γ	total yield
ΔV	velocity requirement

CHAPTER I

Introduction

The purpose of this chapter is to provide motivation and background concepts for the present work. The chapter will then summarize this dissertation's objectives and provide the organizational structure of the thesis.

1.1 Motivation

Electric propulsion (EP) refers to spacecraft propulsion devices which produce thrust via electric power as opposed to a chemical-based process. While generally having lower thrust densities compared to their chemical counterparts, electric propulsion systems hold the advantage of having a higher specific impulse (I_{sp}) making them an integral aspect of missions with high velocity requirement (ΔV) or strict payload limits. Recent high-profile missions and projects, such as SMART-1 [17], DAWN [18], GOCE [19], and VASIMR [20], have presented electric propulsion systems as primary propulsion systems. Due to their increasing role in missions, the need to fully characterize electric propulsion devices in both ground- and space-based facilities is also increasing. The expensive nature of both ground- and space-testing gives support for the importance of numerical simulation as a supplement to experimental characterization efforts. Numerical simulation has the advantage of being much cheaper and quicker than experimental testing. However, accurate models used to simulate the

complex physics of EP discharges and plumes are still not fully developed; proving their physical accuracy is often a difficult process.

In particular, the Hall effect thruster (HET) is an electric propulsion device which has shown considerable promise. Certain details of HET operation, however, are unknown and related to the fundamental transport physics of various species within the device. The theory behind transport of heavy species (often noble gases) and electrons in the discharge region of HETs still relies on assumptions which have not been very well-refined in the past half-century [21, 22]. In addition, disparities have been found in experimental measurements of HET plumes depending on whether or not operation is in a ground facility or on a spacecraft [2] or whether or not secondary electron emission is accounted for correctly in the diagnostics [23]. The inability to resolve these physics are directly related to efficiency and lifetime factors for electric propulsion devices as well as other spacecraft hardware directly impacted by thruster operation. These unknown factors translate to higher mission cost and are a detriment to the practical, wide-scale use of electric propulsion systems.

The present work is motivated by these unknowns in HET operation and utilizes a numerical approach to investigate the related physics. The numerical models presented in this dissertation have proven to be effective in the simulation of similar plasma physics on a device-level scale [15] but are unique in that they are scaled down to a more fundamental environment so that their accuracies and sensitivities can be more closely evaluated. In addition, the complement of an ongoing experimental effort at the University of California, Los Angeles (UCLA), has led to a collaborative effort to understand these physical phenomena in full by comparing results obtained with numerical models to physical measurements. As HETs become the primary electric propulsion system of choice for more space missions, it is important to interrogate and validate all models used in the simulation of the devices so that we may build a better understanding of their fundamental physics.

1.2 Background

This section will provide background information and context on the topics of electric propulsion (EP), Hall effect thrusters (HETs), the experimental facility of interest, and the physical models under investigation.

1.2.1 Electric propulsion and the rocket equation

Spacecraft propulsion devices operate on the principle of Newton's Third Law of motion [24], commonly written in terms of spacecraft parameters as

$$m\frac{\mathrm{d}V}{\mathrm{d}t} = \dot{m}U_e \ , \tag{1.1}$$

with the left hand side representing spacecraft mass and acceleration and the right hand side representing propellant flow rate ($\dot{m}$) and exit velocity (U_e) combined to equal thrust. Replacing $\dot{m}$ with $\mathrm{d}m/\mathrm{d}t$ and integrating gives the classical rocket equation for a simple spacecraft [25, 26],

$$\frac{m_f}{m_0} = e^{-\Delta V/U_e} \ , \tag{1.2}$$

with the left hand side now representing the final propellant mass-fraction of the spacecraft and the exponential term on the right hand side containing the ratio of ΔV to propellant exit velocity. This relationship is commonly thought of as a performance characterization of the propulsion system as, for a given ΔV, an increase in propellant exit velocity results in less required propellant mass.

Referenced earlier, I_{sp} is a parameter which describes the efficiency of propulsion systems, representing the ratio of thrust to propellant weight flow rate,

$$I_{sp} = \frac{U_e}{\dot{m}g_0} \ , \tag{1.3}$$

using 9.81 m/s^2 for gravitational acceleration at sea-level (g_0). This relationship attempts to normalize all propulsion systems and their respective propellant types by their flow rate and is measured in the unit of seconds. This normalization is important as I_{sp} is then directly inserted into Equation 1.2 for an unbiased propulsion efficiency.

1.2.2 Types of electric propulsion devices

EP devices are commonly categorized as electrothermal, electrostatic, or electromagnetic [1], as illustrated in Figure 1.1. These categories refer to the primary mechanism used to accelerate the propellant to create thrust:

1. *Electrothermal* devices directly heat the propellant using an electric discharge or radiative process, shown in Figure 1.1(a). Similar to chemical propulsion methods, the resulting thermal energy is directed into kinetic energy using a nozzle. Electrothermal devices are typically the simplest from an integration standpoint as they only rely on a heating mechanism and no electromagnetic devices despite still posing a significant spacecraft contamination issue due to the plume. However, electrothermal devices provide the lowest magnitude and range of I_{sp} options. The most common electrothermal electric propulsion devices are resistojets and arcjets.

2. *Electrostatic* devices use a static electric field to accelerate charged propellant particles to the exit of the device, shown in Figure 1.1(b). Magnetic fields are often used to contain electrons in regions of ionization while keeping ions unmagnetized. However, it is the electric field which is the primary source of acceleration, such as in the case of ion thrusters or HETs. Electrostatic thrusters are a popular choice of electric propulsion device for various mission types due to their reliability, throttle ability, and efficiency. However in certain cases, such as in the ion thruster design, there are space-charge limitations which cause a plateau in device performance.

3. *Electromagnetic* devices use the Lorentz force resulting from crossed electric and magnetic fields to accelerate charged propellant particles to the exit of the device, shown in Figure 1.1(c). Electromagnetic thrusters have the advantage of accelerating both ions and electrons in the same Lorentz-force direction, leading to an exhaust which requires no neutralization. However, electromagnetic devices have performance-limiting instabilities which prevent them from achieving high powers based on predictions using state of the art physical models [27]. Examples of electromagnetic thrusters are pulsed-plasma thrusters and magnetoplasmadynamic thrusters.

1.2.3 The Hall effect thruster (HET)

HETs originated in the 1950s and 1960s in both the United States and the Soviet Union and have become a primary focus of electric propulsion research [28] due to their high efficiencies, throttle ability, and reliability. A schematic of a typical HET can be seen in Figure 1.2(a) with its axisymmetric construction and configuration of cathode and anode seen in the photograph of Figure 1.2(b).

The HET is comprised of an extended annulus with an anode at the upstream-end and a cathode externally mounted at the downstream-end; this region all-together is called the acceleration channel. Neutral propellant, typically a noble gas, is injected at the anode and ionized into a plasma within the acceleration channel. At the downstream end of the channel, a cathode emits electrons which *i*) act to neutralize the final plume, *ii*) travel to the anode to complete the circuit, or *iii*) remain trapped in the high-magnetic field region at the exit of the channel. The magnetic field is designed in a special way to trap electrons in this manner yet leave ions unmagnetized [29]. The trapped electrons establish a potential difference which accelerates the ions to the exit. These electrons also drift in the azimuthal direction and form the phenomenon which is the namesake of the device, the Hall current [30].

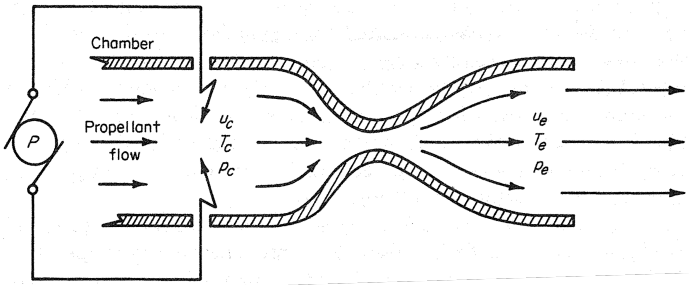

(a) Electrothermal acceleration of propellant through a nozzle which has been previously heated electrically.

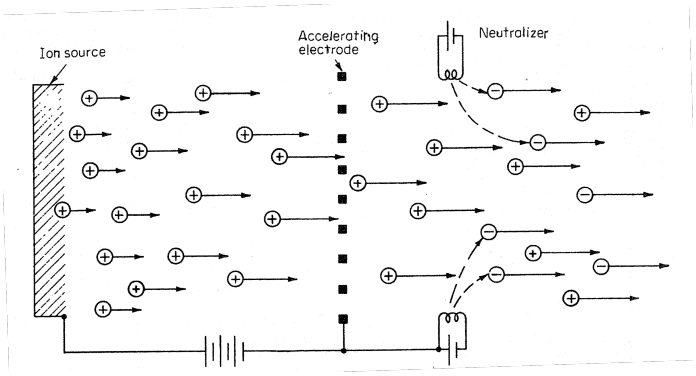

(b) Electrostatic acceleration of charged particles using an electrode and subsequent neutralization.

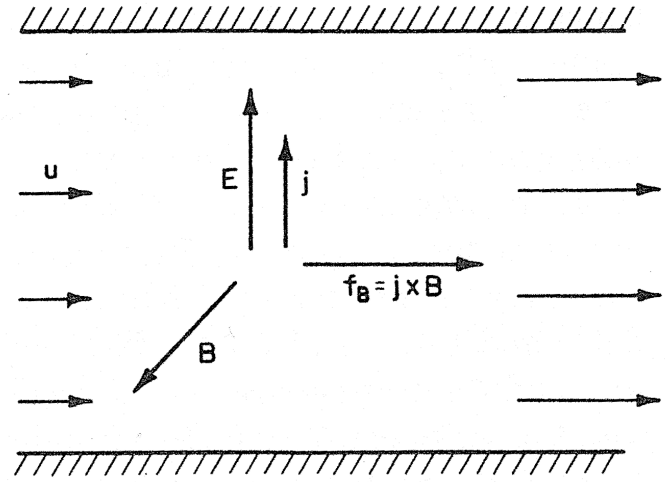

(c) Electromagnetic acceleration visualized as the Lorentz force resulting from crossed fields.

Figure 1.1: Illustrations of the underlying physical processes behind the three categories of electric propulsion devices, from Jahn [1].

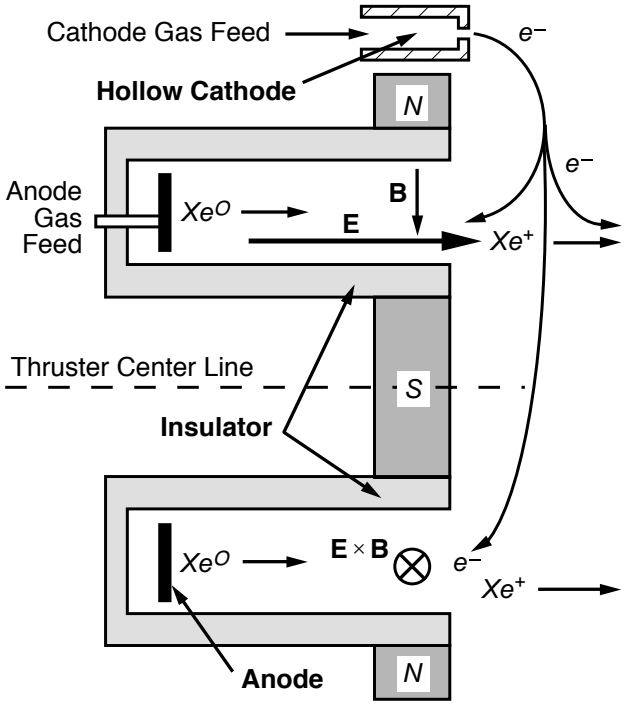

(a)

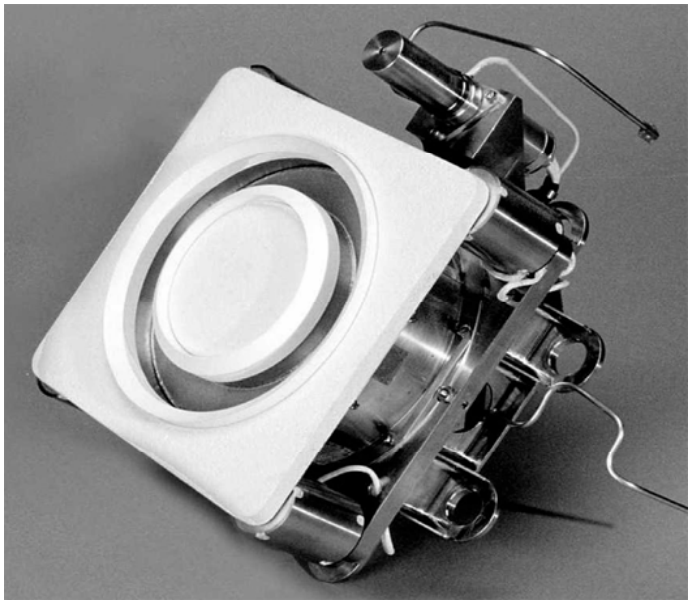

(b)

Figure 1.2: Illustration of a Hall effect thruster (HET), from Goebel and Katz [2] (a) and a photograph of a BPT-4000 Hall effect thruster (HET), manufactured by Aerojet [3] (b).

There are two types of HET: stationary plasma thrusters (SPTs) and thrusters with anode layer (TALs) [31]. In the SPT, insulating material such as boron nitride is used for the walls of the acceleration channel which is relatively long, on the order of centimeters. The TAL, however, has a very short acceleration channel, on the order of millimeters, and is made of metallic walls such as stainless steel. This conductive material leads to a constant potential along the channel wall and higher electron temperatures than those of SPTs. However, from a spacecraft integration point-of-view, TALs are often much heavier and therefore are sometimes thought to be more difficult to integrate into the often strict mass constraints of a space mission.

1.2.4 A collaborative, simplified, experimental facility: the Test Cell

This study focuses on stepping back from previously mentioned full-device HET operation in order to develop and validate models which can simulate and predict the fundamental physical processes that occur. There is a particular interest in the simulation of plasma transport mechanisms in HETs through the use of kinetic methods such as direct simulation Monte Carlo (DSMC) and particle-in-cell (PIC) algorithms [32, 33]. Kinetic methods have the advantage of not limiting electron behavior to fluid assumptions, such as having a Maxwellian distribution, which have proven to be inaccurate due to the prevalence of nonequilibrium phenomena such as inelastic processes and sheath formation [34].

However, it is generally understood that important transport mechanisms, such as cross-field electron diffusion, are collective effects arising in magnetized, low-temperature environments and require high fidelity simulation of more than just electron physics. [35, 36] The inelastic processes and transport mechanisms of the heavy species involved in these devices must be understood so that an anomalous transport model can eventually be built incrementally, introducing, for example, the complexities of multiple species, device geometry, and magnetic fields. This is also

the case for the interactions of heavy species with the device walls as sheaths, sputtering, and emission will likely result. This research aims to eliminate as many of the complexities of full-device simulation and operation as possible with the hopes of directly studying the phenomena of specific models related to transport physics. This can be done by simulating a simplified and well-characterized environment in a scaled-down facility.

The experimental setup which is the focus of this simulation study is constructed by Wirz, et al. [37, 38, 39, 40, 41], located at UCLA, and consists of a 1.5 keV xenon ion beam of about 10 nA of current directed into a small, well-characterized, cylindrical facility made from stainless steel and held at a controlled pressure. The objective of the facility is to study a well-characterized ion beam collected in a well-defined target domain, called the Test Cell. The Test Cell is used to gather precise measurements of current resulting from the transport of various plasma species as the ion beam is accelerated into the bulk volume of the Test Cell which has been populated with background xenon atoms. The Test Cell is designed to have an axisymmetric volume measuring 152 mm long and 48.24 mm in diameter. The large aspect ratio of the Test Cell allows for a clear separation between low-angle and high-angle scattering events allowing for the ability to distinguish between different collision types. A schematic and photograph of the facility can be seen in Figure 1.3. The important, current-collecting electrodes are labeled in Figure 1.3(b) as the Inner Cylinder (IC), Exit Plate (EP), and Exit Orifice (EO). The main purpose of the Test Cell is to be easily integrated into numerical studies for the validation of numerical models. A numerical description of the facility optimized for computational simulation is described later in Section 3.2.

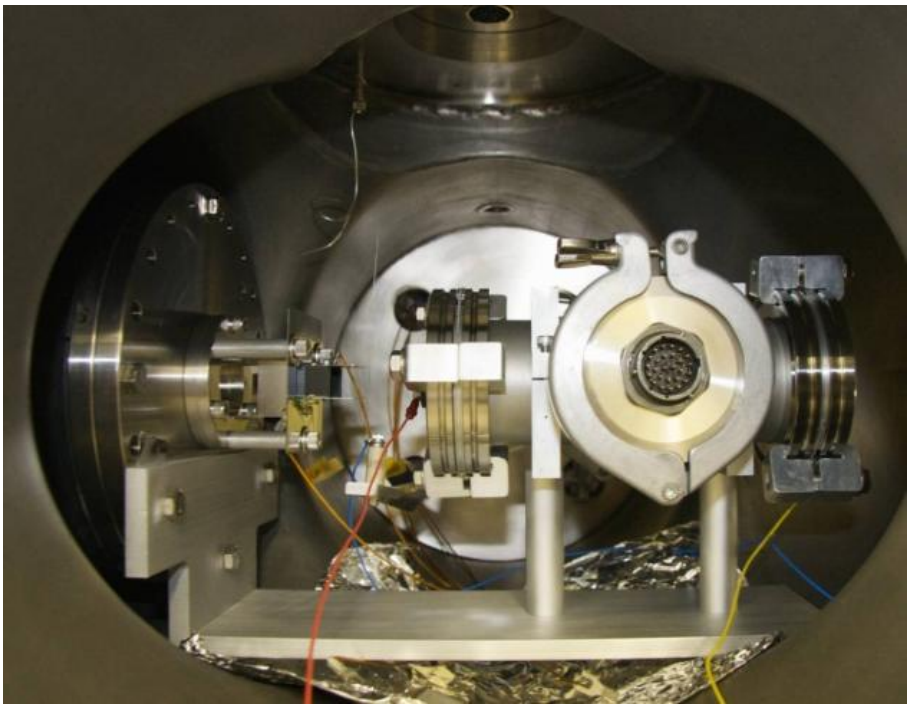

(a) Top-down photograph of the Test Cell.

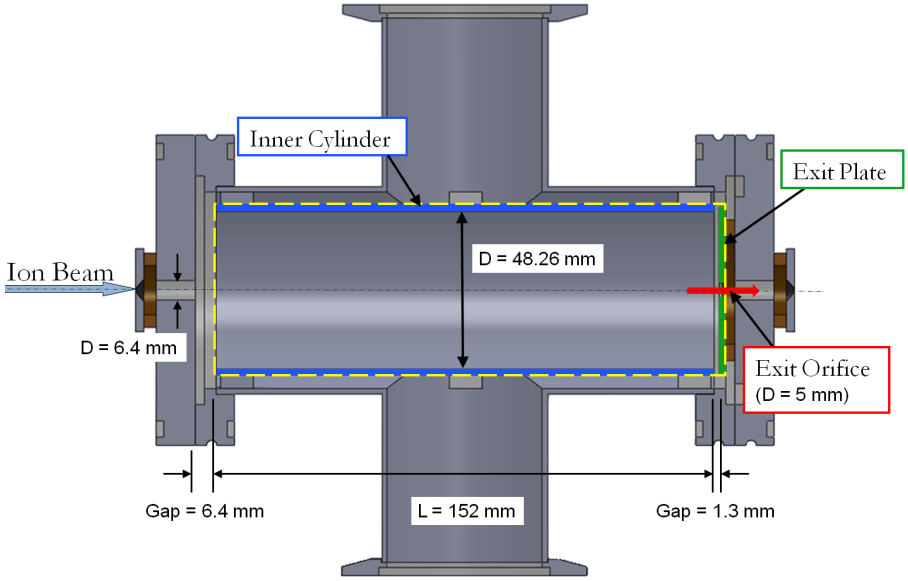

(b) Working schematic of the components of the Test Cell, listing major electrode locations and names.

Figure 1.3: Photographic (a) and schematic (b) visualizations of the Test Cell, courtesy of UCLA.

1.2.5 Computational modeling of electric propulsion devices

Computational modeling provides a method for analysis of electric propulsion devices and their underlying physics without the complexity and cost of ground testing. Modeling efforts can both assist in the characterization of a thruster and its operation as well as work toward the validation of new and improved physical models which are used on the scale of the fundamental physics of a device.

Three types of computational models are typically applied in the simulation of plasma devices and their physics:

1. *Fluid models* [42, 43] make the assumption that all charged and uncharged species can be represented as fluids. They are typically very computationally efficient and easily expandable to multiple dimensions. They are, however, subject to the assumptions made about the inherent velocity distribution functions chosen in their derivation as moments of the Boltzmann equation.

2. *Kinetic/particle models* [34, 44, 45] use numerical particles as a representation of charged and uncharged species and are better suited for nonequilibrium environments as they are not subject to continuum and equilibrium assumptions. However, they are often computationally inefficient when both heavy and light species, such as ions and electrons, are simultaneously used due to the large disparity in time scales. The kinetic method is one of the underlying foundations of the DSMC and PIC computational methods, described in detail in Chapter III.

3. *Hybrid models* [46, 47, 48, 49, 50, 51] use a combination of the assumptions made in the fluid and kinetic methods. A typical hybrid model assumes that the heavy species can be represented as particles and the electrons can be represented as a fluid. This combination aims to grasp the most tractable aspects of both kinetic and fluid sets of assumptions. The heavy species of plasmas of interest are typically in rarefied, non-Maxwellian environments and are thus well suited for

a particle representation. Furthermore, Maxwellian or equilibrium assumptions for electrons can be valid for first assumptions and can lead to one of various options for simulating electron physics, ranging from the simple, logarithmic description of the Boltzmann relation to a more sophisticated electron fluid model [52]. This choice of electron fluid assumption also reduces the immense computational cost resulting from particle electron descriptions.

Boyd's 2001 review [46] of HET plume modeling led to a major emphasis on hybrid methods for the simulation of full-device HET operation. Thus, the main computational tool used in the simulation of this work, MONACO-PIC, was originally developed with hybrid functionality, described in detail in Chapter III. However, due to the simplified nature of the present work and the importance of accurate collision and transport modeling, MONACO-PIC was modified to use a purely kinetic approach with few macroscopic assumptions. This lack of assumptions also required a direct solution of the Poisson's equation in order to resolve electric potential contours within the Test Cell rather than relying on an assumption of non-zero electron density, also described in detail in Chapter III.

1.2.6 Past efforts in heavy species collision modeling

Validation of heavy species transport models commonly used in HETs is a major step toward a more comprehensive device plasma transport model. The study of ion-atom interactions dates back to the collision models of Rapp and Francis [5] which resulted in a basic symmetric charge transfer model for gaseous interactions. A large body of work was delivered four decades later on the subject of elastic and inelastic momentum exchange (MEX) and charge exchange (CEX) interactions in the context of ion thruster and HET operation, spearheaded by researchers at Hanscom Air Force Base [21, 4, 53, 54]. The ability to resolve MEX and CEX collisions is important in the characterization of electric propulsion plumes. The CEX interaction in electric

propulsion plumes results in a population of charged heavy species with a very slow velocity and possibly high projectile angles, leading to a high susceptibility of back-streaming toward the thruster or a sensitive spacecraft device. Past efforts have shown the difficulty in correctly resolving this high-angle region of the beam with a Faraday probe (discussed further in Section 1.2.7), most likely populated with CEX ions. The work of Boyd and Dressler [48] on current density comparisons between experimental *in situ* plume measurements of an SPT-100 HET on the Express spacecraft with ground facility current measurements and computational models showed an initial disparity between current density results at high angles, an example of which is seen in Figure 1.4(a). A similar disparity was noticed by Mikellides, et al. [55], for a BPT-4000 HET, seen in Figure 1.4(b). The work by Pullins, et al. [21] and Miller, et al. [4], showed that the original Rapp and Francis method over predicted total cross sections for xenon ion-atom interactions by $\sim 30\%$. In addition, much of this body of work has shown the various dependencies of charge or metastable state on these interactions [54]. Chiu, et al. [53] expanded on the differential cross-section descriptions for these xenon interactions.

Recently, work by Scharfe, et al. [14] and Huismann [56, 15] extended the differential cross-sections of Chiu to a DSMC method for the direct application to HET plume simulation, with Huismann comparing current density predictions at high plume-angles for the H6 HET to experimental results from the University of Michigan and NASA-JPL [57, 58]. A common theme among this history of heavy species collision models and experiments, however, is that they are carried out in the context of either 1) an oversimplified guided-ion beam time-of-flight (GIB-TOF) experiment [59, 21] or *ii*) full device operation [48, 55, 15]. The aim of this computational study is to mirror the developments of the experimental counterpart at UCLA for the purpose of investigating heavy-species collision mechanisms in the previously described well-characterized Test Cell. This study utilizes a kinetic simulation to compare computed

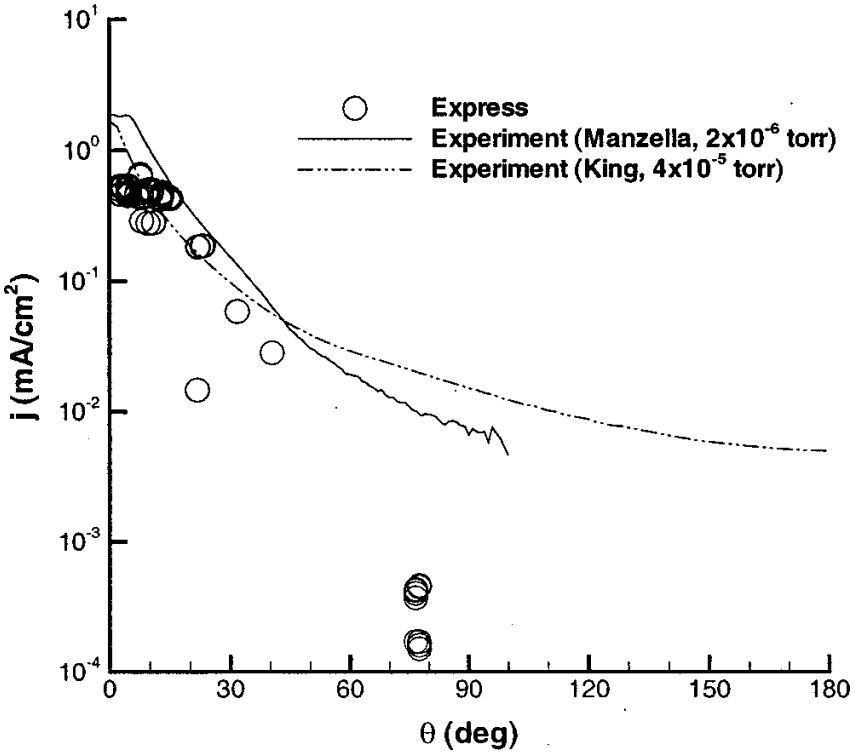

(a) An example of disparities between space and ground operation of an SPT-100, documented by Boyd and Dressler [48].

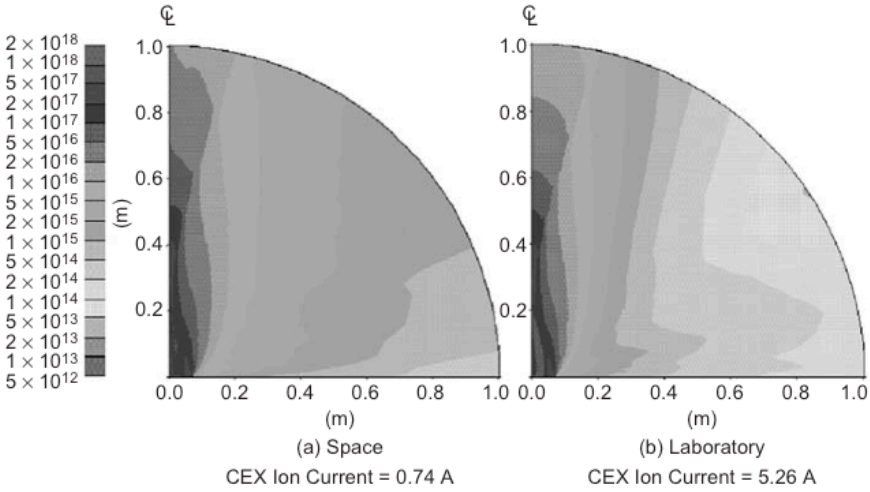

(b) An example of disparities between space and ground operation of a BPT-4000, documented by Mikellides, et al. [55, 2]

Figure 1.4: Examples of plume disparities seen between space operation, ground-facility operation, and numerical simulation for an SPT-100 (a) and BPT-4000 (b).

ion beam current predictions to measured values using current collection at specific electrodes on the facility walls. The simulations take into account the biased potential of the Test Cell, the non-neutrality of the injected ion beam, and ion beam divergence. A detailed description of the theory of heavy species collisions and transport for this work can be found in Chapter II.

1.2.7 Past efforts in SEE modeling

The well-characterized nature of the UCLA Test Cell has proven to be advantageous in the collection of secondarily-created electrons in both biased and unbiased operation. In preliminary current collection comparisons, it was found that high-pressure regimes of Test Cell operation resulted in a large disparity between simulation and experiment [60], also seen in the preliminary results of Chapter IV. Furthermore, this disparity could be controlled depending on the bias voltage of the Inner Cylinder of the Test Cell, essentially changing the current-collecting mode of the facility. In other words, by biasing certain components of the Test Cell positively or negatively during operation, high- and low-energy positively-charged ions and secondary negatively-charged electrons would be either electrostatically attracted or repelled from current-collecting surfaces.

Secondary emission is the process of an impacting (primary) particle striking a surface and resulting in an emitted (secondary) particle, illustrated in Figure 1.5. In the context of electric propulsion analysis, secondary electron emission (SEE) has traditionally been approached using electrons as the primary particles and applying the classical theory of Hobbs and Wesson [61]. Models have been developed using this approach by Ahedo et al. [62] using a theoretical fluid sheath/pre-sheath model, and Taccogna et al. [63] using a kinetically-treated plasma-surface interaction model. Taccogna's work includes a very comprehensive literature review of SEE via primary electrons. SEE is a very important phenomenon to characterize in HETs as, among

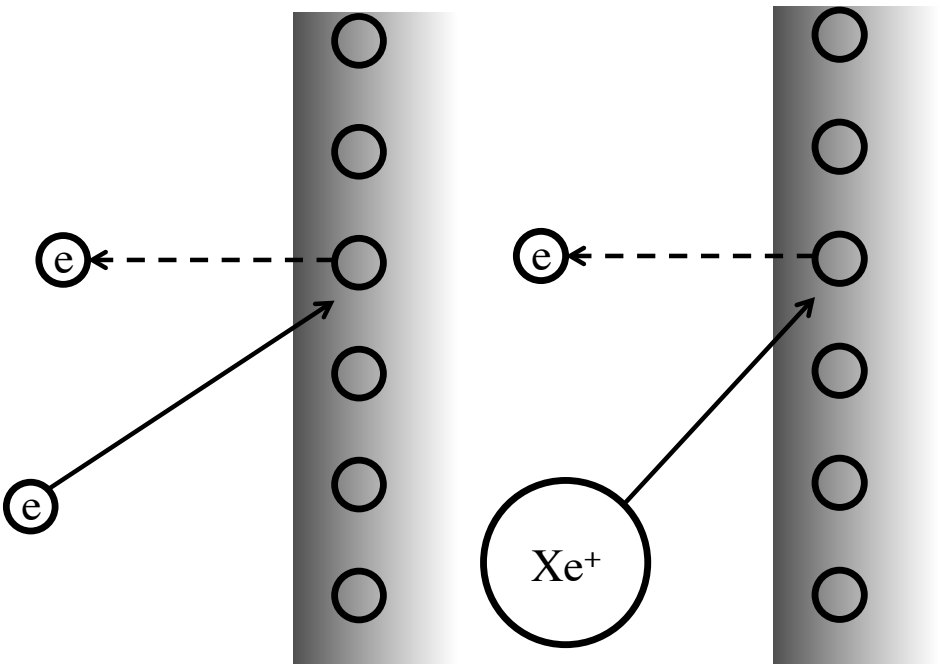

Figure 1.5: Basic visualization of secondary electron emission (SEE) (a) and particle-induced electron emission (PIE) (b) from a surface such as a metal which contains a surface conduction band of electrons.

other reasons, it is often referred to as a possible augmenting process to electron cross-field mobility [64], also known as "anomalous" electron mobility, as transport due to classical collision mechanisms are found to be insufficient. Those who do not make the often contentious link between SEE and anomalous electron mobility still focus on the importance of near-wall electron production within the HET discharge [65, 66, 67].

Additionally, the measurements attained from probing an electric propulsion plume using a Faraday probe can be artificially augmented via SEE effects. The Faraday probe is a device which collects ion current at locations measured angularly from the thruster exit and is integrated across the beam to arrive at a total discharge ion current. SEE effects of impacting ions on Faraday probes, often made out of molybdenum or a similar metal, are typically not included in experimental investigation or numerical simulation yet can be extremely important as an emitted electron resulting from an ion-surface interaction is indistinguishable from a collected ion [68]. Past

collections of work in which extensive thruster diagnostics-based studies are carried out by, for example, Hargus et al. [23] and Walker et al. [69], simply mention that the effect of SEE has the possibility of current collection augmentation yet stop short of detailed analysis or descriptions. This diagnostic approach could benefit from a more detailed understanding of the effects of heavy species-induced electron emission.

The common description of electron-induced SEE, however, is not valid for an environment which is dominated by heavy-species interactions with the surfaces of a facility. A subset of secondary electron emission is particle-induced electron emission (PIE), the process of secondary electron emission via impact of neutral or charged heavy species, such as xenon and the noble gases, also illustrated in Figure 1.5. For the purpose of clarity, a convention will be used which refers to secondary electron emission (SEE) for primary electrons and particle-induced electron emission (PIE) for primary heavy-particles. PIE is a more appropriate description of electron emission in the Test Cell and is absent in much of the electric propulsion literature which is mostly dominated by SEE treatments and the effect of electron-wall interactions on electron mobility. The Test Cell allows us to separate and study the potential effects of PIE on a representative HET environment.

PIE has been historically studied in the context of two modes of emission, kinetic emission (KE) and potential emission (PE). KE refers to the emission of electrons via the direct interaction of the primary particle kinetic energy with the kinetic energies of the electrons at the surface of the material. PE, on the other hand, is the process of electron emission via the interaction of the internal properties and potential energy of the primary particle with the surface valence band structure of electrons at the surface of the material. Modern formulations of PIE became a process of interest with the advent of Ion Neutralization Spectroscopy in the 1950s and became a very well characterized process in the following decades [70]. The process of PIE due to both high- and low-energy xenon ions and atoms could be a potentially underrepresented

source of secondary electrons in an environment such as that in an electric propulsion device which has a complex mixture of heavy species populations. The Test Cell proves to be an effective facility for observing the effects and transport due to PIE and is described in detail in Chapter II.

1.3 Objectives

The scope of this project and dissertation is to improve the understanding and accuracy of the modeling of fundamental physics behind certain heavy species and electron transport physics in a well-defined environment which mimics that of a HET. The specific objectives of this work are outlined in the following sections.

1.3.1 Validation of heavy species collision models

Previous experimental and computational studies have investigated the MEX and CEX interactions between xenon atoms and ions using either a complicated, full-device experiment for the characterization of thruster operation or an over-simplified cross-section experiment which is not representative of an electric propulsion environment. In this work, care is taken to reproduce the environment found in a HET and to validate the heavy species collision models which are essential in the characterization of plume models. Previously the focus of 300 eV energies [15], it is shown in this work that the total and differential cross-section models for xenon can be extended to a collision energy of 1.5 keV. The focus on this higher-voltage ion beam not only allows us to validate the repeatable operating conditions of the Test Cell but can also be useful to current and future developments for high-power, high-voltage HETs [71]. Cases are simulated in which the environment is either collisionless or non-electrostatic in order to prove that the collision models are the dominant source of low- and high-angle particle scattering and current collection within this environment. Additionally, isotropic scattering cases are run in order to show the importance

of anisotropy in these collision models.

1.3.2 Explore PIE as an electric propulsion transport mechanism of interest

The unique environment created within the Test Cell provides the ability to resolve the effects of PIE and its contribution to secondary electron transport within a representative HET environment. This work aims to explore particle-induced electron emission in the context of the Test Cell and electric propulsion environments. PIE could be an important process for low-energy, near-wall electron production in electric propulsion devices. In addition, a better description of PIE could lead to a more physics-based description of current disparities often found in Faraday probes, an important diagnostic tool in HET characterization. In order for PIE to be a useful model in this environment, its detailed governing equations must first be reduced to lower-order models which can be implemented in a DSMC-PIC framework. These reduced-order models and their numerical applications will be described in full and presented as an important addition to the work of plasma-surface interactions in the field of electric propulsion.

1.3.3 Development and analysis of PIE reduced-order models

Through the implementation of a reduced-order model for particle-induced electron emission, detailed information can be learned about the interaction of low- and high-energy xenon ions and atoms with the stainless steel electrodes of the Test Cell. With the implementation of PIE in DSMC-PIE simulations, insight can be gained into the transport of secondary electrons within this representative environment by testing the sensitivities of emitted-electron behavior to the environment and emission region. Furthermore, there is a lack of data for xenon-stainless steel atom- and ion-surface interactions for environments of interest to electric propulsion. Using experimental

data as a reference, both total yields and emitted electron energy distribution functions (EEDFs) can be deduced by observing sensitivities of current collection results to these numerical models and their parameters. This insight could lead to more physics-based SEE and PIE models for use in the electric propulsion community.

1.4 Organization of the dissertation

Chapter II outlines the fundamental theory and governing equations of rarefied gas dynamics, heavy species transport, electron emission, and reduced physical models which can be implemented in a numerical simulation.

Chapter III describes the various numerical approaches to modeling the physical phenomena described in Chapter II, detailing such algorithms as the kinetic, statistical nature of simulating rarefied particles, a direct solution of Poisson's equation for electric potential, and the simulation techniques of both heavy species and electrons.

Chapter IV details the initial current collection results of the Test Cell at various operational modes and with an array of different Data Sets. These simulated results use only heavy species and are then compared to experimental measurements so that the validity of the heavy species transport models may be assessed.

Chapter V details the results of current collection simulations with the addition of PIE physics and the transport of electrons through the Test Cell. PIE parameters used in the proposed reduced-order models are analyzed and their sensitivities are quantified.

Chapter VI provides a summary of the work completed and contributions to the field. This chapter also lists suggestions for future Test Cell simulations and experimental design and ends with suggested future work in heavy species and electron emission modeling.

CHAPTER II

Theory of Heavy Species Collisions and Electron Emission

This chapter describes the underlying transport physics behind the collision and emission phenomena which are simulated in this work. Rarefied gas dynamics will be introduced in Section 2.1 as the Test Cell largely operates in a rarefied to transitional regime. Transport models are then described in two major categories: the formulation of collision cross-sections for the interactions between heavy species in Section 2.2 and the particle-induced emission of electrons into the Test Cell in Section 2.3. The numerical implementation of these models is explained further in Chapter III.

2.1 Rarefied gas dynamics

Models for the dynamics of fluids and gases fall into two major categories of assumptions: macroscopic and microscopic/molecular. Macroscopic-level models make the assumption that the gas or fluid can be represented as a continuum and can therefore rely on solutions for macroscopic-level properties such as velocity, temperature, pressure, and density. The Navier-Stokes equations are the most popular set of equations for solving flow physics at the macroscopic level. Molecular models, on the other hand, describe gases and fluids as discrete packets of information contain-

ing details of the internal properties of the medium. A molecular description can simulate macroscopic properties by only focusing on position, velocity, and internal parameters and by utilizing such models as the Boltzmann equation.

2.1.1 Definition of flow regime

Assuming that any flow can be discretized into infinitely-small packets of volume, continuum hypotheses are only satisfied when enough particles are represented in said packets such that average values are representative of the macroscopic properties of the entire flow. However, when a gas is rarefied, this condition does not hold and the continuum method results in a loss of accuracy. The amount of rarefaction is related to the ratio of the average distance traveled by molecules between collision events to the characteristic length scale of the flow, resulting in the Knudsen number (Kn),

$$Kn = \frac{\lambda}{L} \ , \tag{2.1}$$

with λ as the mean free path and L as the characteristic length scale. Mean free path for a collision in which the colliding particle has a large velocity compared to the target particle can be defined as,

$$\lambda = \frac{1}{\sigma n} \ , \tag{2.2}$$

using the collision cross-section (σ), discussed further in Section 2.1.2, and the number density (n) of the relatively motionless target particle.

Typically, continuum flow descriptions such as the Navier-Stokes equations are used up to the upper bound of $Kn \simeq 0.01$ in modern computational methods [16]. Environments found in the range of $Kn \simeq 0.01$ to 1 are considered "transitional" regimes in which molecular-level models should be considered. Environments found at a Knudsen number of $Kn \geq 1$ are considered rarefied and require molecular de-

scriptions.

The Test Cell operates in environments in the rarefied and transitional regimes and so the molecular approach is used for descriptions of discrete particles which represent the environments.

2.1.2 Collision cross-sections

A molecule in a dilute gas can be initially defined as having a diameter d using the simplified elastic hard sphere model [16]. This allows for a collision to occur between two molecules if the distance between their trajectories decreases to d. The total cross-section can then be defined geometrically as the region of an occurring collision related to the diameter as

$$\sigma = \pi d^2 \ , \tag{2.3}$$

treating d as a radius than a diameter because of its definition as the distance between the centers of the molecules. This region is created by the effects of intermolecular force fields and assumed to be spherically symmetric. The cross-section is a function of the relative speed between molecules and is often represented as relative collision energy, a concept that is further discussed in Section 2.2.

When there is need for more information about the post-collision details of an interaction, a differential cross-section ($\mathrm{d}\sigma/\mathrm{d}\Omega$) may be used in order to describe the scattering behavior of a molecular system. The differential cross-section defines the number of scattered molecules per infinitesimally small solid angle ($\mathrm{d}\Omega$) by associating these scattering behaviors with a small portion of cross-section ($\mathrm{d}\sigma$). The differential cross-section can be integrated to obtain the total cross-section in the laboratory frame using the following integral,

$$\sigma = \int_0^{\pi} \frac{\mathrm{d}\sigma}{\mathrm{d}\Omega} 2\pi \sin(\theta) \mathrm{d}\theta \ , \tag{2.4}$$

Reference Parameter	Reference Value
Viscosity coeff., ω	0.85
Diameter, d_{ref}	5.74 Å
Temperature, T_{ref}	273 K
Speed, $g_{r,\text{ref}}$	209.8 m/s

Table 2.1: Reference values for xenon using the VHS model [16].

integrating over all scattering events and angles and assuming azimuthal symmetry, as further discussed in Section 2.2.2.

2.2 Heavy species cross-section models

This section describes the various models used in the formulation of cross-sections for binary collisions involving both xenon atoms and ions. The total and, if relevant, differential, cross-sections will be established to set the foundation for the numerical implementation which is described in Section 3.4.

2.2.1 Atom-atom interactions

Xenon atom-atom, Xe-Xe, collisions are modeled elastically using Bird's Variable Hard Sphere (VHS) model [32], the standard model for the DSMC numerical method, the most commonly used particle simulation technique for rarefied gas flows [16]. First introduced by Bird [32] in the 1960s, the method has become widely developed and largely accepted in the scientific community. The DSMC method uses numerical macroparticles which represent a larger number of real molecules and is a more efficient method than other kinetic methods such as the molecular dynamics technique which attempts to simulate interactions between all real particles. The VHS model is used within the No-Time-Counter (NTC) collision routine, described in the numerical implementation details of Section 3.4.1.

The VHS model was originally formed as an advancement of the hard sphere model of molecules. The VHS concept is a more physics-based model in that the

cross-section (σ) of a molecule decreases as relative velocity (g_r) increases. This VHS cross-section is described using an inverse power law for the variable diameter of the molecule,

$$d_{\mathrm{VHS}} = d_{\mathrm{ref}} \left(\frac{g_{r,\mathrm{ref}}}{g_r} \right)^{1-2\omega} \tag{2.5}$$

where "ref" refers to reference values and found in Table 2.1 for xenon atoms using a diameter (d_{ref}) and relative collision speed ($g_{r,\mathrm{ref}}$) at a reference temperature (T_{ref}).

The VHS cross-section can then be calculated using Equation 2.3 as $\sigma_{\mathrm{VHS}} = \pi d_{\mathrm{VHS}}^2$. Additionally, the relative speed may be substituted for the relative collision energy (E_r) as $E_r = \frac{1}{2}\frac{m}{q} g_r^2$ eV using the elementary charge (q) and element mass (m). The collision model only provides information for the cross-section without any special *a priori* knowledge about the post-collision scattering details and therefore assumes that the collision is isotropic.

2.2.2 Atom-ion interactions

The models of interest for collisions between xenon atoms and ions, Xe-Xe^+, in these simulations are related to the physical phenomena of momentum exchange (MEX) and charge exchange (CEX) interactions. The models for establishing Xe-Xe^+ cross-sections are formed in a similar manner to Xe-Xe collisions in that they are inversely related to relative collision energy. However, the nature of total and differential cross-section behavior varies greatly and must be treated in detail.

Development of atom-ion interaction models for xenon and other noble gases began in the 1950s as a quantum-mechanical, theoretical treatment of ion mobilities through like and unlike gases. The theory for atom-ion CEX cross-sections resulted in a logarithmic formulation, originally established by Demkov [72, 73] and Dalgarno [74, 75], which follows the general formula of

$$\sigma \sim a \ln(E_r) + b \; . \tag{2.6}$$

The work of Rapp and Francis [5] attempted to take a more empirical approach to the calculation of these cross-sections, eventually arriving at the same formulation as Equation 2.6 using an *a priori* approach that combined experimental and theoretical results. This data was also found to lie in a useful particle velocity range for various applications, approximately 10^4 to 10^6 m/s, and so became a standard in such fields as electric propulsion. A similar approach was taken at lower velocities by Sakabe and Izawa [6].

The total Xe-Xe^+ cross-sections used in this study, however, are calculated from the logarithmic formula proposed by the work of Pullins et al. [21] and Miller, et al. [4] (whose laboratory's legacy of cross-section measurements is described in detail in Section 1.2.6), as

$$\sigma_{\mathrm{CEX}} = 171.2 - 27.2 \log_{10}\left(g_r \text{ [m/s]}\right) \text{ Å}^2 \text{ or} \tag{2.7}$$

$$\sigma_{\mathrm{CEX}} = 87.3 - 13.6 \log_{10}\left(E_r \text{ [eV]}\right) \text{ Å}^2 , \tag{2.8}$$

which results in a cross-section larger than the Rapp and Francis model and smaller than the Sakabe and Izawa model. A comparison of these cross-sections can be seen in Figure 2.1 for a range of collision energies of interest. This model leads to a total cross section of $\sigma_{\mathrm{CEX}} = 44.1$ Å^2 for the Test Cell 1.5 keV ion beam, corresponding to a xenon ion velocity of 46,923 m/s.

Boyd and Dressler [48] continued analyzing the applicability of the Xe-Xe^+ CEX model as applied to far-field electric propulsion plume models and concluded that the MEX and CEX cross-sections are similar enough to be equated, $\sigma_{\mathrm{MEX}} = \sigma_{\mathrm{CEX}}$. This approximation arises in the equivalence of the CEX probability for impact parameters (b) under a threshold which is met in the assumption of the close proximity of pairs for the DSMC method, described further in Chapter III.

Differential cross-sections ($\mathrm{d}\sigma/\mathrm{d}\Omega$) for the atom-ion CEX interaction were ob-

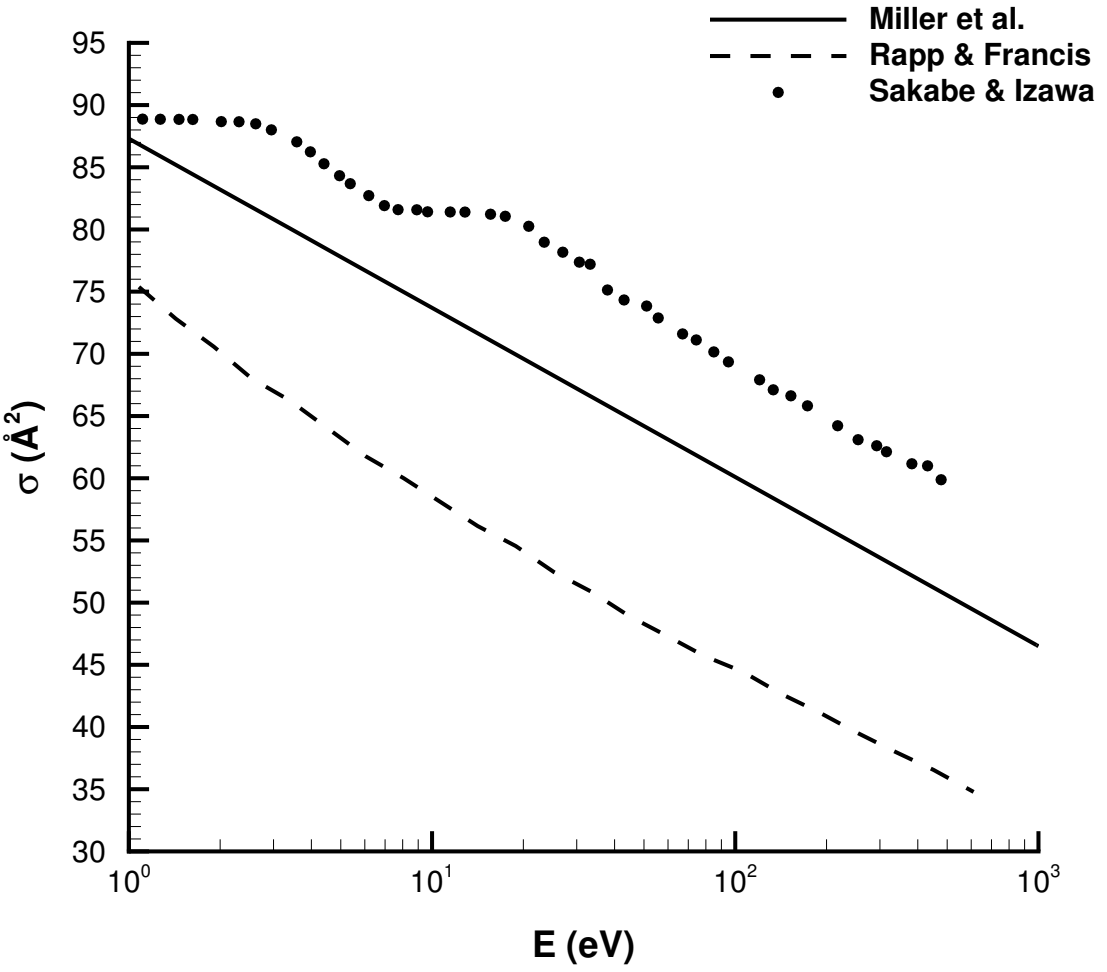

Figure 2.1: Comparison of atom-ion CEX cross-sections from Miller et al. [4], Rapp and Francis [5], and Sakabe and Izawa [6].

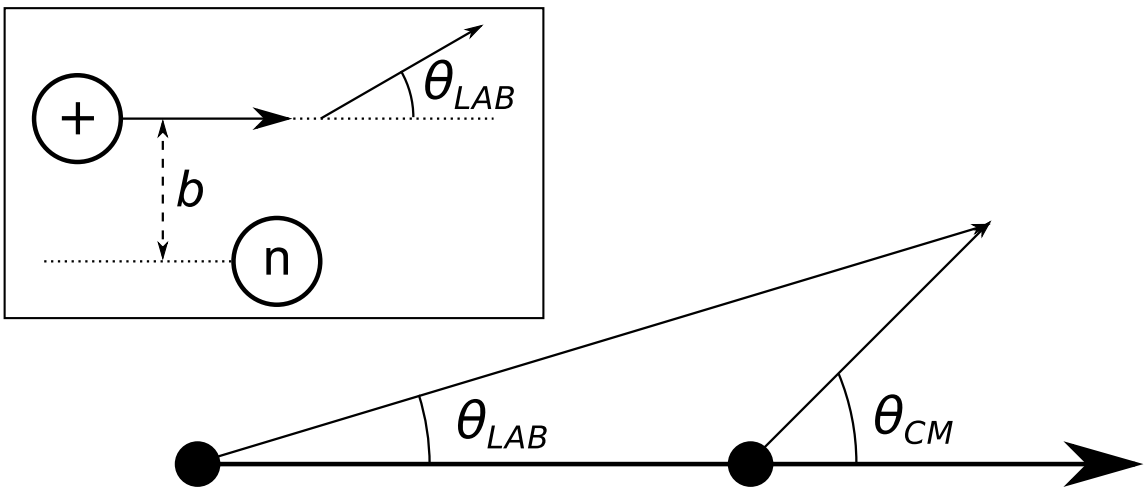

Figure 2.2: Illustration of the scattering details of an atom-ion interaction taking into consideration deflection angle (θ) and impact parameter (b).

tained by Chiu et al. [53] using a semi-empirical approach of theoretical potential models and a guided-ion beam experiment. The differential cross-section allows for a more detailed representation of the post-collision scattering properties of an atom-ion interaction depending on the inter-atomic potential structure ($V(r)$) of a pair separated by distance r. The importance of these differential cross-sections lies in their anisotropic nature which is much more detailed than the isotropic VHS description.

Moving from the laboratory (LAB) to the center-of-mass (CM) frame of reference, Figure 2.2 shows the deflection angle (θ) due to potential field ($V_i(r)$) at a specific translational energy (E) and impact parameter (b) for an i^{th} instance. This angle can be calculated as [76]

$$\theta_i(E,b) = \pi - 2b \int_{R_0}^{\infty} \frac{\mathrm{d}R}{R^2\sqrt{1-\frac{b^2}{R^2}-\frac{V_i(R)}{E}}} \tag{2.9}$$

using R as the inter-atomic distance of the particles and R_0 as the closest point of approach for the impact trajectory. The "total" differential cross-section for the entire interaction can then be obtained by summing over all i differential cross-sections at

all j impact parameters, b_j, as

$$\frac{\mathrm{d}\sigma(\theta, E)}{\mathrm{d}\Omega} = \sum_i \frac{\mathrm{d}\sigma_i(\theta, E)}{\mathrm{d}\Omega} = \sum_j \left| \frac{b_j}{\sin(\theta_i)\frac{\mathrm{d}\theta_i}{\mathrm{d}b_j}} \right| . \tag{2.10}$$

Chiu et al. combined theoretical potential curves for $V(r)$ as well as experimental scattering results to obtain semi-empirical curves for differential cross-section versus center-of-mass scattering angle for various energies. These semi-empirical curves provide *a priori* knowledge of the post-collision scattering angles of Xe-Xe$^+$ collisions and can thus be applied numerically to advance the post-collision behavior from isotropic to anisotropic. At the time of Reference [53], the primary collision energy of interest to the field of electric propulsion was 300 eV as it was representative of the nominal HET accelerating potential. The application of these differential cross-sections in a numerical simulation and the development of a 1.5 keV set of $\mathrm{d}\sigma/\mathrm{d}\Omega$ curves is discussed further in Section 3.4.

It should finally be noted that $\mathrm{d}\sigma/\mathrm{d}\Omega$ must be integrated using Equation 2.4 to ensure consistency with the total CEX cross-section, defined in Equations 2.7 and 2.8.

2.3 Particle-induced electron emission (PIE) models

Particle-induced electron emission (PIE) is a well-known process of electron emission from surfaces and a sub-set of the field of secondary electron emission. Two different mechanisms of PIE are distinguished regarding the potential and kinetic parameters of a system. If the potential energy of a projectile impinging on a surface is the principal source of impact energy, the process known as potential emission (PE) occurs in front of the surface, independent of kinetic energy, by a process known as Auger neutralization resulting in the emission of an electron from the surface. If the kinetic energy of the projectile dominates the interaction, kinetic emission (KE) results in the direct interaction of the projectile with free electrons at the surface of

the material and leading to emission of those electrons.

This section will describe the physics of PE and KE in the context of the conditions of the Test Cell for the purpose of creating reduced-order, semi-empirical models which describe total yield and emitted electron energy distribution functions (EEDFs). Therefore, most physical parameters will be proposed in the context of xenon atoms, xenon ions, and stainless steel surfaces (or iron, if stainless steel data are not available). The goal of this section is to arrive at models for both total yield and emitted EEDF for the PE and KE processes.

2.3.1 Potential emission (PE)

Potential emission (PE) is a mechanism for electron emission whereby the internal properties of an impacting particle, such as being ionized or excited, are taken into account rather than the kinetic properties. Therefore, PE is the principle mechanism for slowly-impacting particles on a solid surface. The process of PE was studied by Hagstrum for the purpose of Ion Neutralization Spectroscopy [77, 78, 7, 79, 80, 81, 82, 83] which extensively investigated the dependence on charge state, species, material, and surface conditions on PE processes of singly charged ions in their ground state. Research later extended into metastable atoms, single charged molecules, metastable ions, and multiply-charged ions.

PE via ion-impact is caused by neutralization processes taking place at very close distances to the solid surface. A schematic of the PE process can be seen in Figure 2.3 describing the principle phenomenon of PE, Auger neutralization. Auger neutralization involves a decrease in the charge state of the ion approaching a surface and the emission of an electron from the surface valence band if the neutralization energy is above a certain threshold related to the surface work function (W_ϕ).

Auger neutralization is considered a "two-electron process," meaning one neutralizes the ion and the other gains energy and is emitted through electron-electron

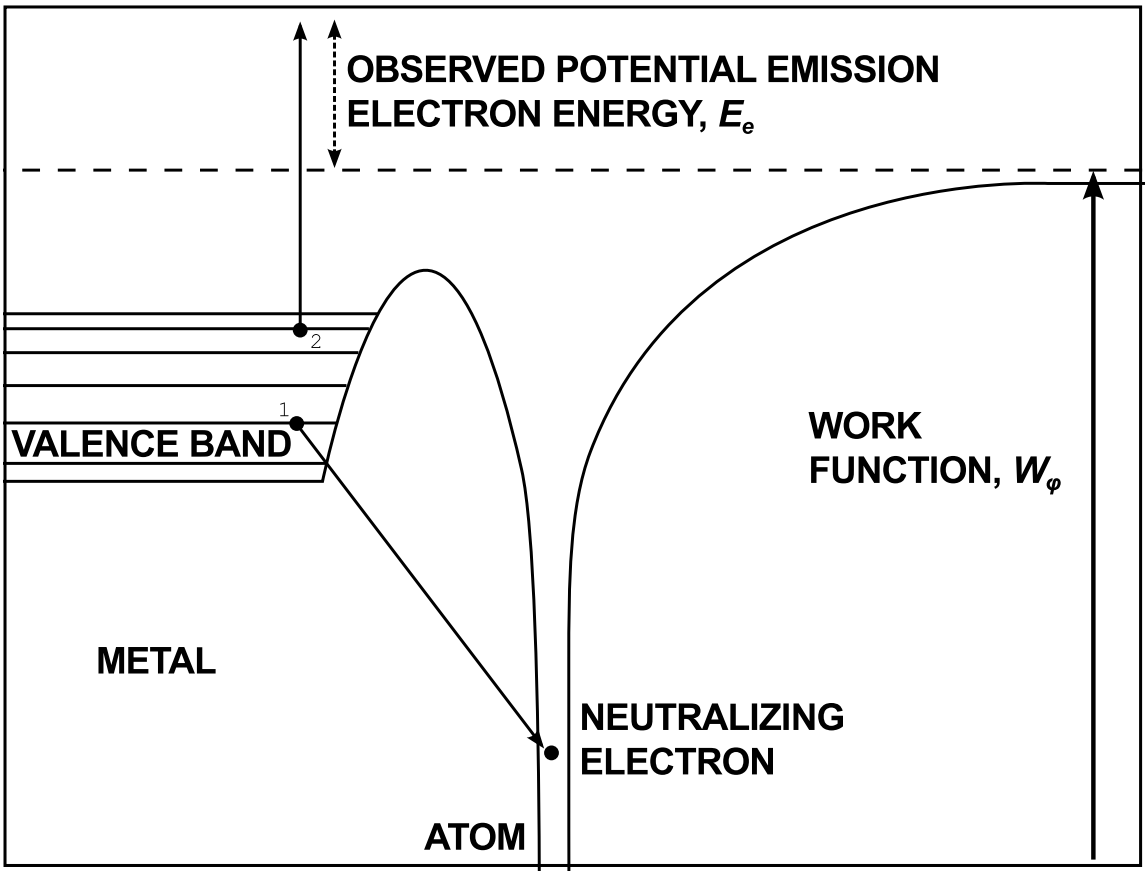

Figure 2.3: Energy diagram of the PE process, Auger neutralization, a two-electron process in which a projectile ion is neutralized by one electron while a second electron is emitted via electron-electron interactions.

interactions. The total yield of emitted electrons due to Auger neutralization corresponds to the available potential energy of the neutralized ion and the surface work function. The energy distribution of the electrons emitted is determined by *i*) the available potential energy of the particle, *ii*) Auger transition matrix elements, and *iii*) a self-convolution of the target material surface density-of-states (SDOS) which describes the behavior of electronic transitions occurring within the valence band structure of the material.

2.3.1.1 PE Total Yield

The total yield (γ) of electrons emitted from a solid surface per impacting ion is defined as

$$\gamma = \frac{I_e}{I_i} \tag{2.11}$$

where I_e and I_i are the corresponding currents of emitted electrons and initially charged ions arriving at the target surface. From the bulk of available data of projectile ions impinging on target materials, a least-squares regression [84] has led to a formula for total PE yield (γ_p) which shows a dependence on the ion potential energy (W_i) and the target surface work function (W_ϕ),

$$\gamma_p = \alpha \left(\beta W_i - 2W_\phi\right). \tag{2.12}$$

This curve is fitted to large sets of experimental data [85] and the function parameters obtained are $\alpha = 0.2/\epsilon_F$, with ϵ_F as the target surface Fermi energy (ϵ_F), and $\beta = 0.8$. It is noted that this formula does not contain the projectile impact energy and relies purely on potential energy. As either projectile potential energy increases or surface work function decreases, γ_p increases. In addition, there has been no observed relationship between the SDOS and the target's PE total yield [70]. This is not the case for the emitted electron energy distribution, discussed later.

Using the Fermi energy for iron [86], $\epsilon_F = 11.1$ eV, a common work function for stainless steel [87], $W_\phi = 4.4$ eV, and the potential energy as equivalent of the ionization energy, $W_i \equiv E_i$, or 12.13 eV for xenon, the resulting total yield of electrons due to PE processes as a function of impacting ion potential energy from Equation 2.12 is $\gamma_p = 0.016$. The total PE yield will only be of importance in certain instances of projectile-surface interaction in the test cell, namely where the majority of interactions are low-energy and Auger-like, and will be discussed later in the numerical implementation of PE processes.

2.3.1.2 PE Emitted Electron Energy Distribution Function

As mentioned before, singly-charged noble gases are neutralized mainly via Auger neutralization processes, leading to an emitted EEDF which corresponds to a self-convolution of the SDOS ($\rho(E)$) and valence band structure. An energy balance for the emitted electron, taking into account all involved particles, leads to the following equation,

$$E_e = E_n' - 2E_0 - W_{\phi,loc} - W_\phi, \tag{2.13}$$

with E_e as the emitted electron kinetic energy, E_n' as the effective neutralization energy of the particle, E_0 as the binding energy between the two electrons involved, and the two W_ϕs being the local and global material work functions, respectively. Because, in the case of ions, no initial ionization process takes place before impact, the effective neutralization energy will be equivalent to the ionization energy, $E_n' \equiv E_i$. This expression can also be simplified by assuming the local work function structure is similar to global values and the maximum electron kinetic energy ($E_{e,max}$) can also be established in the following two equations,

$$E_e = E_i - 2\left(E_0 + W_\phi\right), \tag{2.14}$$

$$E_{e,max} \leq E_i - 2W_\phi. \tag{2.15}$$

This method, however, only gives the maximum kinetic energy of an emitted electron given the surface work function and effective ionization energy of the projectile and does not describe the shape of the EEDF of those electrons. Given the lack of information about the SDOS, however, the maximum kinetic energy will assist in the creation of a representative EEDF, explained further in the next paragraphs.

The EEDF of electrons emitted by PE (henceforth referred to as "PE EEDF") can be established through analysis of Auger neutralization spectra following Hagstrum [83] in which the potentially emitted electron energy distribution function (PE EEDF) is given by integrating over all combinations of Auger neutralization transitions through a self-convolution of the SDOS, with the mathematical operation of convolution represented using the symbol "$*$",

$$f_p(E) \simeq \rho(E) * \rho(E) \simeq \int_{-E}^{E} \rho(E-x)\rho(E+x)dx \ , \tag{2.16}$$

using an effective transition spectra density function, effectively the SDOS, and the location of the electronic transitions (x) over the range of energies of the electrons in the valence band ($\pm E$). Historically, analysis is typically carried out by gathering detailed information about Auger neutralization spectra via spectroscopy experiments, leading to a unique solution to the PE EEDF and then gaining insight into the surface band structure and $\rho(E)$ of the material through a deconvolution technique [88, 89, 90]. This information, however, is not available in the scope of the Test Cell experiment and so must be obtained in another way.

In order to represent the PE EEDFs without all of the necessary Auger neutralization spectra information or SDOS, an assumption must be made about the shape of the SDOS and, thus, the EEDF of the emitted electrons. Extensive work performed on the impact of singly charged noble gas ions on such materials as tungsten, palladium, copper, and molybdenum (all from most of the PIE-related references cited in

this work) has led to a general idea of the shape of PE EEDFs due to xenon [8, 91, 70]. Furthermore, there is an issue of data availability: while there are some SDOS and EEDF data available for xenon, it is for materials other than stainless steel and while there is some SDOS data available for iron, it is either *i*) resolved for other systems than xenon-impact, *ii*) at very different temperature or ferromagnetic conditions, or *iii*) is not suitable for an effective SDOS which already contains elements of the Auger transition matrix. This leads to the need to have a representative model for an effective SDOS for stainless steel which can act as a starting point in the characterization of the PE EEDF in this environment. Therefore, it is proposed that the self-convolution method should be carried out on a "model" SDOS which is representative of the material and projectile of interest. In addition, to assist in defining the bounds of this model SDOS, it is attempted to correlate the resulting EEDF with the maximum emission kinetic energy of Equation 2.15.

This is not a completely novel approach as, in the explanation of the algorithm used by Sesselmann to test a self-deconvolution algorithm [89], a model SDOS is used which is based on a Lorentzian, or Cauchy-Lorentz, distribution superimposed on an arbitrary linear function. In studies of the spin-resolved SDOS of iron [92], as well as the general derivation of the SDOS for various surfaces and solids [93], a distribution which resembles either a Cauchy-Lorentz or Gaussian distribution is seen as the main SDOS peak. While the Cauchy-Lorentz distribution is difficult to characterize due to its high magnitude tails and nonexistent mean and variance, a Gaussian distribution has a similar shape and is much easier to define. In addition, the convolution of two Gaussian functions leads to another Gaussian function, leading to a PE EEDF for xenon-impact which represents the simple and less-broad EEDFs as compared to lighter elements, such as neon or helium [70]. Therefore, a model SDOS is used in this study of xenon-impact PE from stainless steel which is based on a Gaussian distribution and then self-convolved to arrive at a representative PE EEDF ($P_p(E)$)

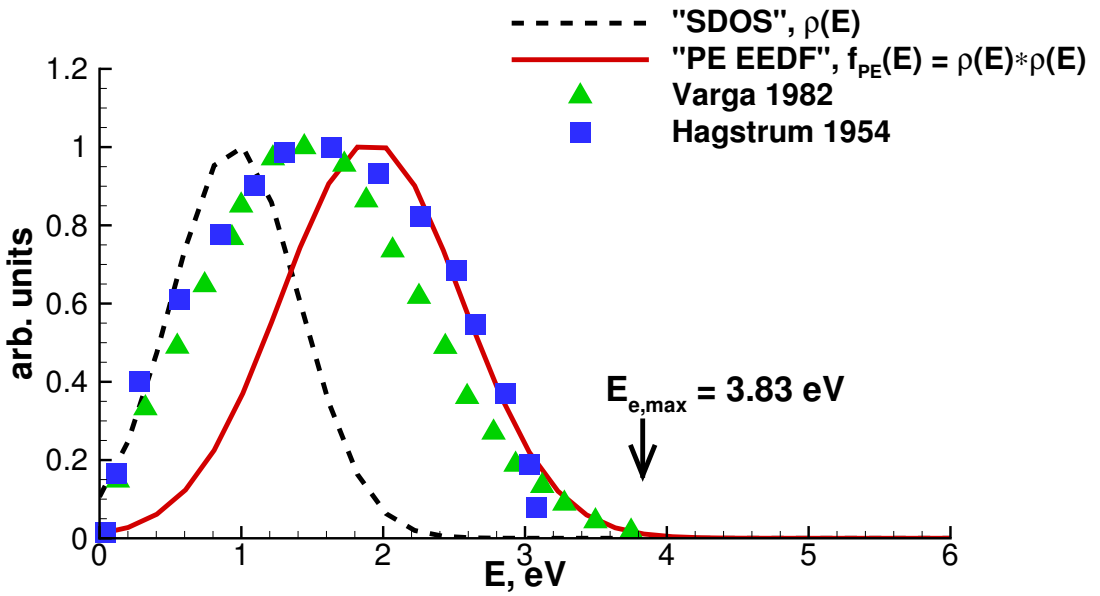

Figure 2.4: Normalized Gaussian functions representing SDOS ($\rho(E)$) and EEDF next to previously cited historical PE EEDF data for generalized, theoretical emission [7] and 10 eV xenon ion emission [8] from W.

for emitting electrons.

The Gaussian distribution [94] and its self-convolution are described by the mean (μ) and standard deviation (σ) in terms of energy (E) as

$$\rho(E) = \frac{1}{\sigma\sqrt{2\pi}} e^{\frac{-(E-\mu)^2}{2\sigma^2}} \text{ and} \tag{2.17}$$

$$P_p(E) = \rho(E) * \rho(E) = \frac{1}{2\sigma\sqrt{\pi}} e^{\frac{-(E-2\mu)^2}{4\sigma^2}} , \tag{2.18}$$

resulting in the following self-convolved Gaussian parameters,

$$\mu_* = \mu * \mu = 2\mu, \tag{2.19}$$

$$\sigma_* = \sigma * \sigma = \sigma\sqrt{2} . \tag{2.20}$$

To set the upper bound of the shape of the self-convolved Gaussian distribution

EEDF, the minimum and maximum emitted electron energies of $E_{e,min}$ and $E_{e,max}$, defined in Equation 2.15, are set to be located at three standard deviations from the mean of the distribution, meaning that 99% of emitted electrons will be found within those values. The minimum value is set to 0 eV and the maximum value is set to $E_{e,max} = 3.83$ eV, using the ionization energy of xenon, $E_i = 12.13$ eV, and the stainless steel work function used previously, $W_\phi = 4.15$ eV. Fitting the self-convolved Gaussian distribution to these constraints leads to an SDOS Gaussian fit with parameters $\mu = 0.9576$ and $\sigma = 0.4514$ and PE EEDF self-convolved parameters $\mu_* = 1.915$ and $\sigma_* = 0.6383$. This translates to PE-emitted electrons having a mean emission energy of $\simeq 1.91 \pm 0.64$ eV. The resulting Gaussian functions for SDOS and EEDF can be seen in Figure 2.4 normalized and compared with prior data.

2.3.2 Kinetic emission (KE)

Kinetic emission (KE) is the process by which a projectile directly interacts with the valence electrons of a target at high velocities resulting in the emission of those electrons [85, 11]. KE is generally thought of as a three-step process whereby electrons are *i*) excited within a solid, *ii*) diffused to the surface of the solid, and *iii*) penetrated into vacuum from the solid. The first observations of KE occurred at the end of the 19^{th} century in the pioneering experiments of Villard [95], Thomson [96], and Rutherford [97], probing the interactions of canal rays and alpha particles with solid surfaces.

Similar to PE, KE processes are described by two parameters: the total yield (γ_k) and differential energy spectra, or energy distribution curve ($d\gamma/dE$). A schematic of the KE process can be seen in Figure 2.5. The KE total yield, unlike its PE counterpart, is proportional to the kinematics between the projectile and target material via a term described as the stopping power (dE/dx) which accounts for the losses from a penetrating ion interacting inelastically with the atoms of the surface. The KE

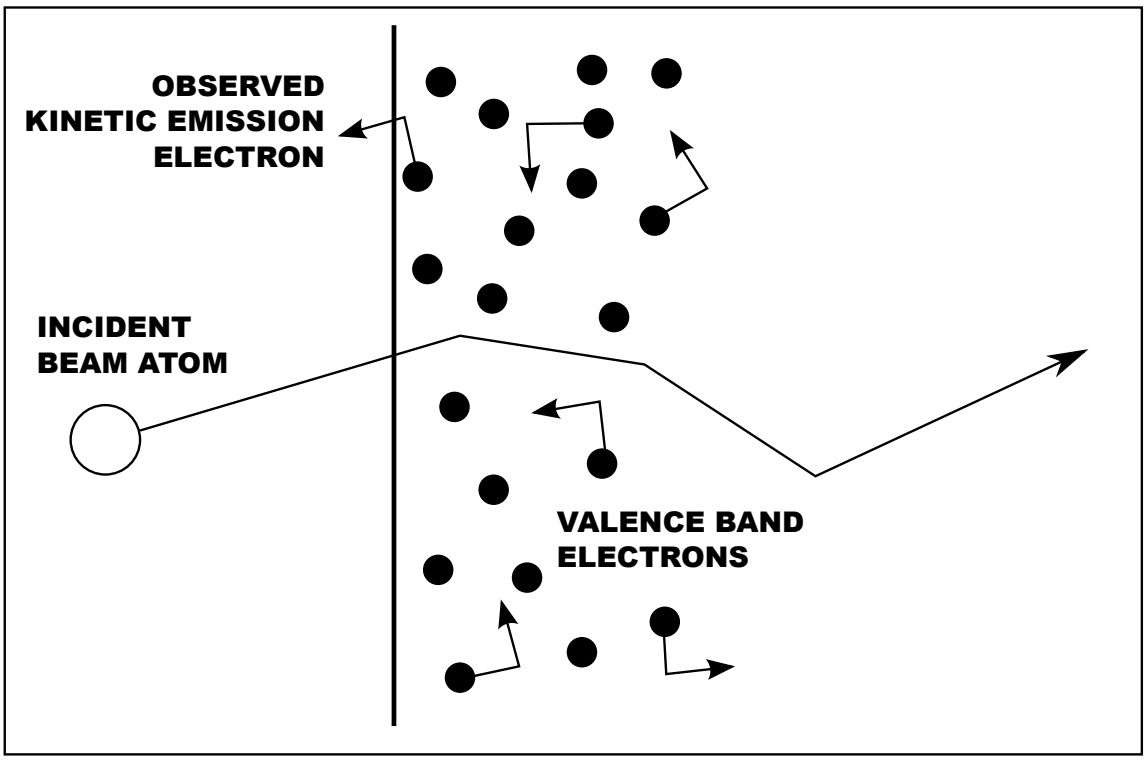

Figure 2.5: Schematic of the KE process in which an incident projectile atom penetrates a material surface, interacting with valence band electrons and resulting in at least one emitted electron.

emitted energy distribution is also related to material properties but is found to be independent of projectile properties [10]. Complete treatment of the total KE yield and EEDF should also take into account material temperature and incidence angle dependence [98, 99] but are left out for simplicity in this analysis and implementation.

2.3.2.1 KE Total Yield

The total yield (γ) of electrons emitted from a solid surface per impacting atom is defined as

$$\gamma = \frac{\Gamma_e}{\Gamma_i} \tag{2.21}$$

where Γ_e and Γ_i are the corresponding fluxes of emitted electrons and impinging atoms at the target surface, respectively. The reason for choosing atoms instead of ions is discussed near the end of this section. This formulation of KE is slightly different than the total yield of the PE process found in Equation 2.11 due to the fact that a "current" does not exist for a flux of neutral particles. The total yield of KE is introduced by first establishing that there exists a threshold energy at which electrons will be emitted via kinetic processes. The maximum energy transferred between a projectile ion and target electron (E_T) is derived from the free-electron model [100] and defined as,

$$E_T = 2m_e v_i(v_i + v_F) \tag{2.22}$$

with m_e as the electron mass, v_i as the projectile ion velocity, and v_F as the Fermi velocity, the average velocity of free electrons in the valence band structure of the surface. Using the Fermi velocity for iron [86], $v_F \simeq 1.98 \times 10^6$ m/s, and varying the impacting energies as 0.073-1500 eV for the various states of low- and high-energy xenon ions of our system, corresponding to $v_i \simeq 327$ m/s to 4.69×10^4 m/s, we arrive at maximum transferred energy values of 0.007 eV to 1.08 eV.

If a relationship is to be found for the minimum threshold projectile velocity

($v_{i,th}$) to emit an electron at a surface, the maximum threshold is replaced by the surface work function (W_ϕ) and the relationship is solved for velocity which appears in quadratic form,

$$\frac{W_\phi}{2m_e} = v_{i,th}^2 + v_{i,th}v_F \ . \tag{2.23}$$

For stainless steel, the threshold velocity is found to be $v_{i,th} = 1.7 \times 10^5$ m/s, which is much larger than the maximum velocity of the impinging xenon ions in our system. However, despite this very high threshold value, electrons emitted by KE are still always observed in systems in which velocities are below this supposed threshold [87]. The disparity arrives in the inability of the free electron model to account for elastic collisions between valence-band electrons and the lattice structure of the material, leading to a drastic lowering of the threshold energy level [101, 100]. Therefore, we instead rely on the total yield (γ_k) calculated from both projectile and material parameters to determine how electrons are emitted at the stainless steel surface.

There are multiple ways to approach the calculation of the total yield. A first attempt will be to approach the material parameters directly, despite a lack of precise material data, focusing on the stopping power. The stopping power can be considered as the average energy loss per unit distance of the projectile traveling through the solid medium. Two different stopping powers are taken into account in the KE process, the stopping power of the projectile impacting and traveling through the target ($(dE/dx)_p$) and the stopping power of the electrons which are diffused into vacuum through the valence band of the target ($(dE/dx)_e$). Specifically, the electronic stopping power is considered as opposed to the nuclear stopping power, and is defined as (for instances of electrons, "e", and projectiles, "p")

$$\left(\frac{dE}{dx}\right)_{e,p} = -N_m S_{e;e,p} \ , \tag{2.24}$$

with the average atomic density of iron or stainless steel [86], $N_m \simeq 8.52 \times 10^{28}$ m^{-3}

and the stopping "cross-section", $S_{e;e,p}$.

The stopping cross-section for projectiles ($S_{e,p}(E)$) was proposed by Lindhard and Scharff [102] and is used widely in similar gas-material systems [103]. $S_{e,p}(E)$ is calculated as follows,

$$S_{e,p}(E) = 1.21 \frac{Z_{Xe}^{7/6} Z_{Fe}}{(Z_{Xe}^{2/3} + Z_{Fe}^{2/3})^{3/2}} \sqrt{\frac{E}{M_{Xe}}} \ , \tag{2.25}$$

using the atomic numbers of xenon and iron, $Z_{Xe} = 54$ and $Z_{Fe} = 26$, respectively, and the atomic mass of xenon $M_{Xe} = 131.29$ amu. For an average impact energy of 1.5 keV, the stopping cross-section for xenon onto a stainless steel (or iron) target is calculated to be $S_{e,p} = 100.8$ eV·Å^2 $= 1.01 \times 10^{-18}$ eV·m^2. Using this and the atomic number density of the material, we arrive at a projectile stopping power of $(dE/dx)_p = -8.61 \times 10^{10}$ eV/m $= 8.61$ eV/Å.

The concept of a low-energy electronic stopping power for electrons escaping from the surface, as opposed to projectiles impinging onto the surface, was first proposed by Bethe [104]. Ashley, et al. [105], used statistical models to study the low-energy electronic stopping power for diffusing electrons in various metals with the majority of data compiled in Reference [86]. However, electronic stopping power for stainless steel or iron remains to be gathered. A conservative representative stopping power interpolated from values of slightly more dense metals (Ni and Cu) gives $(dE/dx)_e \simeq$ 5 eV/Å.

An exact relation for the total KE yield described in terms of electron-surface transport has been a major topic of interest for the past 50 years and has resulted in both semi-empirical and theoretical descriptions [106, 107, 108]. The model of Schou [10] became the most broadly-used, describing total KE yield as

$$\gamma_k = \Lambda_m \, \beta \left(\frac{dE}{dx} \right)_p \ , \tag{2.26}$$

a simple equation containing the two sets of required information for yield: the properties of the material's "specific yield" (Λ_m) and the properties of the projectile found in the stopping power. The equation uses a fitting-factor (β) for extra phenomena, such as recoiled and backscattered ions, and can be estimated to be $\beta \simeq 0.1$ for the situation of heavy particles impacting on heavy target atoms, as described by Schou [109]. The material specific yield, Λ_m, can now be evaluated using Schou's simplified description [10] as,

$$\Lambda_m = \frac{\Gamma_m}{8\,(dE/dx)_e}\ , \tag{2.27}$$

with $\Gamma_m = 0.6079$ resulting from the assumption that the average projectile impact energy is much greater than the surface barrier, $E_i \gg U_0$, with the barrier U_0 equal to the superposition of the Fermi energy and work function, $U_0 = \epsilon_F + W_\phi = 15.25$ eV. This is true for the case of 1.5 keV impacting xenon ions and leads to a calculated material specific yield of $\Lambda_m = 7.6 \times 10^{-2}$ Å/eV. Putting these values and the two stopping powers into Equation 2.26 for total KE yield leads to an estimation of approximately 0.01. However, it is shown later in this work that this yield is too large and, therefore, more specific material information is required if this method is to be used accurately.

The work of Alonso et al. [100] and Winter et al. [110] give a KE yield which is of a lower magnitude and more appropriate for the present study. Alonso studied the interactions of heavy ions with aluminum surfaces in order to build a better description of activation, or threshold, energies for the KE process. It was found that the effects of L-shell interactions and high-energy recoil atoms at the surface brought the KE threshold energy into the range of approximately 1.6 to 3 keV, providing a lower limit to the range of allowable emission threshold energies. Therefore, only atom wall-fluxes above 1.6 keV will be considered to activate the KE process in the

present study. While the Test Cell's ion beam is injecting xenon ions at 1.5 keV, it will be shown in Chapter V that projectiles with a larger magnitude energy are observed resulting from a combination of MEX and CEX collisions.

Winter [110] then analyzed charged and neutral heavy and light species impacting on gold with an emphasis on relatively low-energy impact energies, approximately 0.1 to 10 keV, resulting in a total yield of approximately $\gamma_k = 0.0001$. Additionally, other physical phenomena have the effect of reducing the yield even further. It was observed that neutral projectile penetration resulted in about one-third of the charged-particle yield due to fundamental differences between neutral and charged particle penetration through a surface lattice [110]. Furthermore, the lack of many of the required fundamental parameters for stainless steel and its existence as an alloy rather than a pure metal (the usual focus on PIE experiments) is hypothesized to lower the yield another order of magnitude.

These assumptions and parameters are condensed into a final total yield for the KE process which is dependent on high-energy atoms. This choice of atoms instead of ions is due to the fact that a much higher magnitude of high-energy atom flux arrives at the KE-emitting region than high-energy ion flux. This is related to the mean free paths and lifetimes of each of these populations of species and discussed later in Sections 5.1.1 and 5.3.1. A final KE yield for high-energy atoms of approximately $\gamma_k = 3 \times 10^{-6}$ is then established. This very low yield can be attributed to the fact that fluxes are used in these KE yield calculations as opposed to currents and include threshold-level flux-fraction information for high-energy atoms. Due to the compounding assumptions and inclusion of these threshold levels, sensitivity analyses are carried out for these corrective factors in Section 5.4.

Lastly, it should be mentioned that, historically, the interplay of KE and PE at high kinetic energies has been difficult to study experimentally [111, 112, 110] and it will be assumed for this work that the processes are independent, discussed later in

the numerical implementation of PIE physics.

2.3.2.2 KE Emitted Electron Energy Spectrum

Introduced earlier, the energy distribution curve is a differential distribution of the measure of emitted electrons similar to an EEDF and will be referred to as the kinetically emitted electron energy distribution function (KE EEDF) as we are primarily interested in the probability of an electron emitted with a certain energy from the surface.

The shape of the KE EEDF shows good repeatability of data for various metals and various projectile energies in both experimental and theoretical contexts [9, 13, 10, 113, 11, 12]. The KE EEDF is commonly described as having a large peak in the few-eV range and then a monotonically decreasing tail extending no further than 15-20 eV [114]. The full-width half-maximum of the KE EEDF was originally thought to decrease with increasing projectile energy [9, 13] but was later accepted as being defined by the surface barrier of the material [10].

There is once again a lack of data for xenon-induced KE from iron or stainless steel so, similar to the PE EEDF process, a model must be used to describe the surface properties of the target and the KE EEDF. Therefore, a "non-central χ^2 distribution" [94] with degrees of freedom $\nu = 5$ and non-centrality parameter $\lambda = 0.1$ is used to mimic the shape of a KE EEDF. This leads to a KE EEDF with a mean of $\mu = \nu + \lambda = 5.1$ eV and a standard deviation of $\sigma = \sqrt{2\nu + 4\lambda} = 3.23$ eV. The non-central χ^2 distribution is described in terms of energy as

$$P_k(E) = 2^{-\nu/2}\, e^{\frac{-(\lambda+E)}{2}}\; E^{\frac{\nu}{2}-1}\; {}_0\tilde{F}_1\left(;\frac{\nu}{2};\frac{\lambda E}{4}\right)\;, \tag{2.28}$$

where ${}_0\tilde{F}_1\left(;\frac{1}{2}\nu;\frac{1}{4}\lambda E\right)$ is the regularized confluent hypergeometric function [115]. The resulting distribution can be seen in Figure 2.6 alongside historical KE EEDF data

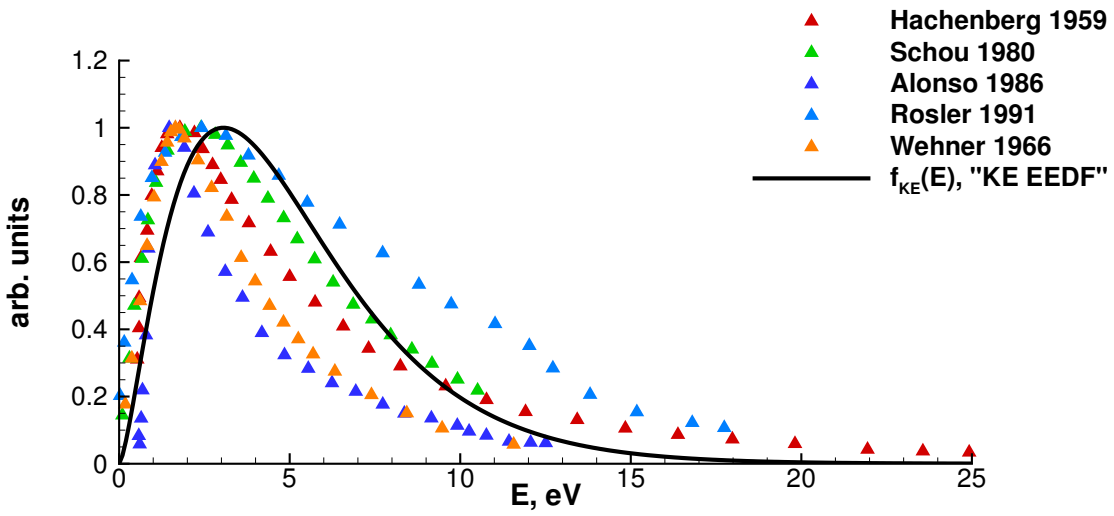

Figure 2.6: Normalized non-central χ^2 distribution next to previously cited historical KE EEDF data for for various species and metals [9], generalized theoretical results [10], 0.5 eV Xe on Au [11], Monte Carlo simulation [12], and 10 eV Ar on Mo [13].

for the before-mentioned values of ν and λ.

2.3.3 Electron-atom interactions

Once the secondary electrons are emitted, a simple collisional model must be implemented in order to simulate the collisions of electrons with the heavy species in the Test Cell environment. Past kinetic treatments of electrons in a similar electric propulsion environment [34] have focused on elastic, ionization, and excitation collisions between electrons and atoms. However, due to the low densities and energies of the secondary electron populations in the Test Cell, only elastic scattering collisions are taken into account.

Total collision cross-sections for elastic electron-atom interactions (σ_{el}) are calculated using a fifth-order polynomial function proportional to the square root of the

e-Xe interaction energy ($\sqrt{E}$),

$$\sigma_{\rm el}(\sqrt{E}) = -0.60(\sqrt{E})^5 + 8.89(\sqrt{E})^4 - 48.85(\sqrt{E})^3 \quad (2.29)$$

$$+ 117.07(\sqrt{E})^2 - 106.86\sqrt{E} + 39.16 \text{ Å}^2 , \quad (2.30)$$

fit to data by Ramsauer et al. [116, 117] and Dababneh et al. [118] for e-Xe collision energies $E \leq 30$ eV. These collisions result in an isotropically-scattered electron with the target xenon atom relatively unchanged due to the difference in mass and momentum.

2.4 Summary of transport theory

The underlying transport physics used in the simulation of collisions and emission in the Test Cell have been described in this chapter. The complete set of transport models can be summarized in the following collision model reactions (taking note of collision energies when special treatment is required),

$$\mathrm{Xe} + \mathrm{Xe} \xrightarrow{\text{VHS}} \mathrm{Xe} + \mathrm{Xe} \quad (2.31)$$

$$\mathrm{Xe} + \mathrm{Xe}^+ (E \simeq 1.5 \text{ keV}) \rightarrow \begin{cases} \xrightarrow{\text{MEX}} \mathrm{Xe} + \mathrm{Xe}^+ (E \simeq 1.5 \text{ keV}) \\ \xrightarrow{\text{CEX}} \mathrm{Xe}^+ + \mathrm{Xe} (E \simeq 1.5 \text{ keV}) \end{cases} \quad (2.32)$$

$$\mathrm{Xe} (E \geq 1.6 \text{ keV}) + \mathrm{SS} \xrightarrow{\text{PIE}} \mathrm{Xe} + \mathrm{e}^-_{\mathrm{KE}} \quad (2.33)$$

$$\mathrm{Xe}^+ + \mathrm{SS} \xrightarrow{\text{PIE}} \mathrm{Xe} + \mathrm{e}^-_{\mathrm{PE}} \quad (2.34)$$

$$\mathrm{e}^- + \mathrm{Xe} \xrightarrow{\text{elastic}} \mathrm{e}^- + \mathrm{Xe} \quad (2.35)$$

including atom-atom VHS collisions in reaction 2.31, atom-ion MEX/CEX collisions in reactions 2.32 and 2.32, the electron emission from stainless steel (SS) models of reactions 2.33 and 2.34, and the simple elastic scattering of electrons in reaction 2.35.

The approach for numerically implementing these transport models is described in

Chapter III, explaining the isotropic and anisotropic treatments of the heavy species collision models as well as the secondary emission of electrons from the electrodes.

CHAPTER III

Numerical Implementation of Transport Models and the Experimental Domain

This chapter describes the numerical implementations of the theoretical models of Chapter II. Details of the DSMC-PIC methodology and simulation code are described in Section 3.1. The UCLA Test Cell is then described numerically in Section 3.2. The method for solving the non-neutral electric potential fields in the Test Cell using the Poisson equation is detailed in Section 3.3 and the numerical implementation of the heavy species collision models is outlined in Section 3.4. Lastly, the numerical application of the particle-induced electron emission theory is detailed in Section 3.5.

3.1 The DSMC-PIC technique

The simulation approach used in this study involves a particle-based direct simulation Monte Carlo (DSMC) [16] method capable of simulating nonequilibrium, rarefied flows with a particle-in-cell (PIC) algorithm [33] allowing for the treatment of plasma effects.

3.1.1 MONACO-PIC

The particular simulation code used in this work is MONACO-PIC which utilizes the DSMC-PIC method. The DSMC portion, described in Section 3.1.2, was originally developed by Dietrich and Boyd [119] in 1996 and the PIC element, described in Section 3.1.3, was developed by Cai [120] in 2005. MONACO-PIC is written in both C and C++ and has the ability to simulate axi-symmetric flows on both structured and unstructured meshes. Past applications of MONACO-PIC have resulted in plume solutions for SPTs [120, 15] and TALs [121].

3.1.2 The direct simulation Monte Carlo (DSMC) method

The DSMC method is the most commonly used particle simulation technique for rarefied gas flows [16]. First introduced by Bird [32] in the 1960s, the method has become widely developed and largely accepted in the scientific community. The DSMC method uses numerical macroparticles which represent a larger number of real molecules and is a more efficient method than other kinetic methods such as the molecular dynamics technique which simulates interactions between all real particles. The DSMC technique has been applied and described widely in the literature for various applications [122, 123, 124, 125].

An important feature of the DSMC method is the ability to reproduce the non-linear Boltzmann equation [126, 127] via the simulation of real molecules and their positions, velocity distributions, and collisions, all determined from basic kinetic theory of a rarefied gas. Bird showed [128] that solutions of the Boltzmann equation can be reproduced via an application of the DSMC technique.

3.1.2.1 The DSMC algorithm

The DSMC technique begins by partitioning the computational domain into cells whereby these cells serve as individual regions of molecular interaction as well as for

the sampling of macroscopic information. These cells are sized in order to resolve the mean free path (λ), the mean distance between collisions, introduced in Section 2.1. In certain cases there are instances of DSMC not requiring a subdivision of cells, called "gridless DSMC" [129], which is not the topic of this work. Similar to other numerical techniques, DSMC utilizes a time step (Δt) to calculate the movement of particles through the domain of cells. This time step is set to be smaller than the mean collision time of molecules, related to λ. The domain is established as a system of macroparticles with unique positions and velocities. The following computational tasks are performed each iteration:

1. Iterate through macroparticles and select pairs which are marked as "colliding" via the methodology of Section 3.4. This step uses a combination of stochastic and physics-based models to replicate the actual collision process.

2. Perform binary collisions taking into account conservation of momentum and energy. The collision cross-sections from Section 2.2 are utilized in these calculations.

3. Inject newly created particles due to physical inflows at numerical boundaries marked as an inlet. Macroparticles are created via a specified flux calculated from kinetic theory and an assigned weighting representing the real-to-macroparticle ratio.

4. Move particles according to the translation energy resulting from initial velocities plus any additions or subtractions due to collisions. In this step, particles may move from cell to cell or from cell to boundary, in which either reflection, adsorption, or an escape from the domain is simulated.

5. Lastly, flow properties are sampled.

Step 5 is only reached if the system has reached steady state. The DSMC algorithm is essentially used in the pairing of all particles though the treatment of cross-sections and post-scattering collision properties are treated differently depending on atom-atom or atom-ion interaction, as described in Sections 3.4.

3.1.3 The particle-in-cell (PIC) method

The PIC method is a kinetic particle method, similar to DSMC, which tracks the motions of charged macroparticles [130]. Expanded and popularized greatly by Birdsall and Langdon [131] in the 1990s, the method has been widely expanded to such applications as ion thrusters [132], HETs [120, 121, 15], and plasma-surface interactions [133] which often include an algorithm for the treatment of particle collisions such as DSMC or a simplified Monte Carlo collision (MCC) algorithm [134].

The PIC methodology is developed around the fundamental idea that a plasma is a collection of finite, charged particles which can interact not only with each other but also with externally applied fields. Maxwell's equations are used to calculate self-consistent electromagnetic fields throughout the domain. Particle trajectories can be affected by these external electromagnetic forces using Newton's laws. Similar again to DSMC, the domain is divided into cells which, for PIC, are not for pairing but for the collection of field information at discrete locations for the solving of self-consistent electric fields within the domain. For this particular implementation of PIC, effects due to magnetic fields are not considered.

These fields are solved by collecting the local charge densities at the nodes between cells and solving a discretized equation for electric fields and particle trajectories through the cells. The particles occupy a position within the cell and correspond to a portion of the current density due to the cell volume which is represented numerically by the cell's position. During the course of one iteration, forces on these particles are calculated due to the electric fields located at the nodes and the particles' velocities

are updated. The process repeats as the following computational tasks are performed each iteration:

1. Iterate through cells and particles to obtain charge densities on the cell nodes due to the distributions of particles within the cells. Calculate the electric potential (ϕ) due to this charge distribution using the method described in Section 3.3.

2. Calculate the electric field ($\vec{E}$) by differentiating the electric potential field spatially, $\vec{E} = -\nabla\phi$.

3. Convert $\vec{E}$ to an electrostatic force and iterate through all particles, updating their velocities due to accelerations from this force.

4. Move particles using updated velocities.

5. If a collision algorithm is specified, such as a DSMC or MCC method, perform collisions and further update particle momenta and energies.

These steps are repeated as charged particles move through the domain, changing the charge and field distributions.

Lastly, much like DSMC, there are certain requirements related to the numerical domain which must be satisfied for PIC. Firstly, the time step must be small enough to resolve the plasma frequency (ω_p), defined in the context of ions for this work as [135],

$$\omega_p = 210 \times Z \times \sqrt{\frac{n_i[\ \mathrm{m}^{-3}]}{\mu}}\ \mathrm{rad/s}\ , \tag{3.1}$$

using ion charge number (Z), ion number density (n_i), and ion reduced mass as protons (μ), $\mu = m_i/m_p$. Details of these values are given in Section 3.2.

Additionally, for a non-neutral plasma, the PIC domain must be able to spatially resolve the plasma flow by using cells which are smaller than the Debye length (λ_D).

The Debye length is the distance around a charge at which shielding occurs by other charged particles and is defined, again in terms of ions, as [135]

$$\lambda_D = 7.43 \times 10^3 \sqrt{\frac{T_i[\text{ eV}]}{Z\ n_i[\text{ m}^{-3}]}}\ \text{m}\ . \tag{3.2}$$

The Debye length must be resolved with smaller-sized cells because it is a measure of the maximum distance that information about a particles charge can be observed; if the cell size is larger than λ_D, the plasma will show a shielding distance according to the larger spatial resolution and thus show a λ_D which is too large and representative of a plasma which has too large of a temperature (T_i) or too small of a density (n_i). Again, details of these values are given in Section 3.2.

3.1.4 Numerical weighting of particles

Particle weighting is an important aspect of the present work due to the density disparities between ion beam and background gas of the Test Cell. It would be nearly impossible to resolve trace species without the ability to weight macroparticles so that they have similar population "sizes" numerically while still representing large disparities in terms of real particle densities.

Each particle injected into the domain is assigned a relative macroparticle weight (W_p). Overall particle weight is calculated by multiplying W_p by the local cell weight (W_c). Particles travelling across cells may be subject to cloning or destruction due to the need to match weights through the domain as W_p remains constant. Collisions between macroparticles with different weights result in the splitting of the macroparticle with the larger weight into two smaller macroparticles: one which is identical to the colliding particle weight and one which is the leftover weight from the subtraction. This is performed so that momentum and energy are correctly conserved.

3.1.5 Treatment of boundary conditions in DSMC-PIC

The treatment of macroparticles as they interact with the numerical boundaries of the simulation depends on the type of specified condition at the boundary. Boundaries marked as an "outflow" result in the deletion of the macroparticle. Boundaries marked as "symmetry" result in a specular reflection of the macroparticle. Boundaries marked as a "wall" result in macroparticles which are reflected either diffusely or specularly, specified by the boundary parameters, resulting in different behaviors of the macroparticle's normal velocity (u_n) and tangential velocity (u_t).

Macroparticles which are reflected specularly result in a change of sign for the normal velocity component of the macroparticle while the tangential component remains unchanged. Macroparticles which are reflected diffusely from a wall with a specified temperature (T_w) are sampled from a biased Maxwellian distribution in the normal direction as

$$f(u_n)\mathrm{d}u_n = \frac{1}{2RT_w} u_n e^{\left(\frac{-u_n^2}{2RT_w}\right)} \mathrm{d}u_n \ , \tag{3.3}$$

and sampled from a Maxwellian distribution in each tangential direction as

$$f(u_t)\mathrm{d}u_t = \frac{1}{\sqrt{2RT_w}} e^{\left(\frac{-u_t^2}{2RT_w}\right)} \mathrm{d}u_t \ . \tag{3.4}$$

The choice between specular or diffuse interaction depends on the specified wall's accommodation coefficient (α). The accommodation coefficient describes the fraction of reflected particles which are thermalized to the temperature of the wall and reflected diffusely; the leftover amount of $(1-\alpha)$ is the fraction of specularly reflected particles. The present work uses an accommodation coefficient of $\alpha = 1$ and a temperature of $T_w = 300$ K for all walls.

All boundary types may also be assigned an electric potential condition, ϕ. A Dirichlet condition will result in the boundary being assigned a constant value of ϕ while a Neumann condition will result in the boundary being assigned a constant

gradient, $\nabla\phi$. Walls are typically specified with a Dirichlet condition while inflow, outflow, and symmetry conditions will typically be specified with a Neumann condition.

The details of the chosen electric potential boundary conditions are described in Section 3.2 while the detailed solution of the electric potential from the Poisson equation is described in Section 3.3.

3.2 Numerical description of the UCLA Test Cell

The experimental setup which is the focus of this simulation study is previously described by Wirz, et al. [37, 38, 39, 40], as introduced in Section 1.2.4. The facility is modeled numerically using a simplified and well-defined axi-symmetric domain and structured mesh, seen in Figure 3.1. The domain, named the "Test Cell", is 152 mm long and 48.26 mm in diameter with an inlet used for particle injection, an outlet for particle exit, and a line of rotation along the axis.

As noted in Figure 3.1, the two regions of particular interest are the Inner Cylinder (IC) and the Exit Plate (EP), representing electrically isolated surfaces on which current is measured in the UCLA experiments. The large aspect ratio of the Test Cell is designed to separate current collection from low-angle and high-angle scattering events between atoms and ions, described in Section 2.2.2. In addition, the measurements include the current exiting the domain through the outlet as the Exit Orifice (EO). The currents measured on the Inner Cylinder, Exit Plate, and Exit Orifice are available in datasets provided by UCLA which are compared to simulations.

The collisions which lead to impact with the facility surface in these simulations are momentum exchange (MEX) and charge exchange (CEX) interactions between Xe and Xe^+ particles, illustrated in Figure 3.2. MEX collisions result in high-energy xenon ions striking the Exit Plate while CEX collisions result in high-energy neutral

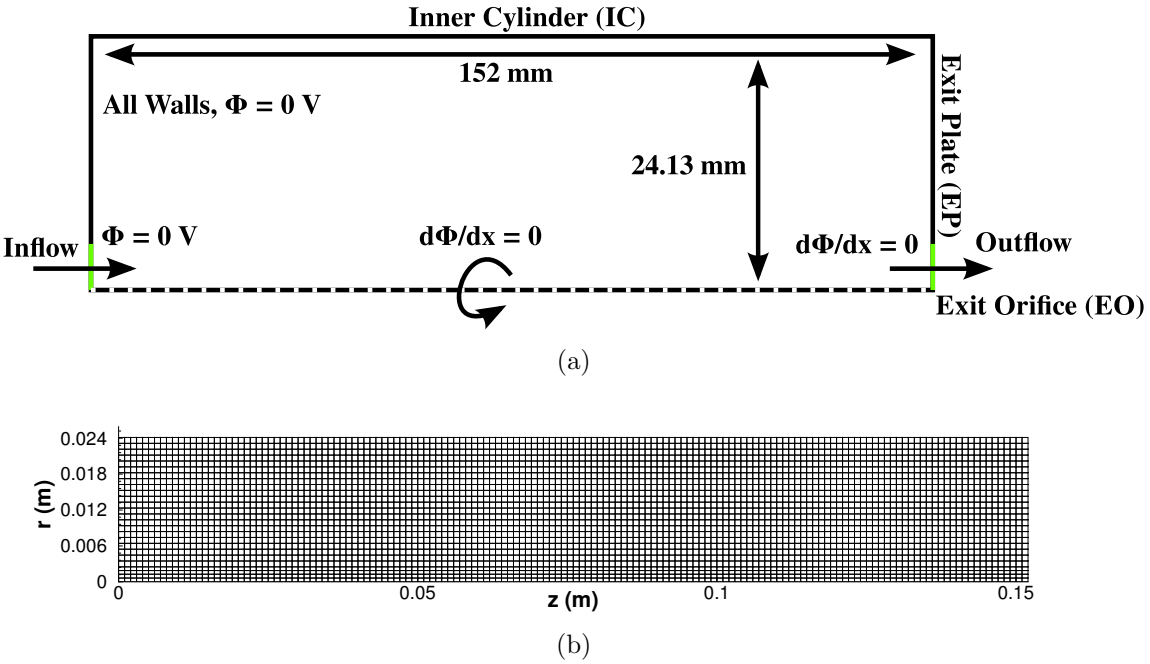

Figure 3.1: Numerical domain of the UCLA experiment, detailing inlet, outlet, symmetry conditions, potential conditions at the walls, and current collecting surfaces Inner Cylinder, Exit Plate, and Exit Orifice in (a) and a to-scale corresponding structured mesh in (b).

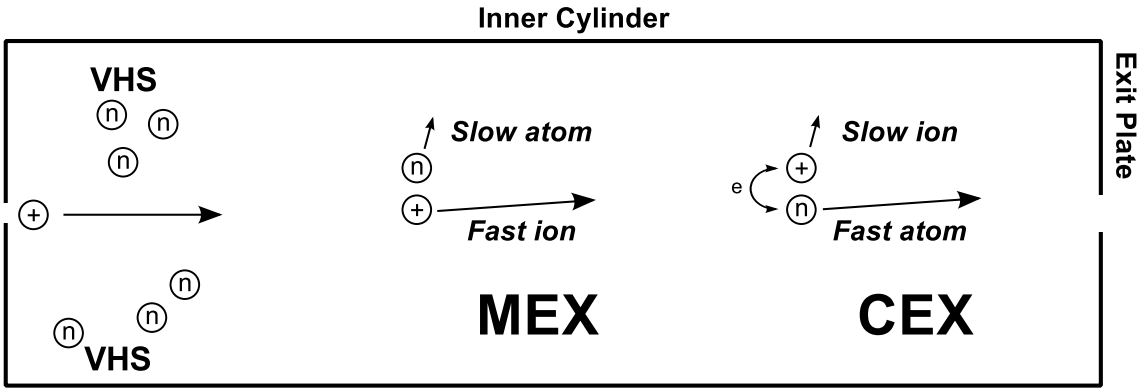

Figure 3.2: Approximately to-scale illustration of the Test Cell and the two processes, MEX and CEX, which create populations of low- and high-energy xenon ions and atoms at both low and high angles.

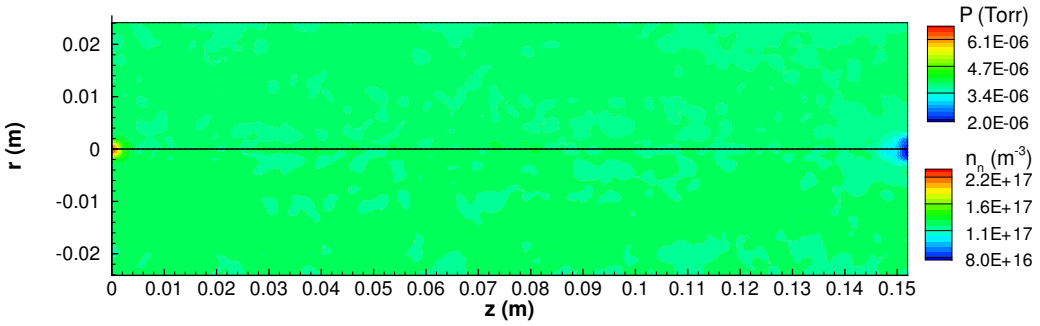

Figure 3.3: Simulated atom number density and pressure contours for the lowest operating conditions of the Test Cell for DSB, illustrating a typical steady state neutral xenon solution for a target pressure of $3.2\times10^{=6}$ Torr.

xenon striking the Exit Plate and low-energy xenon ions striking the Inner Cylinder. The total cross-sections of each interaction are considered equal yet the nature of the differential cross-sections results in this low-angle/high-angle behavior. These specific interactions are essential to the characterization of PIE as they are the source of the two xenon populations of interest: low-energy ions on the Inner Cylinder and high-energy atoms on the Exit Plate, discussed in Section 2.3.

The measured data from UCLA are organized into four sets: Data Sets A (DSA) and B (DSB), the unbiased Test Cell data, and Data Sets C (DSC) and D (DSD), the biased Test Cell data. "Unbiased" and "biased" refers to the application of an applied voltage to the Inner Cylinder in certain operating conditions. Each data set has a unique amount of total current within the Test Cell which is previously recorded experimentally and then simplified using a curve-fit for numerical input. These experimental data were recorded at four different times and at four different conditions, details of which can be found in the previously cited work of Wirz, et al. The details of the operating pressures and total currents as utilized by this work are found in Appendices A through D as applied to previous work [60, 136].

A typical Test Cell simulation is first populated with neutral particles until the target background pressure is achieved after which the beam ions are injected. Fig-

ure 3.3 shows an example of a low-pressure, steady state, background xenon atom solution of the Test Cell. The simulation is allowed to reach a steady state after which time-averaged solutions are generated. A typical ion beam simulation is made up of about 300,000 particles with a domain of about 4,000 cells. Using the conditions specified in the Appendices, λ for atom-ion collisions ranges from approximately 10 mm to 4 m according to Equation 2.2 and λ_D ranges from approximately 3 mm to 8 mm according to Equation 3.2. The cells are structured quadrilaterals with sides of $\simeq$ 1 mm, a condition which satisfies the λ and λ_D requirements of Sections 3.1.2 and 3.1.3.

All walls and the inlet are assigned a Dirichlet boundary condition using a potential of 0 V for the unbiased test cases. The axis of rotation and outlet are defined by a Neumann boundary condition using a zero gradient in potential, normal to the boundary. This numerical domain is held constant for all simulations except for the bias voltage at the Inner Cylinder which is adjusted positively and negatively for the biased data sets. A timestep of $3{\times}10^{-8}$ s is used for a typical run of 600,000 timesteps which takes between 6 to 10 hours of wall time on 4 processors. Again, from the conditions found in the Appendices, an average ω_p for the Test Cell ion beam is approximately 1×10^7 s^{-1}, according to Equation 3.1, which is representative of a timescale of 1×10^{-7} s, a condition which is resolved by the previously-mentioned choice of timestep. Furthermore, the previously established range of mean free paths can be divided by the average velocity of the atom-ion interactions, 1.5 keV $\simeq$ 46,900 m/s, to again arrive at a minimum mean collision time of 1×10^{-7} s, similar to the value associated with ω_p that is resolved well.

For electron emission simulations, described further in Section 3.5, the time step is decreased to 3×10^{-12} s, leaving heavy species essentially motionless as the fast, light electrons are emitted from domain walls and simulated for another 500,000 timesteps until the solution reaches steady state. In addition, when referring to electron runs,

"unbiased" refers to Data Set A and "biased" refers to Data Set C.

3.3 Direct solution of Poisson's equation for electric potential

In order to correctly simulate the biased walls of the Test Cell, the electric potential solver of MONACO-PIC is advanced from a quasineutral assumption to a direct solution of Poisson's equation derived from the difference in charge density of ions and electrons. This is an important advancement for the simulation of the Test Cell which is composed primarily of a non-neutral ion beam.

3.3.1 Previous quasineutral implementations

The original quasineutral models used in past implementations of MONACO-PIC are the Boltzmann relation and a detailed electron-fluid model [120, 121, 15]. The Boltzmann relation is a solution of the electron momentum equation derived using some nontrivial assumptions: the fluid electron flow is isothermal, electron pressure obeys the ideal gas law, and magnetic fields can be neglected. Since the electrons have constant temperature, the pressure gradient and electric forces in the electron momentum equation are balanced and the potential, ϕ, at any point is then:

$$\phi = \phi_r + T_e \ln\left(\frac{n_e}{n_r}\right), \tag{3.5}$$

with ϕ_r and n_r as reference electric potential and density, respectively, and are chosen to match the input conditions of the domain.

The Boltzmann relation is used for comparison purposes in Section 4.1.1 and is configured to use the beam injection inlet as the reference location. While the density of the ion beam changes based on operating condition, the reference potential is set to 0 V at the inlet. In addition, T_e is the electron temperature in eV, and n_e is the

electron number density. For these simulations, T_e is set to the injection temperature of the ion beam, 296 K, and n_e is set to ion number density, n_i, throughout the simulation using the assumption of quasineutrality.

3.3.2 *A priori* assumptions of non-neutrality

Any quasineutral model, however, is inherently inappropriate for the Test Cell and its ion beam as the assumption of a quasineutral mixture of ions and electrons is not valid for ion-only injection. In addition, the Boltzmann relation is unable to recognize electric potential boundary conditions within the domain, instead solely using the reference potential. An important aspect of the Test Cell is the ability to vary the voltage on the Inner Cylinder in order to observe ion collection and repulsion and secondary electron collection. As an alternative to the Boltzmann relation, the Poisson equation is solved directly from ion charge density without any quasineutral assumptions about the plasma. The Poisson equation is represented in cylindrical coordinates as

$$\nabla^2\phi = \frac{1}{r}\frac{\delta}{\delta r}\left[r\frac{\delta}{\delta r}\phi(r,z)\right] + \frac{\delta^2}{\delta z^2}\phi(r,z) = \frac{q}{\epsilon_0}\left(n_i - n_e\right) \ . \tag{3.6}$$

This non-neutral method has the ability to use all electric potential boundary conditions as well as the ability to include electrons in a non-quasineutral way, such as through their secondary production due to particle-induced electron emission.

3.3.3 The finite-element implementation of a generalized Poisson equation

Equation 3.6 can be expressed as a generalized Poisson equation in cylindrical coordinates with a source term,

$$-\nabla\left[P(r,z)\cdot\nabla Q(r,z)\right] = S(r,z) \ , \tag{3.7}$$

with $P(r,z)$ as a distribution of coefficients, $Q(r,z)$ as a distribution of solved-for primary variables, and $S(r,z)$ as a known distribution of source terms. A finite-element solver developed by Cai [120] was originally used to solve for a detailed fluid-electron model [121, 15], representing continuity, momentum, and energy as generalized Poisson-like formulas. This solver is modified [136] to solve for Equation 3.6 using structured or unstructured axi-symmetric meshes. The solver uses only direct charge density values from ions and electrons for $S(r,z)$. A more detailed description of the exact implementation of the generalized solver can be seen in Reference [120].

3.3.4 Electric potential solver validation

The Poisson solver is validated using an exact solution of a one-dimensional Laplace's equation. The Poisson equation takes the form of the Laplace equation in the presence of zero charge density and can be easily solved analytically, i.e.,

$$\nabla^2\phi = 0 \;\rightarrow\; \phi = Ax + B, \tag{3.8}$$

making for an ideal, simple test case to ensure that the finite-element solving method is in working order. Using a one-dimensional domain with $\phi = 200$ V at $x = 0$ and 0 V at $x = L$, the coefficients are found to be $B = 200$ V and $A = -200$ V$/L$. The results of the test case, plotting both simulation and the exact solution, can be seen in Figure 3.4 where the Poisson solver matches exactly the theoretical solution.

3.4 Numerical implementation of heavy species collisions

This section outlines the numerical implementation of the heavy species collision models detailed in Section 2.2, describing isotropic atom-atom interactions in Section 3.4.1 and anisotropic atom-ion interactions in Section 3.4.2.

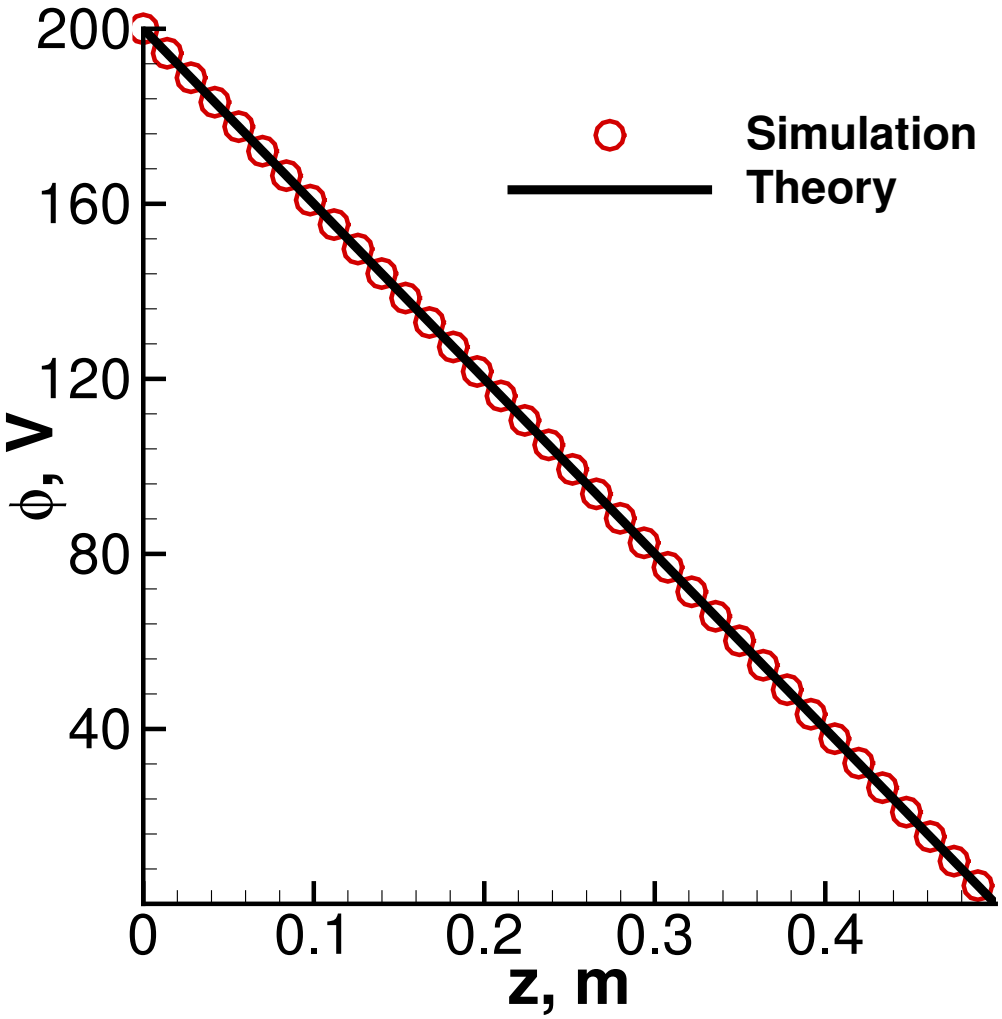

Figure 3.4: Results of the 1-d Laplace's equation validation test showing good correlation between simulation and theory.

3.4.1 Isotropic atom-atom interactions

Collisions between neutral xenon particles are evaluated by pairing randomly selected numerical xenon atom macroparticles in each cell regardless of position of velocity of the macroparticles. The total number of pairs required per timestep is calculated using Bird's No-Time-Counter (NTC) scheme [16],

$$\#\text{ of pairs} = \frac{N\bar{n}}{2}(\sigma_{\text{VHS}}g_r)_{\max}\Delta t \ , \tag{3.9}$$

which uses a multiplication of the instantaneous number of simulated molecules (N) and ensemble-averaged number density ($\bar{n}$), time step (Δt), and the maximum local product of the relative velocity and cross-section. While Equation 3.9 governs the number of pairs selected, actual events are determined through a calculation of the collision probability (P_{VHS}) on a per-collision basis. This probability is computed as the ratio of the instantaneous value of ($\sigma_{\text{VHS}}g_r$) of the selected pair to the maximum value of ($\sigma_{\text{VHS}}g_r$) for all pairs in a given cell and then compared to a random number (R) uniformly distributed in $[0, 1]$,

$$P_{\text{VHS}} = \frac{(\sigma_{\text{VHS}}g_r)}{(\sigma_{\text{VHS}}g_r)_{\max}} \overset{?}{>} R \tag{3.10}$$

with a collision occurring if $P_{\text{VHS}} > R$. Once a collision occurs, post-collision properties are calculated using conservation of momentum and energy along with a random, isotropic scattering angle. The VHS cross-section is calculated using Equation 2.5, reformulated here in terms of $\sigma = \pi d^2$, as

$$\sigma_{\text{VHS}} = \sigma_{\text{ref}}\left(\frac{g_{r,\text{ref}}}{g_r}\right)^{1-2\omega} \ , \tag{3.11}$$

with post-collision scattering angle chosen randomly on a unit sphere in the center-of-mass frame.

Collision Energy	$d\sigma/d\Omega$ **Fitting Parameters**			
	A_{MEX}	B_{MEX}	A_{CEX}	B_{CEX}
300 eV [14]	-2.02	3.24	-1.10	-1.53
1500 eV [137]	-2.50	3.51	-1.38	-1.61

Table 3.1: Fitting parameters for 300 eV and 1500 eV.

3.4.2 Anisotropic atom-ion interactions

MEX and CEX interactions between atoms and ions are governed by an anisotropic scattering model which utilizes differential cross-sections for post-collision properties. Like the VHS method, conservation of momentum and energy provide four out of the six equations required to calculate post-collision velocities. The pairing and collision algorithms also employ the NTC method described in Section 3.4.1 while the difference lies in the anisotropic nature of the post-collision scattering.

Typically, assumptions regarding the post-collision velocity direction, or scattering angle, are made to provide the remaining collision equations. In the present study, the MEX and CEX scattering angles are calculated via anisotropic scattering based on semi-empirical differential cross sections [56, 137]. As described in Section 2.2.2, this anisotropic method is based on measurements of ion-atom differential cross-sections which are then used to determine the post-collision in-plane relative velocity angles whereas out-of-plane angles are chosen randomly.

Firstly, both MEX and CEX collisions and their effects are modeled using equivalent cross-sections, as discussed in Section 2.2.2, and thus result in equal probabilities of occurring in terms of Equation 3.10 [120, 121, 15]. Atoms and ions are paired and both MEX and CEX pairs are selected to collide in an indistinguishable manner. The difference lies in the swap of charge state, representative of the transfer of the electron in the CEX collision, in the processing of post-collision properties. Figure 3.2 is recalled to once again illustrate the nature of atom-ion behaviors in the Test Cell.

The anisotropic scattering model utilizes both differential and total cross-sections

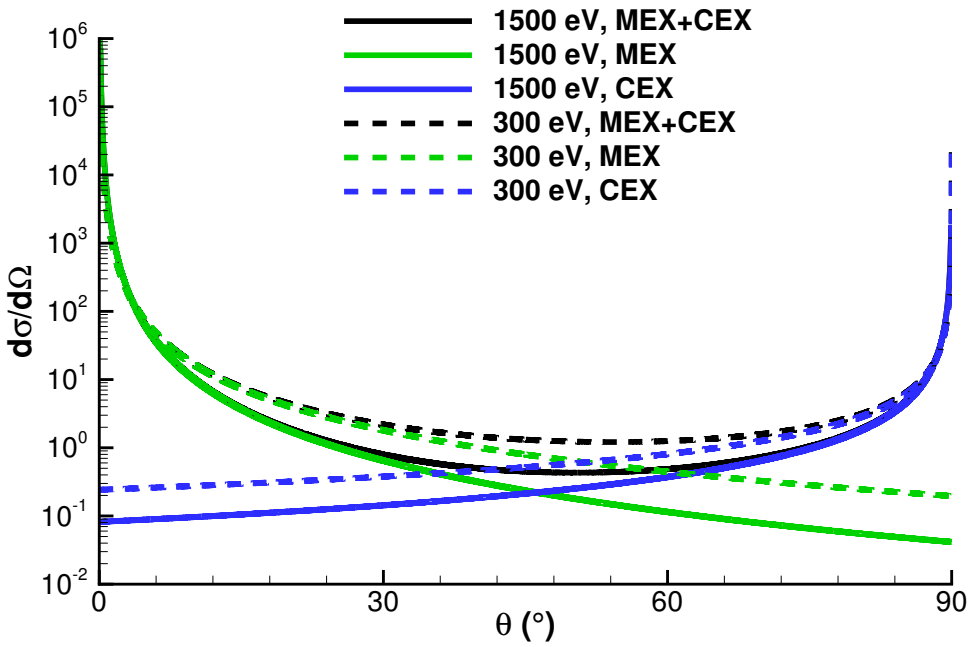

Figure 3.5: Differential cross-section curve-fits used in the MEX and CEX collision models of the current simulation (1500 eV) versus past past [14, 15] implementations (300 eV).

to allow for a more physics-based post-collision scattering behavior for heavy species. The differential cross-sections utilized are semi-empirical values, experimentally verified by Chiu et al. [53], which integrate to the value of the total cross-sections of Equations 2.7 and 2.8. Scharfe et al. [14] provide the following polynomial for calculating a curve-fit representative of differential cross-sections in the laboratory frame,

$$\frac{\mathrm{d}\sigma}{\mathrm{d}\Omega_{\mathrm{LAB}}} = \theta^{A_{\mathrm{MEX}}} 10^{B_{\mathrm{MEX}}} + (90-\theta)^{A_{\mathrm{CEX}}} 10^{B_{\mathrm{CEX}}}, \tag{3.12}$$

using values for the fitting coefficients, A_{MEX}, B_{MEX}, A_{CEX}, and B_{CEX}, found in the first row of data in Table 3.1 for 300 eV.

However, because the dominant interaction energy of this work is 1.5 keV, the differential cross-section curve-fits are re-calculated using the semi-empirical, iterative

technique of Chiu et al. and the fitting technique of Scharfe et al., resulting in the refined differential cross-sections found in Figure 3.5 which show a comparison of 300 eV and 1500 eV curve-fits. The refined 1500 eV curve-fit parameters are found in the last row of Table 3.1.

The bimodal distribution of the differential cross-sections simulate the nature of the post-collision properties in the MEX and CEX interactions: the MEX peak is representative of low-angle scattering and the CEX peak is representative of high-angle scattering. The difference in $\mathrm{d}\sigma/\mathrm{d}\Omega$ between the two implementations is slightly less than an order of magnitude but is still considered important as low-probability events are observed in the sampling of a large number of successive events.

3.5 Numerical implementation of PIE models

The reduced-order, semi-empirical models of PIE presented in Section 2.3 are implemented numerically according to the two modes of projectile impact found at the two major current-collecting electrodes: low-energy ion collection at the Inner Cylinder and high-energy atom collection at the Exit Plate. Phenomenologically, this corresponds to PE due to low-energy ions at the Inner Cylinder and KE due to high-energy atoms at the Exit Plate. High-energy ions at the Exit Plate are excluded due to their low-magnitude flux attributed to a larger collision cross-section, explained further in Section 5.1. A summary of the yield and EEDF information for these processes can be found in Table 3.2. For simplification, it is assumed that all emission from the Inner Cylinder is due to PE and all emission from the Exit Plate is due to KE; furthermore, these processes may be simulated in an independent way yet coupled to the original ion beam simulation, discussed further in Section 3.5.3.

Process	Location	Total yield	Threshold	EEDF
Potential Emission	IC	0.016	Slow Xe^+ ions	Gaussian
Kinetic Emission	EP	3×10^{-6}	$\geq$ 1.6 keV Xe atoms	non-central χ^2

Table 3.2: Summary of parameters for the PE and KE processes including their location, total yield, and their EEDF model.

3.5.1 Total yield

Total yield for both PE and KE is implemented as a flux fraction of electrons being emitted from the various surfaces, with the emitted electron current due to either PE or KE as

$$I_{e,p} = \gamma_p \, q \, \Gamma_p \, A_{IC} \tag{3.13}$$

$$I_{e,k} = \gamma_k \, q \, \Gamma_k \, A_{EP} \tag{3.14}$$

with Γ as the impacting flux of interest for the corresponding emission process and A as the surface area of the corresponding electrode surface. Implementation is focused on fluxes so that both charged and neutral fluxes can be treated in the same way, as discussed in Section 2.3.2.1.

These currents are provided by calculating the steady state flux of electrons which is emitted from one electrode and either *i*) back-stream to the same electrode, resulting in zero net current or *ii*) "cross-collect" at the other electrode, resulting in a positive net current at the emitter and a negative net current at the collector. This methodology and its results are described further in Section 5.2. Furthermore, emission is assumed to be homogeneous along the electrode surface, an assumption which is analyzed in Section 5.2.1.

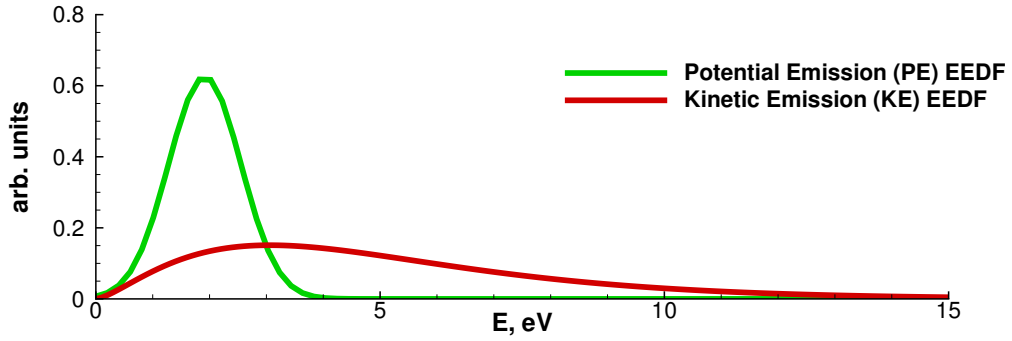

Figure 3.6: Unnormalized comparison of the probability density functions of Equations 2.18 and 2.28 describing the PE and KE EEDFs.

3.5.2 Emitted electron energy distribution function (EEDF)

Injection via a prescribed EEDF is carried out for the PE and KE processes via the acceptance-rejection method [138] in which a random injection energy is sampled and the probability of that energy compared to a random number between zero and the maximum distribution probability, P_{max}. If the random sampled energy has a probability greater than the random sampled probability, that energy is chosen. If not, a new sampled energy and random probability are chosen and the process is repeated. The EEDFs of the PE and KE processes can be seen in Figure 3.6 as prescribed by the respective probability density functions of Equations 2.18 and 2.28, described further in this section.

The PE injection is simulated following the self-convolved Gaussian distribution found in Equation 2.18. The maximum distribution probability, $P_{PE,max} = 0.625$, is used in the acceptance-rejection algorithm. The implementation of the self-convolved Gaussian, which is simply a Gaussian itself, is fairly straightforward and does not require any extra numerical algorithms.

The process of KE injection is simulated using the non-central χ^2 distribution found in Equation 2.28. Care must be taken to efficiently implement a numerical

solution of the regularized confluent hypergeometric function [139, 140], defined as the ratio of the confluent hypergeometric limit function, ${}_0F_1(;a;z)$, and the gamma function, $\Gamma(a)$, using arbitrary parameters a and z, as

$$ {}_0\tilde{F}_1(;a;z) = \frac{{}_0F_1(;a;z)}{\Gamma(a)} = \frac{\Gamma(a) z^{\frac{1-a}{2}} I_{a-1}\left(2\sqrt{z}\right)}{\Gamma(a)} \ . \tag{3.15} $$

with I_{a-1} as the modified Bessel function of order $a-1$. Substituting in terms of the distribution parameters and energy, $a = \nu/2$ and $z = \lambda E/4$, the regularized confluent hypergeometric function reduces to

$$ {}_0\tilde{F}_1(;\frac{\nu}{2};\frac{\lambda E}{4}) = \left(\frac{\lambda E}{4}\right)^{\frac{1}{2}-\frac{\nu}{4}} I_{\frac{\nu}{2}-1}\left(\sqrt{\lambda E}\right) \ . \tag{3.16} $$

The expression for the modified Bessel function, $I_{\nu/2-1}$, will result in a fractional order and can be evaluated using a standard algorithm [138]. Thus, the full expression for the KE EEDF can be written as

$$ P_k(E) = \frac{2^{-\nu/2}}{e^{\frac{(\lambda+E)}{2}}} \ E^{\frac{\nu}{4}-\frac{1}{2}} \ \left(\frac{\lambda}{4}\right)^{\frac{1}{2}-\frac{\nu}{4}} I_{\frac{\nu}{2}-1}\left(\sqrt{\lambda E}\right) \ . \tag{3.17} $$

The maximum distribution probability, $P_{KE,max} = 0.151$, is used in the previously described acceptance-rejection algorithm.

3.5.3 Supplemental electron emission details

At the initialization of a PIE simulation, the emitting electrode is chosen and the total flux of emitted electrons is derived from either the flux of low-energy ions at the Inner Cylinder for PE or the flux of high-energy, threshold-level atoms at the Exit Plate for KE. These corresponding fluxes of interest are detailed in Section 5.1. A population of numerical macroparticles is created at the surface of the electrode directly related to the emitting flux. Additionally, each macroparticle is assigned a

numerical weight which corresponds to the number of real electrons represented.

Electrons are emitted isotropically from the surface of the electrode and may collide elastically with the motionless xenon atom particles already present in the domain, described in Section 2.3.3. Additionally, resulting electron number densities from PIE are very low, of the order 10^4 to 10^6 m^{-3}, compared to ion number densities on the order of 10^{11} m^{-3} and are therefore assumed to not contribute to the source terms in Poisson's equation which is proportional to the difference of the species charge densities. Instead, the electric fields established by the ion beam and the boundary conditions of the Test Cell are used in the calculation of electrostatic forces on the electrons. These assumptions allow us to instead focus on the steady state collection fractions at each of the electrodes, described in the PIE results of Section 5.2.

The simulation is started as either a KE simulation with Exit Plate emission or a PE simulation with Inner Cylinder emission with both instances using the previously solved density and potential solutions of the ion beam simulation. It should be mentioned that instances of electron-induced SEE due to these electrons being collected at the electrodes are negligible due to the low incidence-energy electron impacts on stainless steel found in the Test Cell [141].

3.6 Summary of numerical implementation

The numerical implementation of collision and emission models results in a "coupled" method of simulating the ion beam and resulting electron emission of the Test Cell, summarized in the following operational steps:

1) Populate the Test Cell domain with Xe macroparticles until desired operating condition background pressure is met, approximately 60,000 iterations using $\Delta t = 3 \times 10^{-5}$ s.

2) Simulate 1.5 keV Xe^+ ion beam injection using $\Delta t = 3 \times 10^{-8}$ s until low-

probability collision phenomena are resolved, resulting in current collection at the Inner Cylinder and Exit Plate, approximately 600,000 iterations in total.

3) Calculate total currents on all electrodes to confirm current conservation. Additionally, calculate flux of low-energy ions on Inner Cylinder and flux of high-energy atoms on Exit Plate to determine input conditions for PE and KE, respectively.

4a) Simulate KE emission from the Exit Plate using $\Delta t = 3 \times 10^{-12}$ s and allowing electron travel in the domain to reach steady state, approximately 1,100,000 in total.

4b) Simulate PE emission from the Inner Cylinder using $\Delta t = 3 \times 10^{-12}$ s and allowing electron travel in the domain to reach steady state, approximately 1,100,000 in total.

These steps are simply continuations of the same numerical solution from MONACO-PIC; each step copies previous solution data and then a new simulation is begun with the new operating and input conditions. It can be seen that Steps 4a and 4b lie in parallel as they are independent and can be performed at the same time in order to achieve a steady state resolution of the current collection of emitted electrons at each electrode.

Chapter IV will focus on Steps 1 and 2 for heavy species collision model simulation and validation while Chapter V focuses on Steps 3, 4a, and 4b for the simulation of PIE effects on Test Cell current collection.

CHAPTER IV

Heavy Species Simulations of the Unbiased and Biased Test Cell Environment

This chapter presents the results of comparisons between experimental measurement and ion-only simulation of current collection at the various electrodes of the Test Cell. Section 4.1 presents data comparisons for the unbiased Data Set A (DSA) and DSB as well as a study of collisionless, nonelectrostatic, and isotropic assumptions about the ion beam behavior. Section 4.2 then presents data comparisons for the negatively and positively-biased Data Set C (DSC) and Data Set D (DSD) at voltages of -10 and 10 V applied to the Inner Cylinder. The effect of beam divergence is investigated in Section 4.3. Lastly, Section 4.4 provides a study characterizing important phenomena which may affect future designs of the Test Cell, such as the distribution of current along the electrodes and the collection of back-scattered, upstream ions.

4.1 Unbiased Test Cell analyses

A full comparison between simulation and the UCLA measured results for the 1.5 keV ion beam is first compiled for the unbiased data sets, DSA and DSB, in order to provide a baseline current collection comparison for the simplest cases. Both data sets DSA and DSB are used, despite being of similar unbiased conditions, in order

to portray the repeatability of the phenomena occurring within the Test Cell. In addition, the unbiased tests allow for a comparison of the Poisson equation solutions with those obtained with the Boltzmann relation wherein biased-voltage boundary conditions are of no concern. A comparison of current collection for the three electrodes and the total current is presented in Sections 4.1.1 and 4.1.2. These data sets vary slightly in the amount of total current present in the environment, the beam divergence characteristics, and the resolution of data points.

4.1.1 Unbiased current comparisons

Both DSA and DSB describe the repeatable nature of the unbiased Test Cell environment and the 1.5 keV ion beam. The unbiased Test Cell data of DSA can be seen in Figure 4.1 showing the results of current collection predictions at Test Cell electrodes Inner Cylinder (IC), Exit Plate (EP), Exit Orifice (EO), and total environment current. In these unbiased Test Cell results, the simulated Inner Cylinder current collection of Figure 4.1(a) matches well with the measurements while the computed Exit Plate current of Figure 4.1(b) consistently lies below the measured data. Figure 4.1(c) also shows the Exit Orifice and total current collection comparisons with the simulations agreeing very well with the measurements. At pressures greater than $\sim 5 \times 10^{-4}$ Torr, a major disparity can be seen in current collection comparisons at the Exit Plate. The behavior of the experimental measurements suggests that $\sim 2 - 3$ nA of extra current should be present in the system and collected at the Exit Plate. This disparity becomes a typical occurrence in the rest of the data sets as only a phenomenon such as electron emission could make up for this missing current.

The behavior of the total current is a trend seen in all predictions and experimental data sets and involves the decreasing of total current to the Test Cell as operating pressure increases and fewer ions from the beam source arrive at the Test Cell. Figure 4.1(d) shows the behavior of the total measured and simulated current

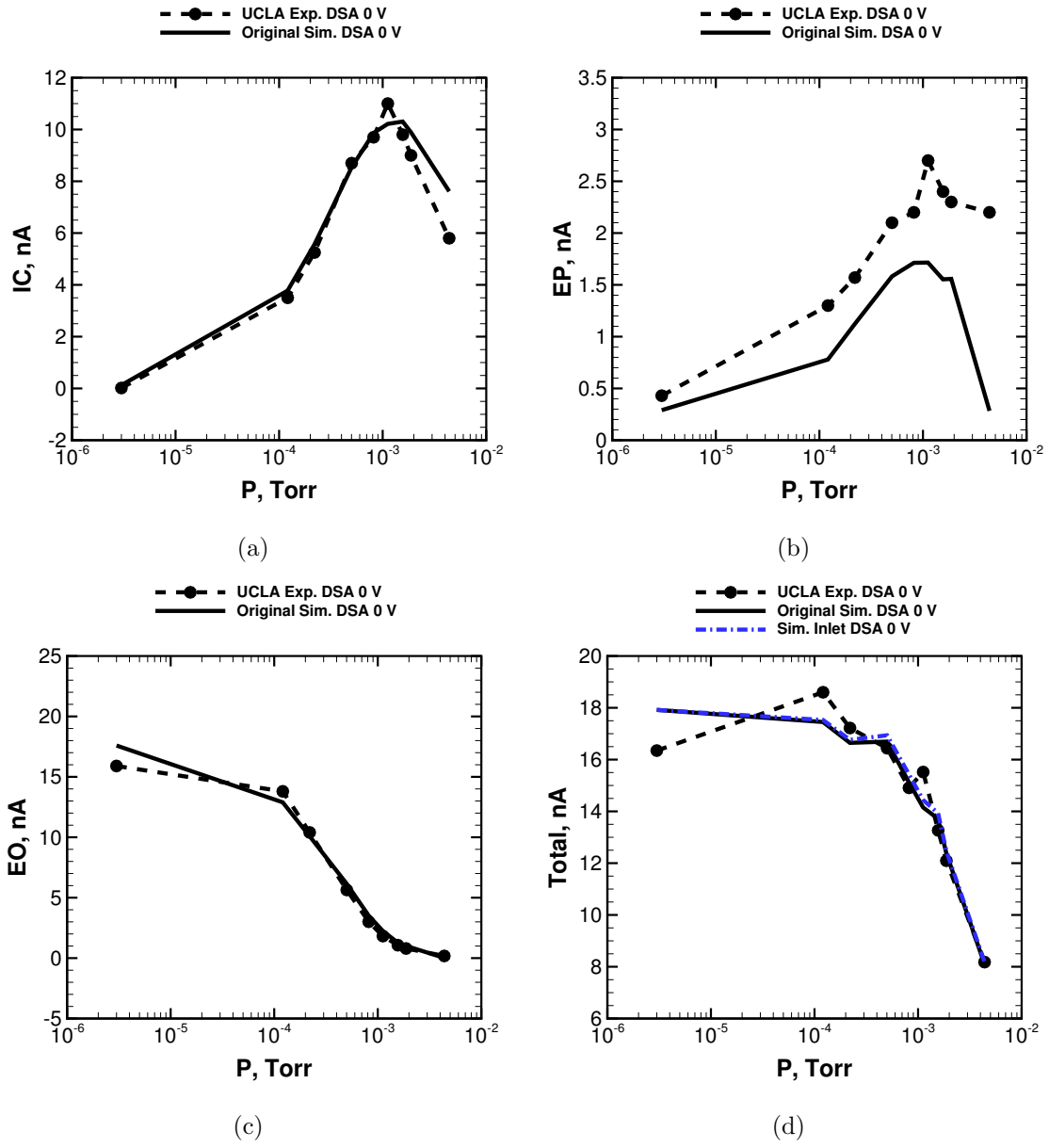

Figure 4.1: Current collection along the Inner Cylinder (a), Exit Plate (b), Exit Orifice (c) and total (d) for the unbiased DSA versus operating condition pressure from simulation and the UCLA measurements.

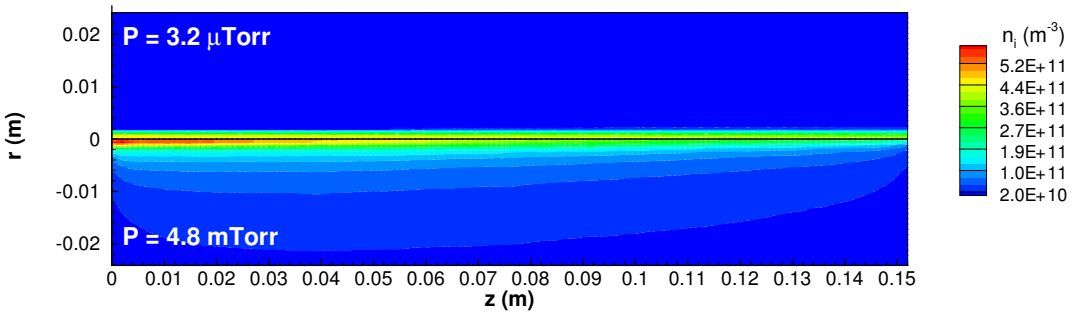

Figure 4.2: Simulated ion number density contours for the lowest and highest background pressure cases of the Test Cell for DSB.

in the simulation, defined as IC+EP+EO, compared to the inlet current defined in the simulation. Discussed in 3.2, the inlet current is defined as a curve-fit to the total (IC+EP+EO) measured current as supplied by UCLA. The total simulated current collected matches well for DSA in that total collected current matches simulated inlet current. This trend holds for the negatively-biased Test Cell cases discussed in Section 4.2 but not for the positively-biased Test Cell nor the unbiased DSB cases, discussed next.

To show the structure of the beam in the Test Cell for the unbiased case, Figure 4.2 shows simulated ion number density for the lowest and highest background pressure conditions in the Test Cell. These contours illustrate the centerline-structure of the beam as well as the attenuation and scattering behaviors as pressure increases. In the unbiased Test Cell results of DSB in Figure 4.3(a), the simulated Inner Cylinder current collection matches well with the measurements while the computed Exit Plate of Figure 4.3(b) current again consistently lies below the measured data. In the case of the Exit Plate current, there is the possibility of beam divergence which is neglected in the simulated ion beam which would lead to finite spreading of the ions and more Exit Plate current being collected than simply through scattering. For pressures ranging from 10^{-6} to 10^{-4} Torr, this could involve about 1 nA of extra current collection.

Figure 4.3(c) also shows the Exit Orifice current collection comparisons with the simulations agreeing very well with the measurements.

Again, the 10^{-3} to 10^{-2} Torr region shows a major current-collecting disparity. Unaccounted-for current makes up ∼2-3 nA of total current in the system at these operating conditions and follows a similar pattern of onset at $\sim 10^{-3}$ Torr. Additionally, Figure 4.3(d) shows a disparity in the simulated, collected total current compared to the simulated inlet current, derived from the experimental measurements as previously discussed. This disparity suggests that there is an alternate location than the IC, EP, or EO to which ions are scattered and being collected. This leads to the possibility of current collection in an upstream location, discussed later in Section 4.4.2. The magnitude of this alternate current scattering is never larger than approximately 1 nA and does not affect the overall purpose of these studies which is to compare the trends of the current collection in the Test Cell and characterize transport and emission physics. Furthermore, in certain cases such as DSA and the negative biases seen in Section 4.2 there is zero upstream current collection.

4.1.2 Collisionless, non-electrostatic, and isotropic studies

DSB is used as a comparison baseline for the two electric potential models, as noted in Figure 4.3. It can be seen that the Poisson equation results match very well with the Boltzmann relation method, displaying the efficacy of both approaches due to the lack of importance of electrostatics in this unbiased environment. The Boltzmann relation, however, is not simply making an assumption about the electric potential structure of the domain but also that there are electrons present, discussed in Section 3.3. Therefore, the Boltzmann relation is inappropriate for this environment and the reason for its ability to resolve the current collection well is hypothesized to be due to the unimportance of electrostatics in these unbiased cases, discussed in the following text.

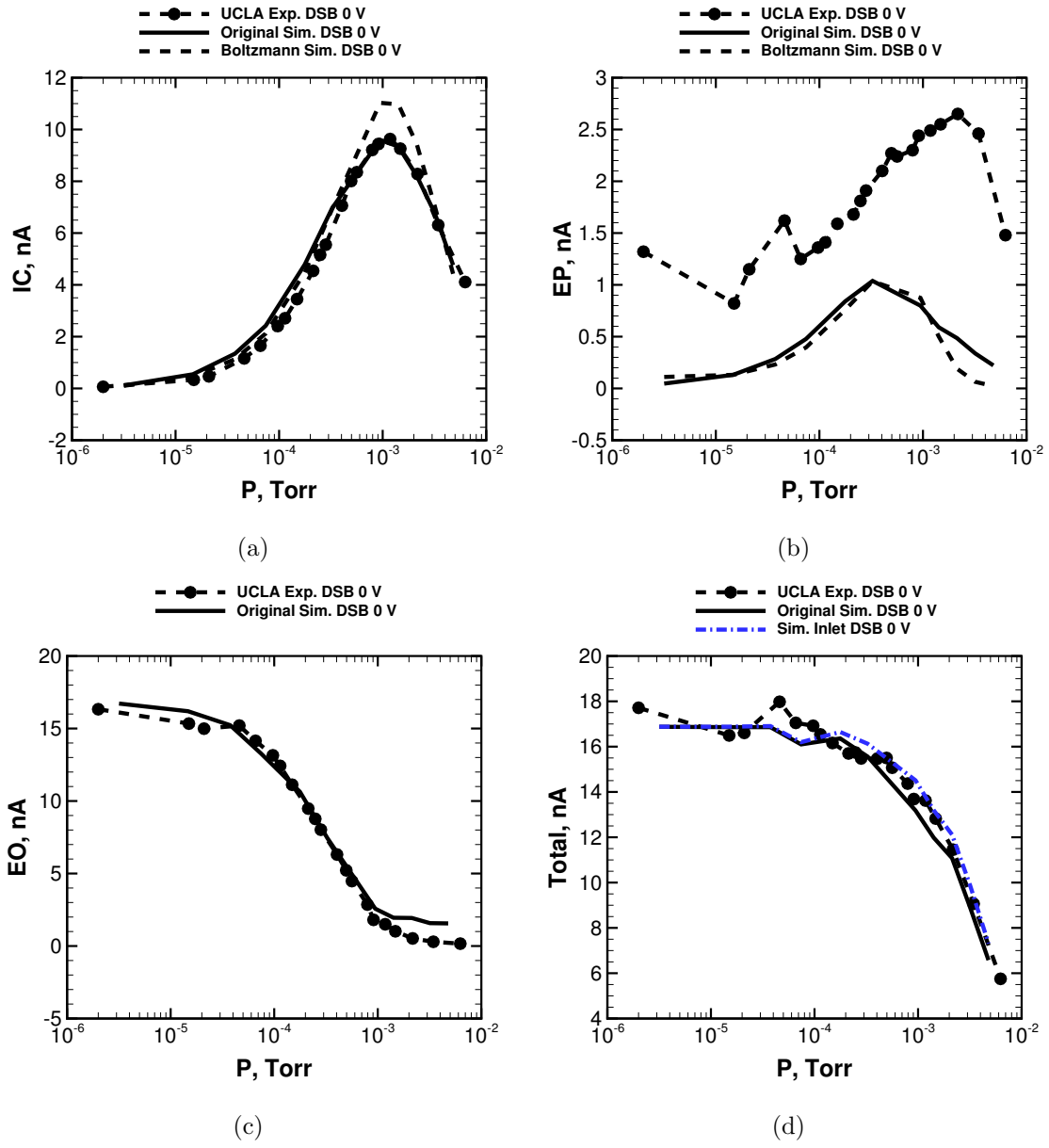

Figure 4.3: Current collection along the Inner Cylinder (a), Exit Plate (b), Exit Orifice (c) and total (d) for the unbiased DSB versus operating condition pressure from simulation and the UCLA measurements.

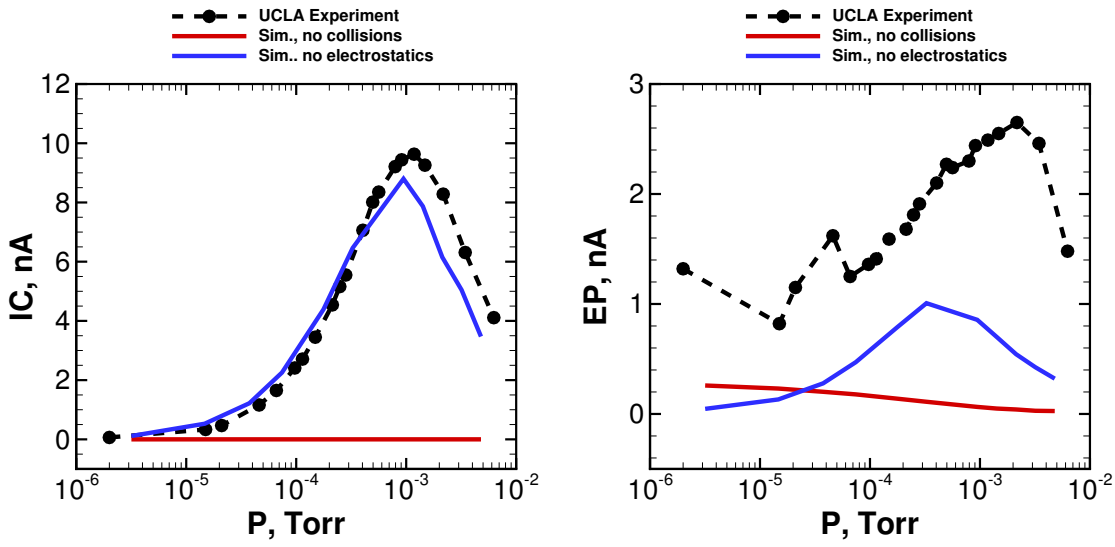

(a) (b)

Figure 4.4: Two cases of current collection along the Inner Cylinder (a) and Exit Plate (b) for the unbiased DSB versus operating condition pressure showing solutions for no collisions and no electrostatics.

In order to observe the importance of electrostatic and collision processes in the Test Cell environment, DSB is further simulated by turning off electrostatic force calculations and collision algorithms while keeping all input and boundary conditions the same. Firstly, Figures 4.4(a) and 4.4(b) show current collection at the Inner Cylinder and Exit Plate for non-electrostatic simulation of DSB. For these unbiased conditions, current collection without electrostatics matches current collection with electrostatics, proving the importance of the heavy-species collision models used and the dominance of heavy-species scattering in this environment.

Furthermore, when all collisions are ignored in the environment while electrostatics are active, there is a complete lack of agreement in current collection, also seen in Figures 4.4(a) and 4.4(b). The only exception is the slight beam divergence most likely due to electrostatic repulsion between ions within the beam and seen at the low pressure operating conditions. This divergence due to charge separation is not enough to characterize the full divergence of the experimental setup of the Test Cell,

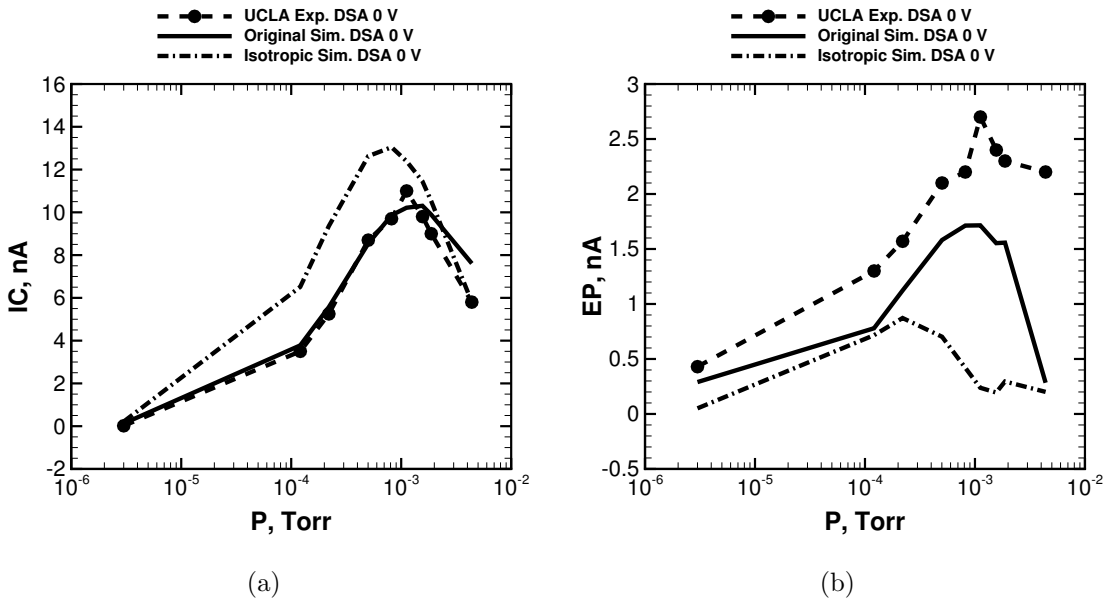

(a) (b)

Figure 4.5: Results of current collection along the Inner Cylinder (a) and Exit Plate (b) for the unbiased DSA versus operating condition pressure showing solutions for isotropic and anisotropic atom-ion collision models.

discussed further in Section 4.3.

Lastly, the atom-ion MEX/CEX collision model was numerically implemented using an isotropic post-collision scattering algorithm, similar to that of the atom-atom VHS model, instead of the anisotropic model used throughout this work. The atom-ion interaction was temporarily made isotropic in order to study the idea that not only is this environment dominated by collisions but it is also sensitive to the anisotropic nature of the atom-ion MEX/CEX interaction. Figure 4.5 shows the results of current predictions due to isotropic atom-ion collision scattering for DSA compared to the standard anisotropic model.

Figure 4.5 shows an over-prediction of ion current collected at the Inner Cylinder and an under-prediction of ion current collected at the Exit Plate due to the isotropic collision model. This behavior is representative of too great of a number of ions being scattered at all angles as opposed to the extreme high- and low-angle nature of the anisotropic model. This comparison shows how the Test Cell is effective in capturing

the correct current behavior due to the interaction's anisotropy and how a simple isotropic implementation can lead to very large disparities in all operating condition regimes of the Test Cell.

4.2 Biased Test Cell analyses

Biased Test Cell data were provided in two sets, DSC and DSD, at bias potentials of -10 and 10 V to analyze the effect of a wide range of positive and negative potentials in the Test Cell environment. The Poisson equation is required for analysis of the biased Test Cell data in order to observe the effect of the new potential boundary conditions, as described in Section 3.3. Current collection from simulation and the UCLA experimental data is presented in Sections 4.2.1 and 4.2.2. DSC data was collected at lower currents and with a smaller range of pressure operating conditions than the unbiased sets while DSD data was collected at higher currents and with a wider range of pressure operating conditions.

4.2.1 Positively-biased current comparisons

In the positively-biased current comparisons of Figures 4.7 and 4.8, interesting trends are observed which suggest strongly the presence of electrons in the environment. Firstly, Figure 4.6 displays contours of ion number density for the positively-biased simulations of DSC in order to illustrate the nature of the positively-biased environment. It can be seen that similar behavior occurs as the unbiased case, which is that of more attenuation at higher pressures. However, rather than scattered, slow ions spreading through the domain at higher pressures, the beam is more focused throughout the Test Cell, indicative of the electrostatic repulsion of the positively-biased Inner Cylinder.

Simulated Inner Cylinder current collection, shown in Figures 4.7(a) and 4.8(a), show good correlation for the lower-pressure region and then lie above the measure-

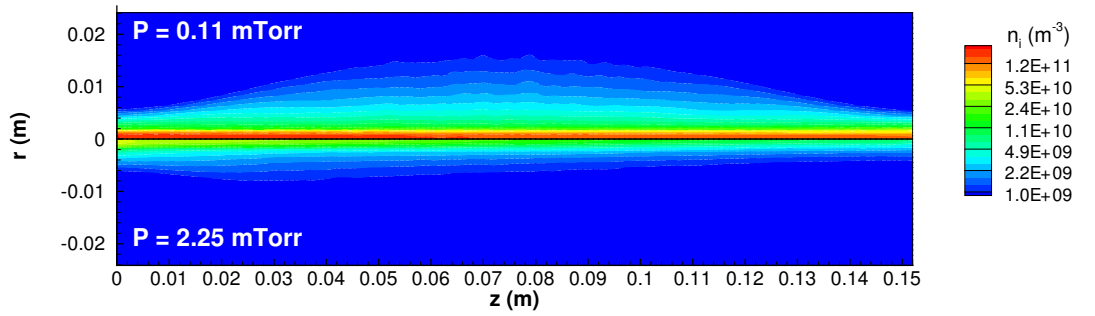

Figure 4.6: Simulated ion number density contours for the lowest and highest background pressure conditions of the Test Cell for the positively-biased case of DSC.

ments for the higher-pressure region. Moreover, this higher-pressure region shows negative current collection at the Inner Cylinder which is impossible for an ion-only simulation with only positive charge-carriers.

Additionally, much like in the unbiased data sets, pressures greater than $\sim 10^{-3}$ Torr are poorly resolved at the Exit Plate in that they severely underestimate the amount of current collection at most pressure conditions, seen in Figures 4.7(b) and 4.8(b). The trend for the experimental current collection measurements at the Exit Plate to go more positive in the higher-pressure region corresponds to the dip in Inner Cylinder current which goes negative. The disparity at the lower-pressure region, however, should not be ignored as there is indication that there may be unresolved beam divergence in the simulated ion beam resulting in off-axis ions being collected at the Exit Plate in the measurements, providing approximately 0.4 nA of additional collected current for DSC and 1.5 nA for DSD.

Figures 4.7(c) and 4.8(c) show the behaviors of the measured and simulated current at the Exit Orifice and Figures 4.7(d) and 4.8(d) show the total current for DSC and DSD, respectively. Similar to the unbiased case, there is a small disparity in the simulated, collected total current compared to the simulated inlet current. Phenomenologically, the possibility of current collection in an upstream location, dis-

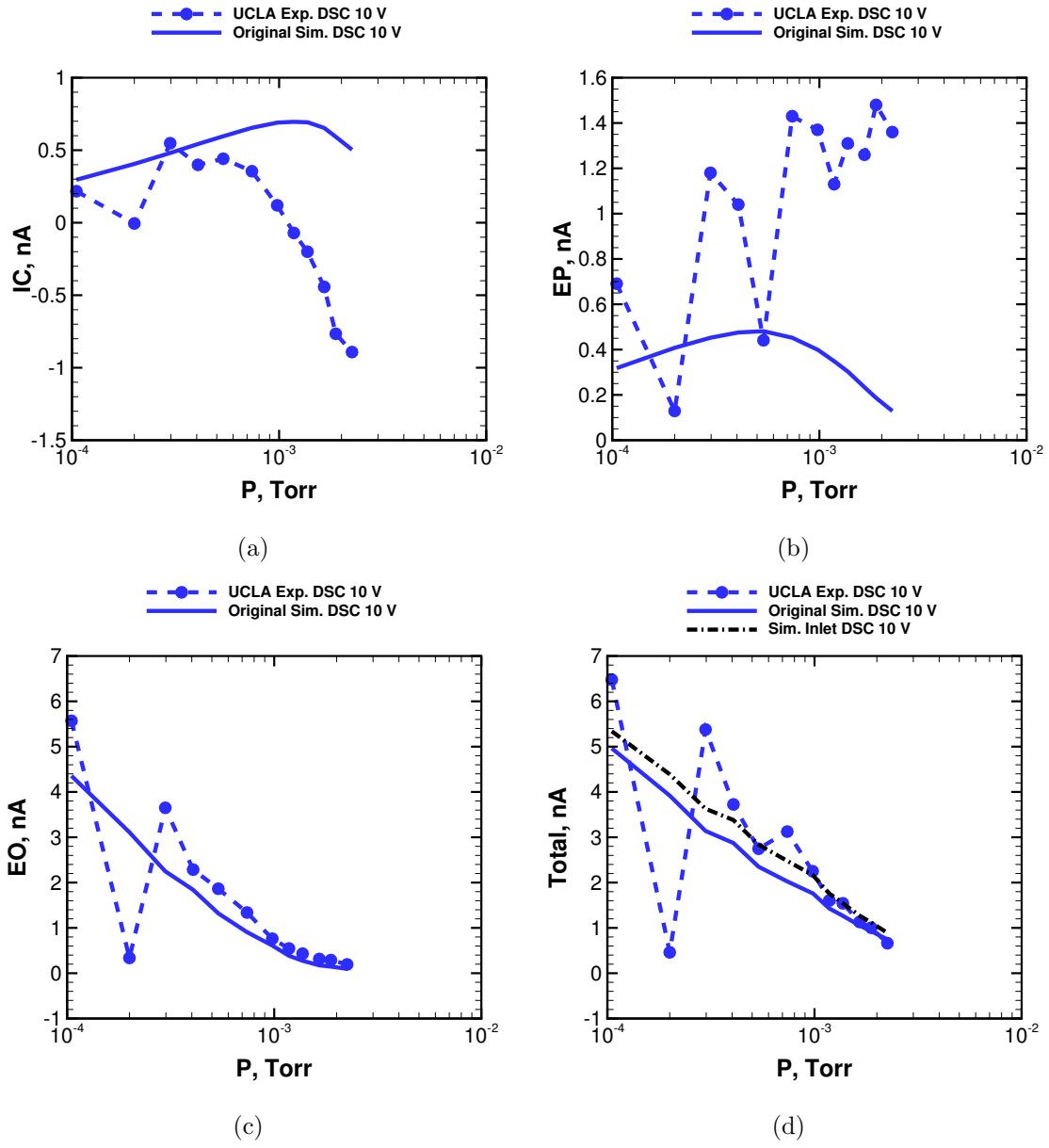

Figure 4.7: Current collection along the Inner Cylinder (a), Exit Plate (b), Exit Orifice (c), and total (d) for the positively-biased data of DSC versus operating condition pressure from simulation and the UCLA measurements.

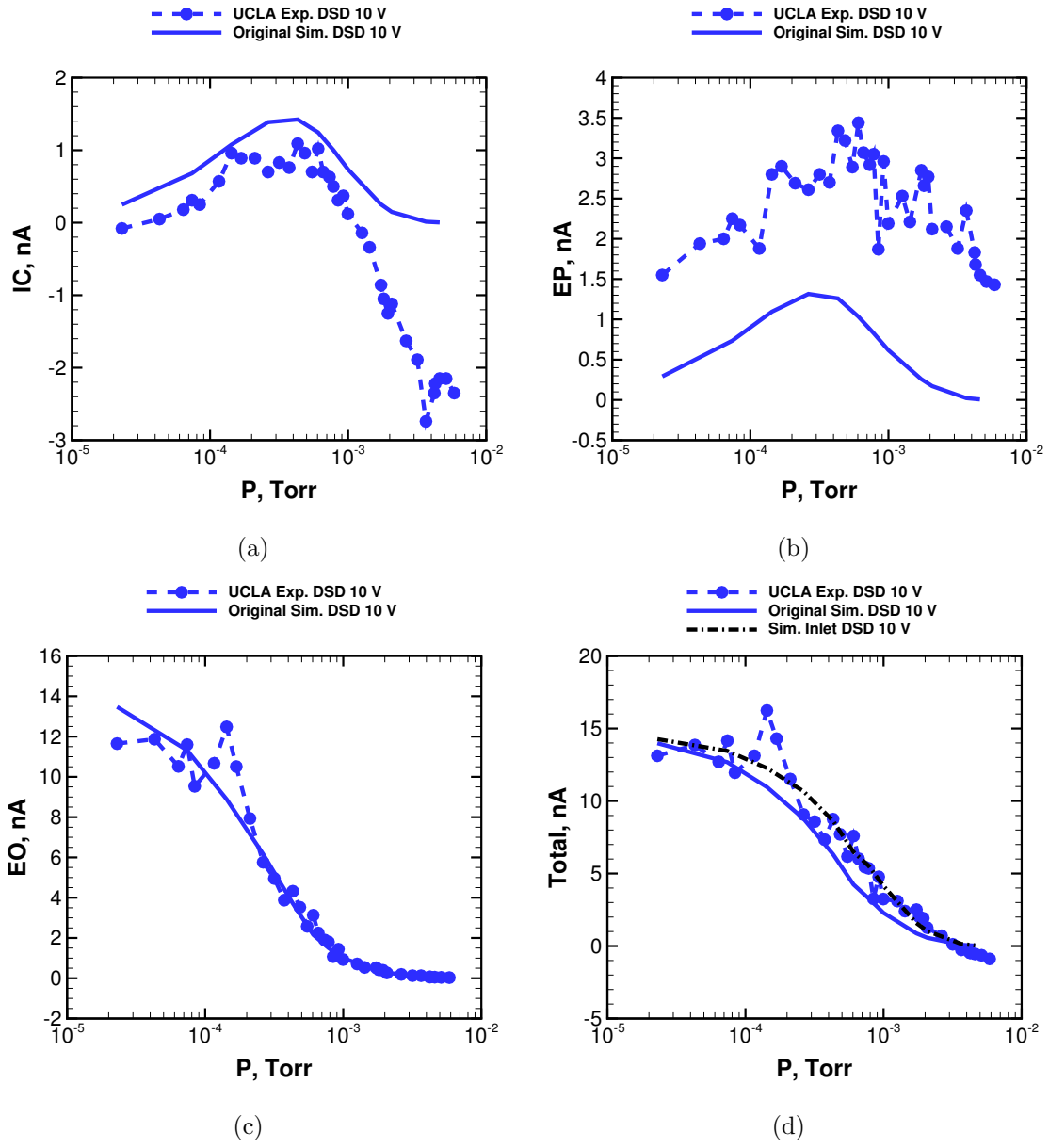

Figure 4.8: Current collection along the Inner Cylinder (a), Exit Plate (b), Exit Orifice (c), and total (d) for the positively-biased data of DSD versus operating condition pressure from simulation and the UCLA measurements.

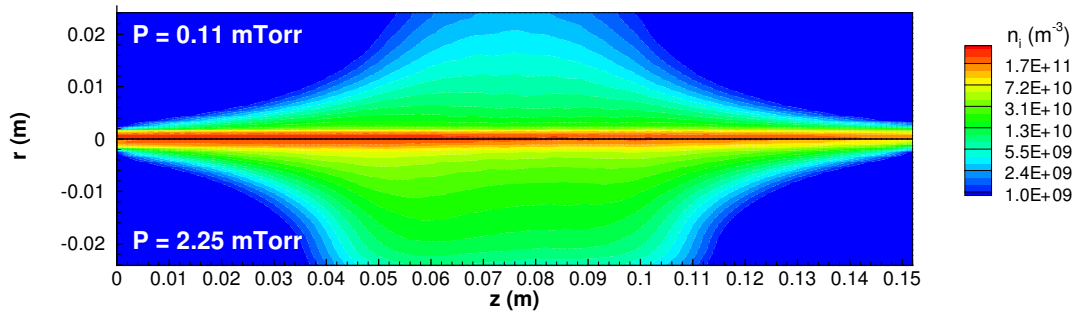

Figure 4.9: Simulated ion number density contours for the lowest and highest background pressure conditions of the Test Cell for the negatively-biased case of DSC.

cussed later in Section 4.4.2, is very likely as low-energy, charged particles created due to CEX at the upstream location of the Test Cell will be repelled from the Inner Cylinder and diverted upstream.

4.2.2 Negatively-biased current comparisons

In the negatively-biased current comparisons of Figures 4.10 and 4.11, more trends are observed which suggest strongly the presence of electrons in the environment. Firstly, Figure 4.9 displays contours of ion number density for the negatively-biased simulations of DSC in order to illustrate the nature of the ion beam. The electrostatic attraction of the ions at the negatively-biased Inner Cylinder is easily visible as more scattered, low-energy ions are attracted to the negative Inner Cylinder as pressure increases. Figures 4.10(a) and 4.11(a) show how the simulated Inner Cylinder current collection matches well for the lower-pressure region but tends to under-predict the current at the higher-pressures. However, the simulated Exit Plate current collection of Figures 4.10(b) and 4.11(b) again lies mostly below the measurements. Looking at the Exit Plate for beam divergence, it can be seen that the experimental measurements of DSC show much less beam divergence than that of DSD which shows approximately 1 nA of current due to off-axis ions.

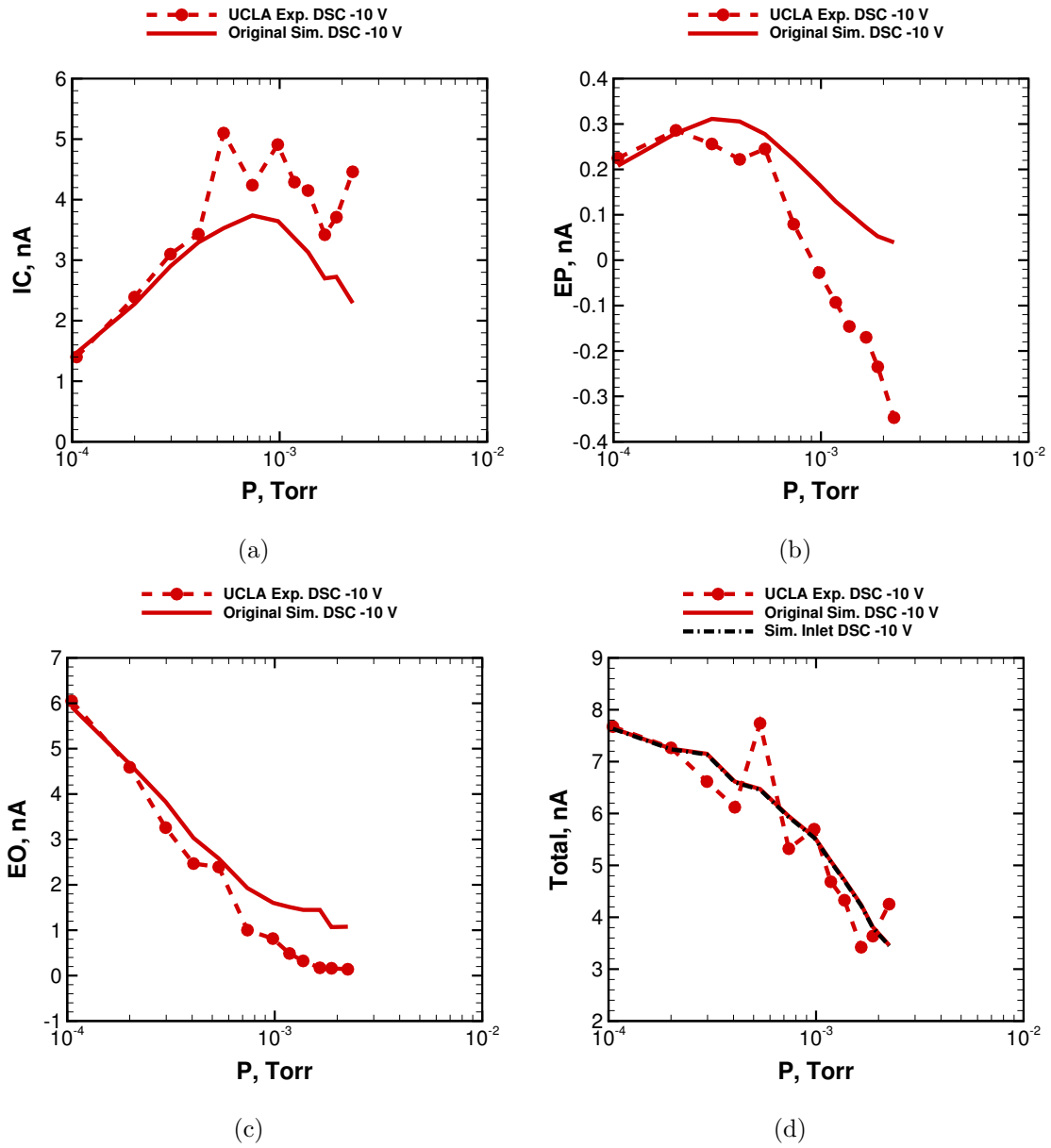

Figure 4.10: Current collection along the Inner Cylinder (a), Exit Plate (b), Exit Orifice (c), and total (d)for the negatively-biased data of DSC versus operating condition pressure from simulation and the UCLA measurements.

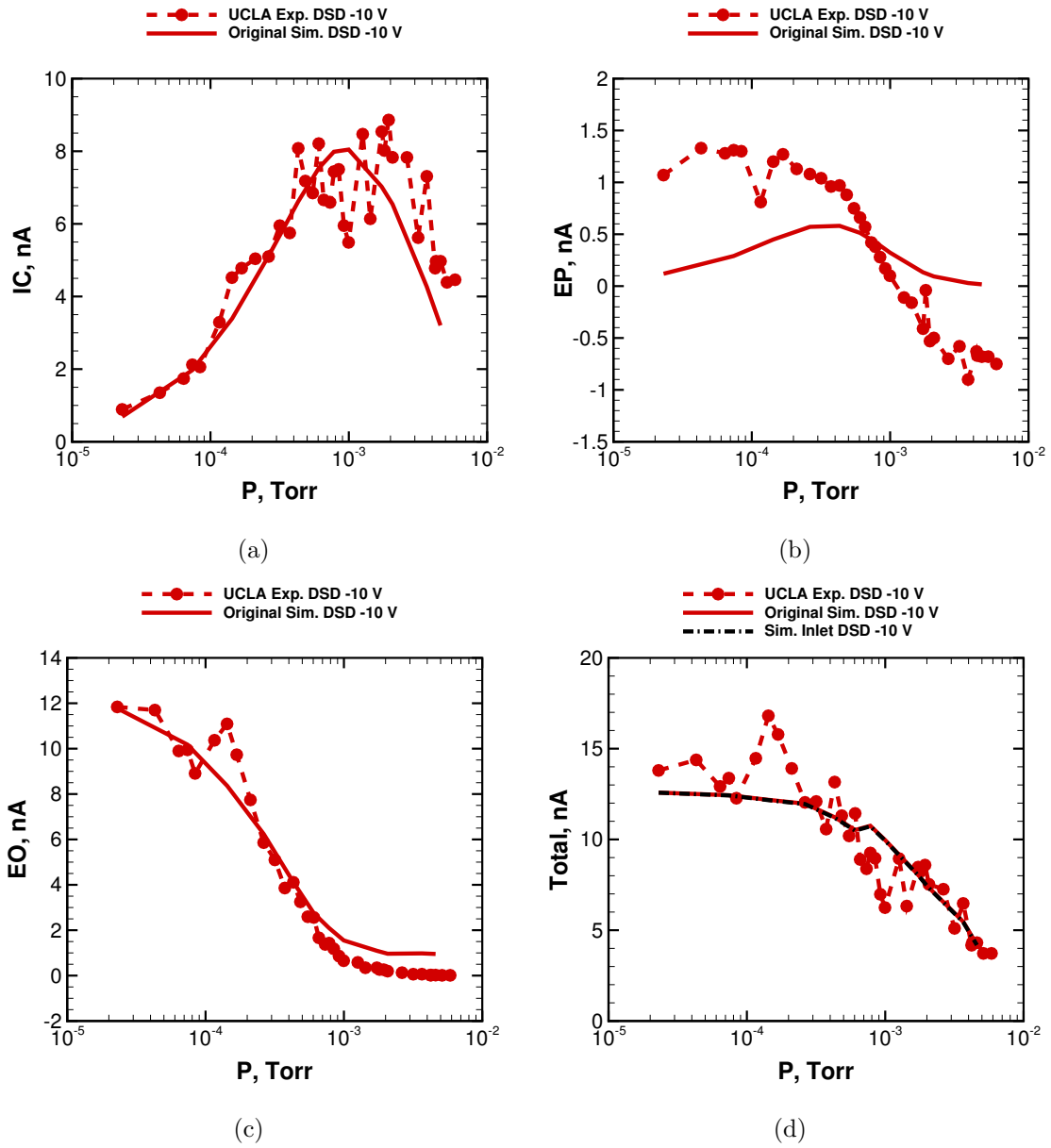

Figure 4.11: Current collection along the Inner Cylinder (a), Exit Plate (b), Exit Orifice (c), and total (d) for the negatively-biased data of DSD versus operating condition pressure from simulation and the UCLA measurements.

The simulated Exit Plate collection further reinforces the suggestion that ion-only simulation is not capturing all of the physics occurring in the biased experimental data. Experimental measurements show negative current collection at the Exit Plate and larger currents at the Inner Cylinder than simulated which, much like the phenomenological description used in the positively-biased results, can be explained with electron physics as electron emission from the Inner Cylinder being collected at the Exit Plate.

Figures 4.10(c) and 4.11(c) display the reasonably good trends of the Exit Orifice despite a slight over-prediction of approximately 1 nA at higher-pressures. Additionally, Figures 4.10(d) and 4.11(d) display the total currents of DSC and DSD which, unlike the positively-biased environments, shows a perfect match between injected and collected current at the Inner Cylinder, Exit Plate, and Exit Orifice for simulation and experiment. This means that zero current is being collected at any other electrode within the Test Cell. This behavior is most likely due to the negative bias acting as an ion-collector and causing any possibly backscattered ions to instead divert to the Inner Cylinder.

4.2.3 Current collection as a function of ion energy

An important byproduct of the collision environment is the population of low-energy ions created from CEX interactions which produce high-angle scattering. Figure 4.12 shows the energy distribution of current collection along the Inner Cylinder for the -10 and 10 V biased cases of one operating condition of DSD. Using 0.15 eV bins, it can be seen that the majority of ions reaching the Inner Cylinder are, in fact, at a low energy of approximately 0.073 eV, or a velocity of 320 m/s, corresponding to the approximate thermal energy of the background atom species.

In addition, a small peak at the energy of 10 eV for the -10 V biased case corresponds to the electrostatic acceleration of ions toward the Inner Cylinder. However,

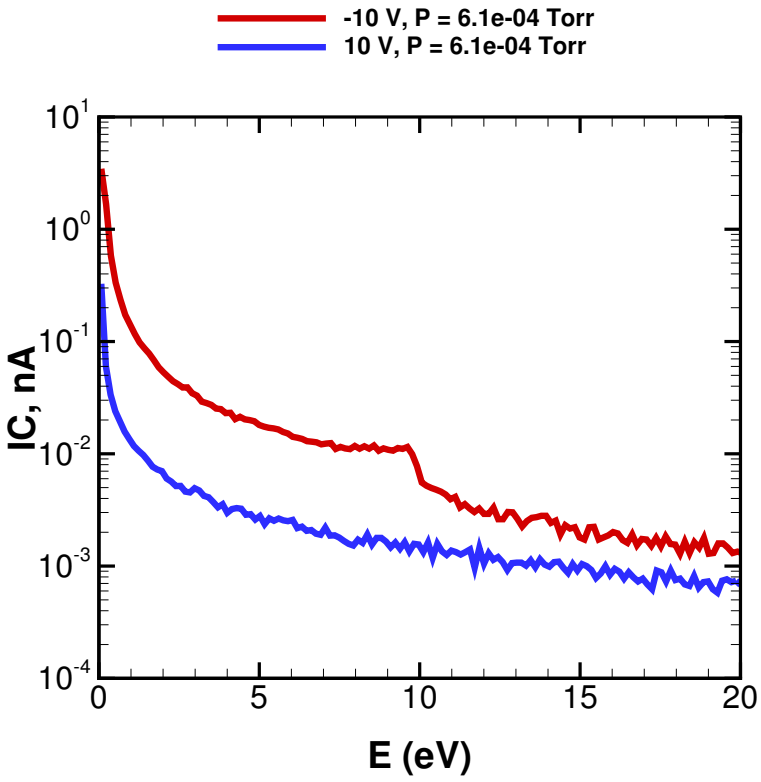

Figure 4.12: Energy distribution of current collected along the Inner Cylinder for the biased DSD at one operating condition pressure for the -10 and 10 V cases.

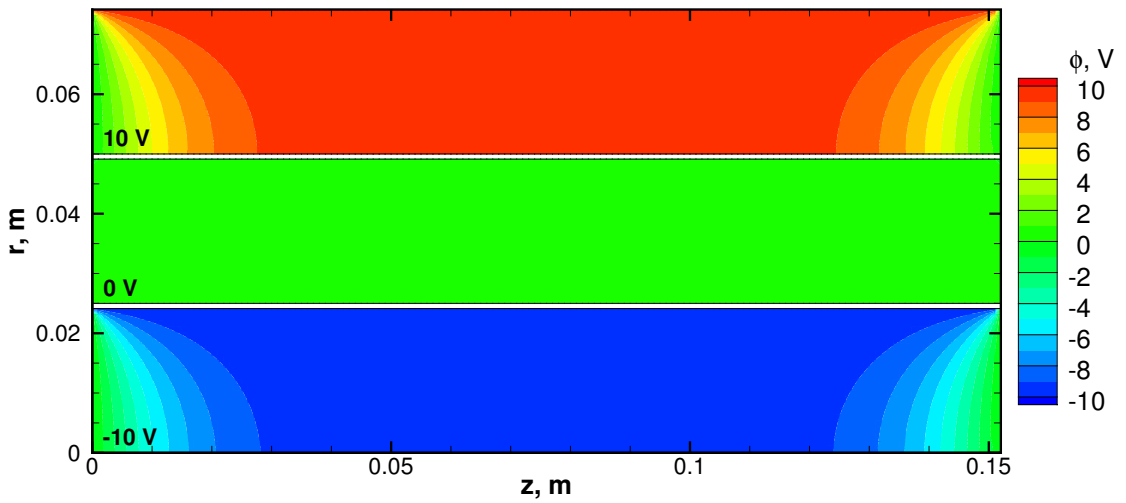

Figure 4.13: Comparison of potential contours for the -10 and 10 V cases as compared to an unbiased case of the Test Cell environment.

this peak is small in comparison to the low-energy ion peak because of the electric potential structure which develops in the Test Cell during biasing, seen in Figure 4.13. It can be seen that there are only small regions in the upstream and downstream locations of the Test Cell in which a low-energy ion would accelerate through 10 V of electric potential before impacting the Inner Cylinder.

4.3 Analysis of beam divergence

An important aspect of the facility tests that needs to be considered carefully is the current collected at the Exit Plate due to divergence of the ion beam. Ideally, the experiment would have no divergence so that all current collection was due to ions scattering from a perfectly collimated beam. However, due to electrostatic repulsion and ion-optics imperfections, a small but finite level of experimental beam divergence is to be expected. A series of numerical simulations is therefore conducted for three of the data sets which show signs of divergence to assess any sensitivity on the computed

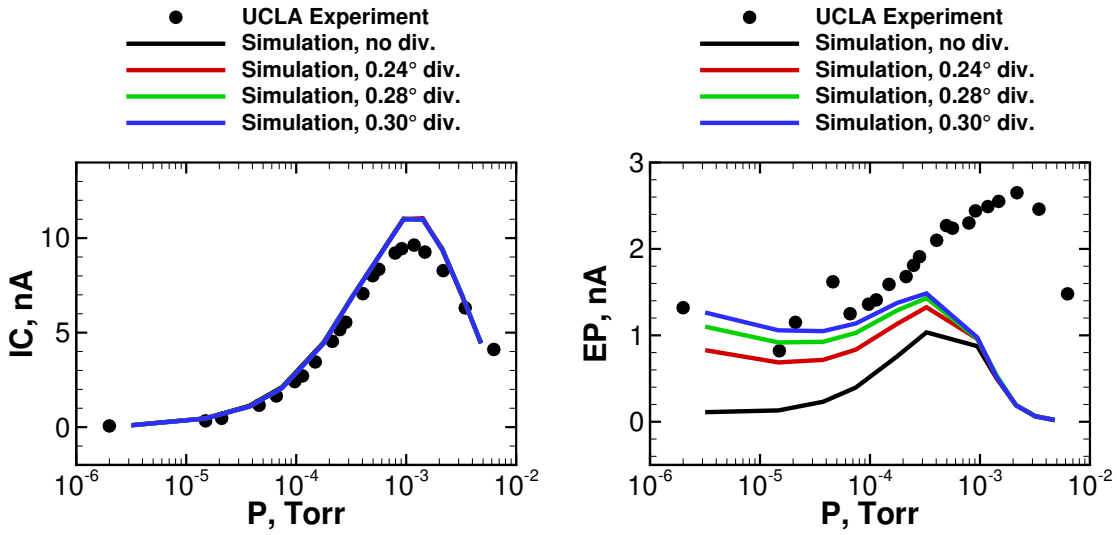

(a) (b)

Figure 4.14: Current collection along the Inner Cylinder (a) and Exit Plate (b) for the unbiased DSB versus operating condition pressure illustrating simulation sensitivity to beam divergence.

results.

Figure 4.14 shows results of varying the beam divergence of the ion beam to angles of 0.22°, 0.26°, and 0.30° for the unbiased case DSB. This set of beam divergences shows almost no change in Inner Cylinder current collection and increases in Exit Plate current collection in the lower-pressure regime. Comparison of the simulations and experimental measurements suggest that the experimental beam divergence for the DSB experimental conditions is approximately 0.30°, the closest matching curve. However, the variation of beam divergence has negligible effect on the higher-pressure current collection at the Exit Plate as all current collection collapses on a single profile.

Ion beam divergence is also analyzed for 0 V cases of the biased data sets, DSC and DSD, seen in Figures 4.15 and 4.16. Divergence is initially set at 0.30° because of assumed consistency of the ion beam. It can be seen in Figure 4.15 that the beam divergence of DSC is, in fact, the same as that of DSB, 0.30°. Figure 4.16 shows the corresponding beam divergence results for DSD which lie closer to 0.4°.

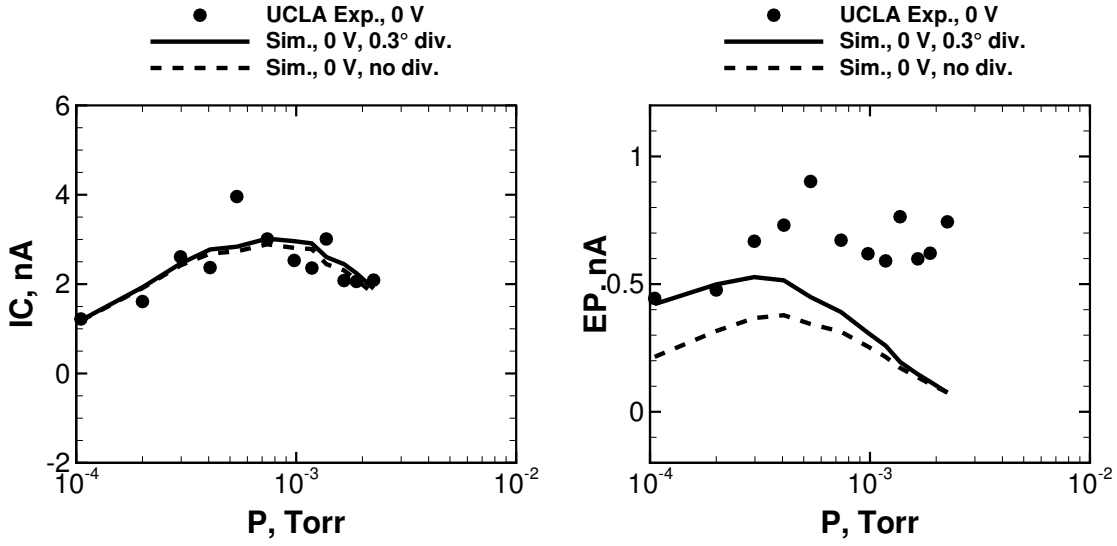

(a) (b)

Figure 4.15: Current collection along the Inner Cylinder (a) and Exit Plate (b) for the biased DSC versus operating condition pressure illustrating simulation sensitivity to beam divergence.

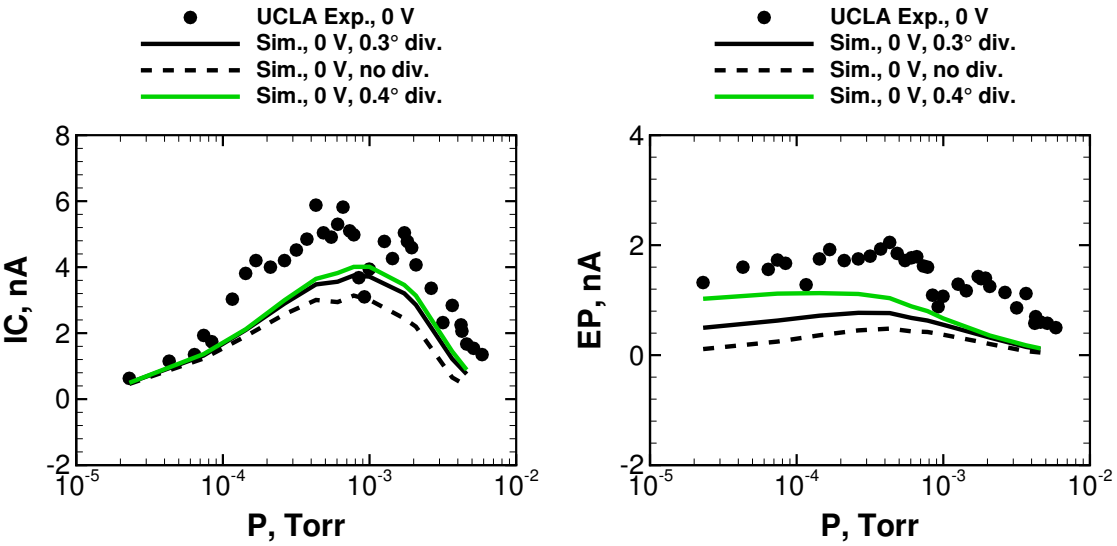

(a) (b)

Figure 4.16: Current collection along the Inner Cylinder (a) and Exit Plate (b) for the biased DSD versus operating condition pressure illustrating simulation sensitivity to beam divergence.

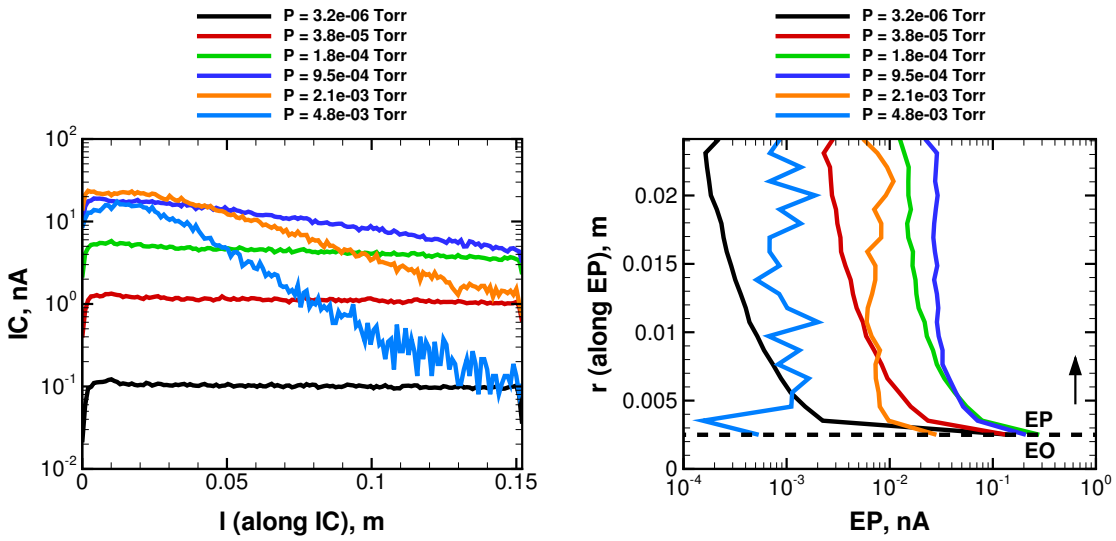

(a) (b)

Figure 4.17: Spatially resolved current collection along the Inner Cylinder (a) and Exit Plate (b) for various operating conditions of the unbiased DSB.

The reason for the disparity in DSDs beam divergence is likely due to the variability of the beam conditions between the different data sets. Additional measurements are being implemented to better characterize the beam divergence in future experiments [37]. These results portray a reasonably consistent beam divergence in the experimental measurements.

4.4 Numerical analysis for Test Cell design

In addition to sharing current collection measurements, close collaboration with the experimental team at UCLA also allows for iterative experimental design and modification based on numerical prediction of capabilities which are not yet implemented but may improve the characterization of the environment within the Test Cell. Specifically, there are two modifications of interest to the experiment: *i*) spatial resolution of electrode current collection, and *ii*) collection of upstream-plane current.

4.4.1 Electrode segmentation for spatial resolution of current

The first possible modification involves the segmentation of electrodes to allow spatial resolution of the experimental measurements. The spatial prediction of current collection along the Inner Cylinder and Exit Plate could lead to a suggested segmentation pattern of these electrodes. Segmentation of the Exit Plate could lead to the separation of un-collided beam divergence current from glancing-collision (MEX) current. Furthermore, segmentation of the Inner Cylinder could lead to better resolution at possible electron-collection locations near the upstream or downstream regions of the Test Cell.

Spatially resolved numerical results of Exit Plate and Inner Cylinder current collection can be seen in Figure 4.17. For the Inner Cylinder, these results suggest a generally homogeneous current collection at low pressures and a concentration at upstream locations for higher pressures. This suggests that scattering collisions become more concentrated toward the upstream location of the Test Cell as operating pressure increases. Furthermore, for the Exit Plate, most current collection occurs in the inner 2 mm of the electrode, probably due to the presence of beam divergence and low-angle collisions. Exit Plate current collection quickly drops off radially but a certain threshold could be suggested for glancing, low-angle MEX ions.

4.4.2 Addition of an Upstream Plate (UP)

The second modification involves the addition of a current collector which lies in the upstream plane of the beam injection. The experiment was originally designed for low Test Cell pressures where upstream current would be small. However, due to the interest in relatively higher operating pressures, efforts are underway to install an Upstream Plate (UP). This electrode will collect ion current due to backscattering collisions as well as electron current due to secondary emission at the near-inlet end of the Inner Cylinder. As seen in Sections 4.1 and 4.2 for DSB, as well as all of the

positively-biased data sets, the collection of upstream-scattered ions is essential to the full characterization of the Test Cell.

Figure 4.18 shows the numerical predictions of UP current due to backscattered ions for all data sets. It can be seen that the UP current is trivial for the unbiased DSA and the negatively-biased environments, as previously discussed. The unbiased DSB and positively-biased environments, however, show a scattering behavior which leads to approximately 1 nA of current being collected upstream at pressure conditions nearing 10^{-3} Torr.

This current collection is not at a magnitude which negatively affects the goal of this work which is to validate the trends of the current collection at the Test Cell electrodes. The total current collected at the IC+EP+EO is enough to validate the heavy species collision models used in this chapter as well as the electron physics introduced in the next.

4.5 Summary of unbiased and biased Test Cell current collection results

Good agreement is shown between the simulations, based on the transport models of Section 2.2.2, and the experimental measurements taken at the electrodes of the Test Cell. It was shown in Section 4.1 that the nature of the scattering and subsequent current collection is a collision-dominated process in the case of the unbiased Test Cell. Section 4.2 then provided results which suggest the presence of electrons in the experiments, an aspect not captured by these ion-only simulations. In the measured results, electrons appear to be present in two ways:

1. Both unbiased and biased current comparisons show an underestimated amount of current at the Exit Plate, suggesting that electron emission could lead to observed positive current collection at that electrode.

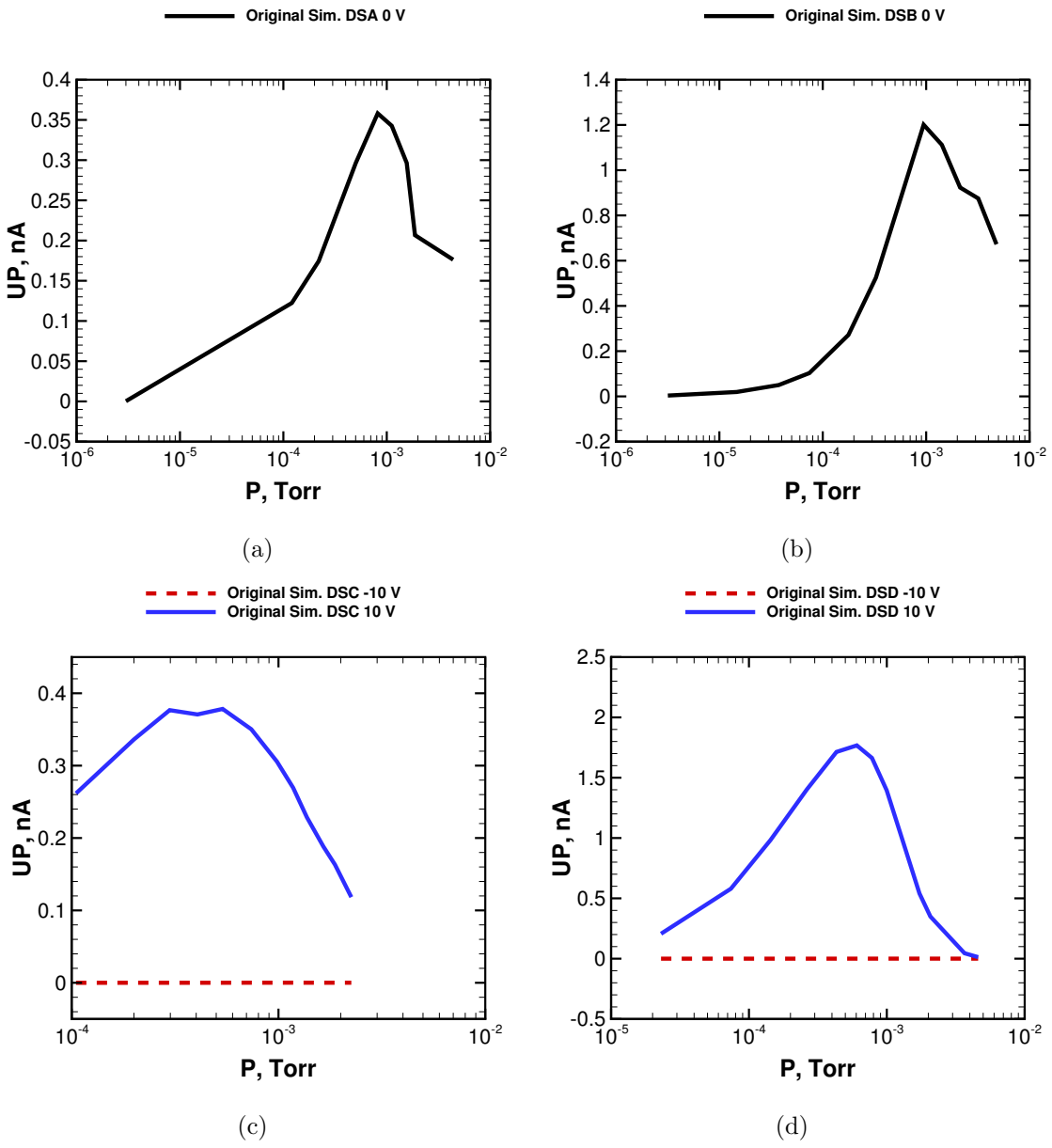

Figure 4.18: Current collection at the UP for data sets A (a), B (b), C (c) and D (d) versus operating condition pressure from simulation.

2. Positively-biased Test Cell current comparisons show instances of negative current collection at the Inner Cylinder which becomes a collector of secondary electrons created at the Exit Plate due to electrostatic attraction.

3. Negatively-biased Test Cell current comparisons show instances of negative current collection at the Exit Plate due to secondary electrons created at the Inner Cylinder.

In Chapter V, efforts are made to include electron physics in a manner which is *i*) computationally effective by relying on a reduced-order, uncoupled simulation process and *ii*) semi-empirical in that a mixture of known and unknown environmental and material parameters must be used.

CHAPTER V

Simulation of Particle-Induced Electron Emission in the Test Cell

It is established in Chapter IV that there are transport phenomena which are not being captured in the ion-only simulations of the Test Cell. These phenomena are suggested to be related to electron physics due to the presence of negative current collection in the UCLA experiments.

In this chapter, simulation results are presented which describe how the flux of heavy species at the electrodes of the Test Cell affects the behavior of emitted electrons from these electrodes. The current collection due to particle-surface interactions presented in this section are driven by the flux of threshold-level xenon atoms at the Exit Plate and the flux of low-energy xenon ions at the Inner Cylinder as these interactions represent the dominant KE and PE sources of secondary electrons within the Test Cell.

Section 5.1 describes an analysis of the heavy species wall flux of populations of interest, with emphasis placed on Exit Plate high-energy atoms and Inner Cylinder low-energy ions. Section 5.2 describes the electron simulations, paying attention to a quantification of backstreaming and cross-collected electron populations at the electrodes. Section 5.3 then provides results of current collection in the Test Cell taking into account the effects of the PIE models while Section 5.4 describes a sensitivity

analysis on the yields of the KE and PE models.

5.1 Heavy species wall flux

This section describes the fluxes of the xenon populations of interest at the walls of the Test Cell. These fluxes directly determine the fluxes of electrons from the emitting electrodes and are essential in considering the dominant mode of emission in the various environments (either PE or KE).

5.1.1 Unbiased Test Cell

The wall fluxes of interest to PIE versus particle energy for the unbiased Test Cell environment are presented in Figure 5.1 for unbiased operation of the Test Cell for low-, medium-, and high-pressure operating conditions showing the threshold-velocity atom flux of interest in Figure 5.1(a) and the low-energy ion flux of interest in Figure 5.1(b).

In Figure 5.1(a), the high flux of atoms at the Exit Plate can be observed following a trend related to the heavy-species collision model showing a low-energy peak, representative of atoms undergoing either low-angle MEX collisions with ions or low-energy VHS-type collisions with other atoms, and a high-energy peak, representative of atoms which were previously ions and underwent a CEX collision. It is the high energy region of this wall flux chart which is the region of interest for KE processes at the wall with high-energy (threshold) fluxes reaching values of approximately 10^{18} $m^{-2}s^{-1}$. Discussed previously in Section 2.3.2.1, the high-energy atom flux is chosen because, by comparison, the flux of high-energy ions reaching the EP is on the order of 10^{6} $m^{-2}s^{-1}$ less in magnitude.

Described previously, the threshold energy of interest for high-energy atoms at the surface is assumed to be 1.6 keV for this system. Despite the average ion beam injection energy being 1.5 keV, the following results show the presence of 1.6 keV

particles, as mentioned in Chapter II. The presence of particles with energies in excess of 1.5 keV is a result of the magnitude of high axial and radial velocities which can occur due to the anisotropic nature of the collisions. Figure 5.1(a) shows a flux of atoms with an energy greater than 1.5 keV that is approximately 10^6 smaller than the peak low-energy fluxes for each operating condition. This small population is directly related to the anisotropic, differential, atom-ion cross-section curve fits illustrated in Figure 3.5 in which large-angle scattering events have a probability near 10^{-6} of occurring post-collision. An example of a low-probability event in the case of these anisotropic collisions would be a MEX collision resulting in a high-angle, high-energy ion as opposed to the typical glancing, high-energy ion. This results in a small population of high-energy particles travelling radially and interacting with a larger population of high-energy particles travelling axially, thus resulting in a very small population of particles which have both high-energy radial and axial velocity components. It is this small population of highest-magnitude energy particles which are important in the characterization of KE processes in an environment such as this.

In Figure 5.1(b), the flux of ions to the Inner Cylinder shows similar trends with a less pronounced high-energy peak. In fact, at high pressures, the high-energy peak completely disappears as the ions which reach the Inner Cylinder have been mostly equilibrated. The low-energy peak found in Figure 5.1(b) is important because it represents the majority of the flux at the Inner Cylinder by low-energy ions and the flux which is used in the PE process for electron emission from the Inner Cylinder.

Specific fluxes of interest versus operating condition pressure are shown more concisely in Figure 5.2, showing atom threshold flux at the Exit Plate and low-energy ion peaks at the Inner Cylinder. These fluxes determine the PIE flux from the electrodes of the Test Cell using the yield-flux relationship found in Equations 3.13 and 3.14.

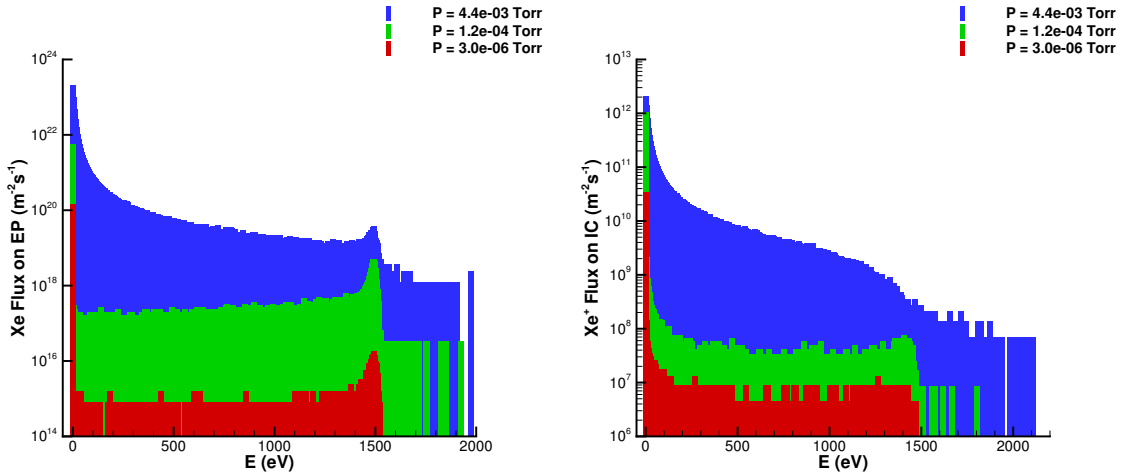

(a) (b)

Figure 5.1: Wall flux distributions of particle energy for the unbiased configuration: (a) Xe on the Exit Plate (EP); (b) Xe^{+} on the Inner Cylinder (IC).

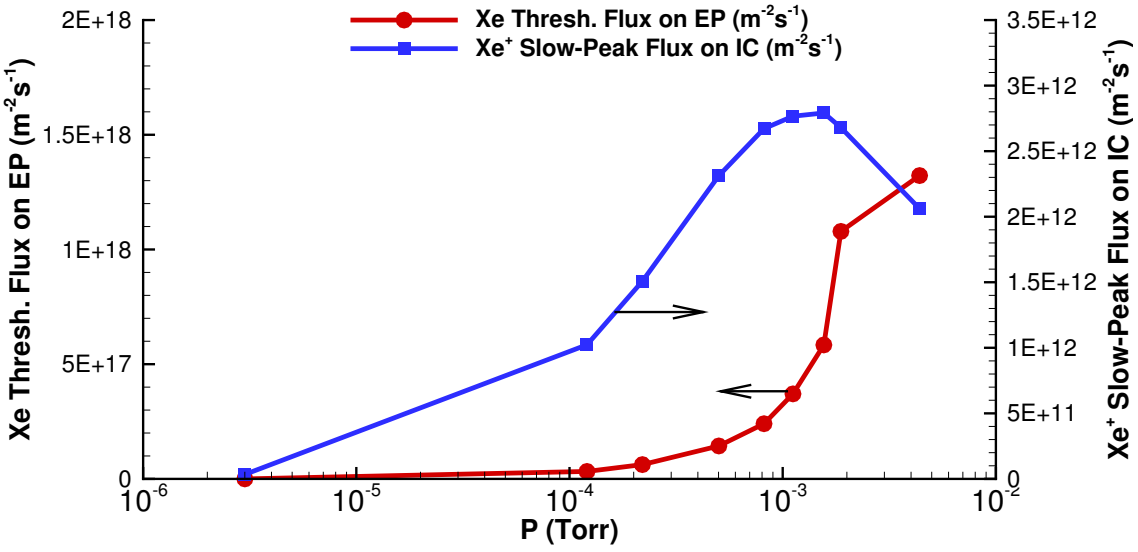

Figure 5.2: Wall flux peak fluxes of interest versus operating condition pressure for the unbiased Test Cell environment.

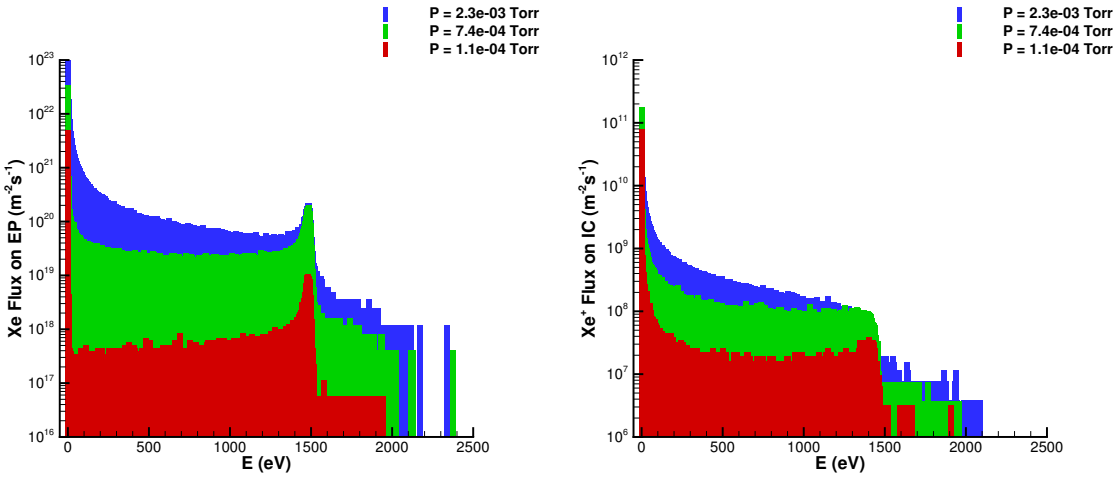

(a) (b)

Figure 5.3: Wall flux distributions of particle energy for the +10 V biased configuration: (a) Xe on the Exit Plate (EP); (b) Xe^{+} on the Inner Cylinder (IC).

5.1.2 Positively-biased Test Cell

The wall fluxes of interest to PIE versus particle energy for the +10 V biased operation of the Test Cell environment are presented in Figure 5.3 for low-, medium-, and high-pressure operating conditions showing the threshold-velocity atom flux of interest in Figure 5.3(a) and the low-energy ion flux of interest in Figure 5.3(b).

In Figure 5.3(a), the high flux of atoms at the Exit Plate can be observed following a trend related to the heavy-species collision model showing a low-energy peak, representative of atoms undergoing either low-angle or low-energy VHS-type collisions with other atoms or ions, and a high-energy peak, representative of atoms which were previously ions. The high-energy peaks of atom impact on the Exit Plate are more pronounced compared to unbiased operation; however, the threshold flux regions are of generally lower magnitude. This is possibly due to the slightly higher pressure operating conditions of the biased data set as more collisions occur which equilibrate high-energy particles. In Figure 5.3(b), the flux of ions to the Inner Cylinder shows similar trends to the results of the unbiased data set.

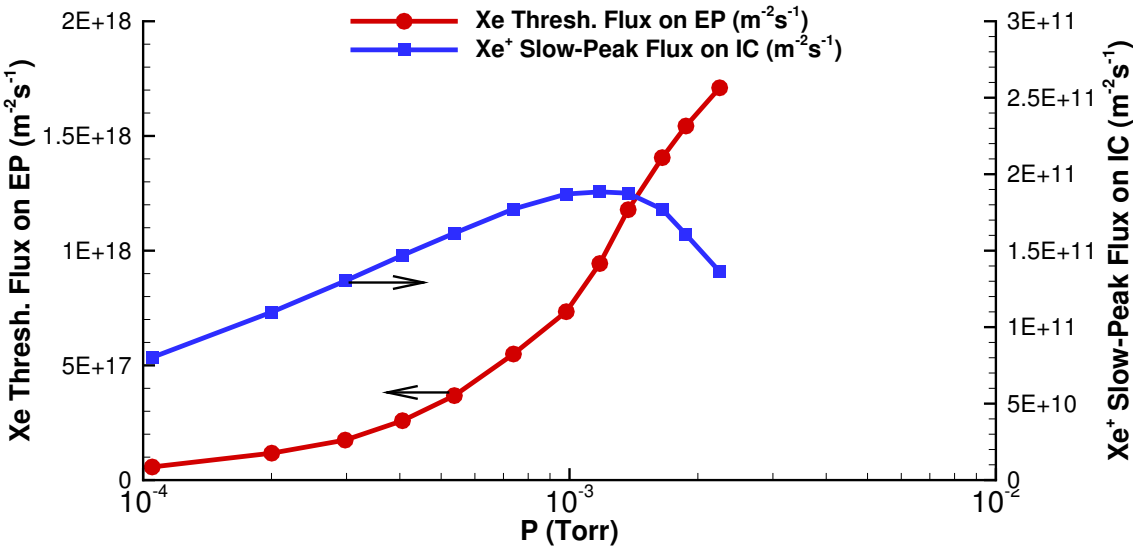

Figure 5.4: Wall flux peak fluxes of interest versus operating condition pressure for the +10 V biased data set.

Specific fluxes of interest versus operating condition pressure are summarized in Figure 5.4, showing atom threshold flux at the Exit Plate and low-energy ion peaks at the Inner Cylinder. These fluxes determine the PIE flux from the electrodes of the Test Cell using the yield-flux relationship found in Equations 3.13 and 3.14.

5.1.3 Negatively-biased Test Cell

The wall fluxes of interest to PIE versus particle energy for the -10 V biased operation of the Test Cell environment are presented in Figure 5.5 for low-, medium-, and high-pressure operating conditions showing the threshold-velocity atom flux of interest in Figure 5.5(a) and the low-energy ion flux of interest in Figure 5.5(b).

In Figure 5.5(a), the high flux of atoms at the Exit Plate can be observed following a trend again related to the heavy-species collision model with low-energy and high-energy atom peaks. The high-energy peaks of atom impact on the Exit Plate are more pronounced compared to the unbiased and positively-biased environments; however,

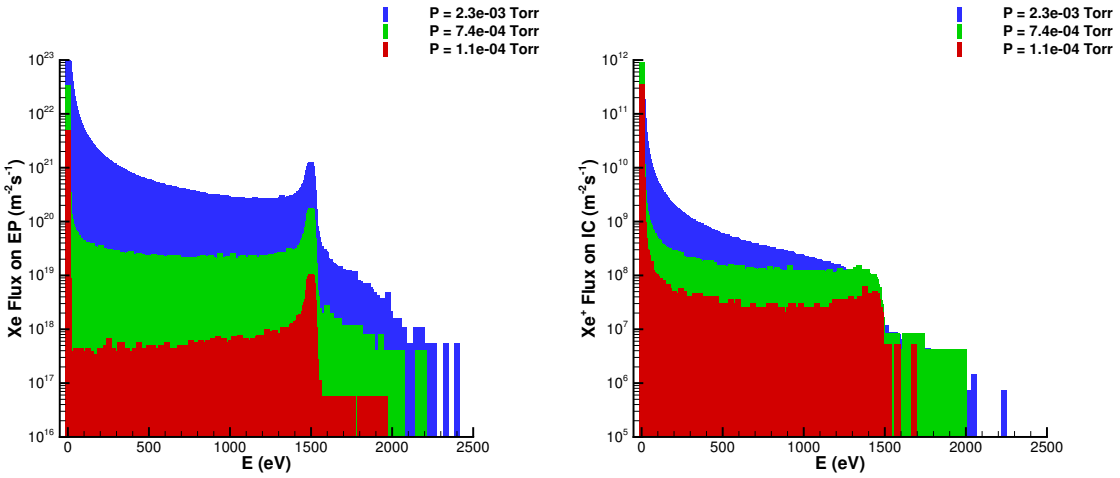

(a) (b)

Figure 5.5: Wall flux distributions of particle energy for the -10 V biased configuration: (a) Xe on the Exit Plate (EP); (b) Xe^+ on the Inner Cylinder (IC).

the threshold flux regions are of generally lower magnitude. In Figure 5.5(b), the flux of ions to the Inner Cylinder again shows similar trends to the other data sets but with larger magnitudes. Specific fluxes of interest versus operating condition pressure are summarized in Figure 5.6, showing atom threshold flux at the Exit Plate and low-energy ion peaks at the Inner Cylinder. The negative biased condition shows non-monotonic behavior in the atom flux at the second highest pressure condition. This behavior is later passed on to the resulting PIE current within the Test Cell due to the dependency on these fluxes, discussed in Section 5.3.3. The exact reason for this behavior is unclear but possibly due to the inability to fully resolve all low-probability collision events resulting in high-energy atoms, as discussed in Section 5.1.1.

A comparison of all peak wall fluxes used in the PIE model can be seen in Figure 5.7, showing peak threshold-level xenon flux at the Exit Plate in Figure 5.7(a) and peak low-energy xenon ion flux at the Inner Cylinder in Figure 5.7(b). It can be seen that the threshold-level xenon flux is, in general, a larger magnitude flux than that of the xenon ions. All fluxes show a trend of growing as operating condition pressure

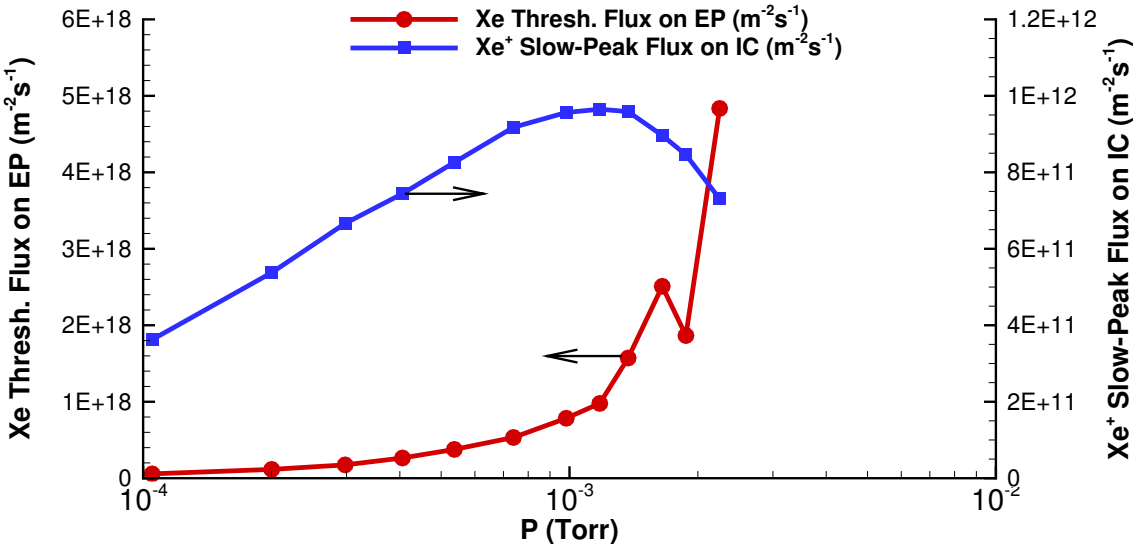

Figure 5.6: Wall flux peak fluxes of interest versus operating condition pressure for the -10 V biased data set.

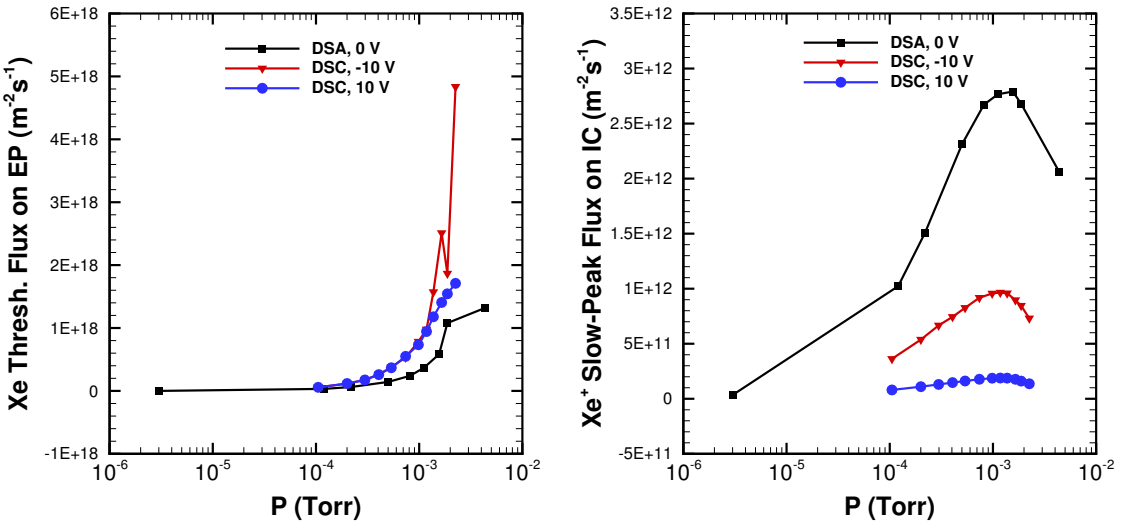

(a) (b)

Figure 5.7: Comparison of peak wall fluxes for the unbiased and biased data sets: (a) Xe on the Exit Plate (EP); (b) Xe^+ on the Inner Cylinder (IC).

Emitter	**Unbiased Collector**		**+10 V Biased Collector**		**-10 V Biased Collector**	
	IC	EP	IC	EP	IC	EP
IC	0.85	0.07	0.99	0.01	0.66	0.20
EP	0.95	0.02	0.98	0.02	0.20	0.77

Table 5.1: Summary of electron collection percentage, P, illustrated in Figure 5.8, which is notated by matching the emitting electrode of interest with the collecting electrode for the environment of interest with the resulting value describes the percentage of emitted electrons which arrive at the collector.

increases with the ion flux at the Inner Cylinder displaying a dip at the highest of pressures.

5.2 Secondary electron behavior

After PIE fluxes are determined at the various electrodes according to the flux values of Figures 5.2, 5.4, and 5.6, electron emission from the Exit Plate and Inner Cylinder is simulated corresponding to the respective yields and EEDFs as previously described in Section 3.5. The purpose of these simulations is to track the flux of emitted electrons which are "cross-collected" at the other electrodes as well as the flux of back-streaming electrons which are re-collected at the same electrode. The electron emission is simulated in two phases: Inner Cylinder-emission and Exit Plate-emission. These simulations are run to steady state and the total emitted and collected electron fluxes are used to calculate cross-collection and back-streaming contributions.

The fluxes collected are reported as percentages for both unbiased and biased Test Cell operation in Table 5.1, quantifying the amount of back-streaming and cross-collection behavior of the emitted electrons. The percentages follow a common sense pattern based on the fundamental principle of electrostatic attraction and repulsion: the positively biased case shows the highest percentage of electron transport; the negatively biased case shows the smallest percentage of electron transport; the unbiased case shows the "control" value which is between the two biased values.

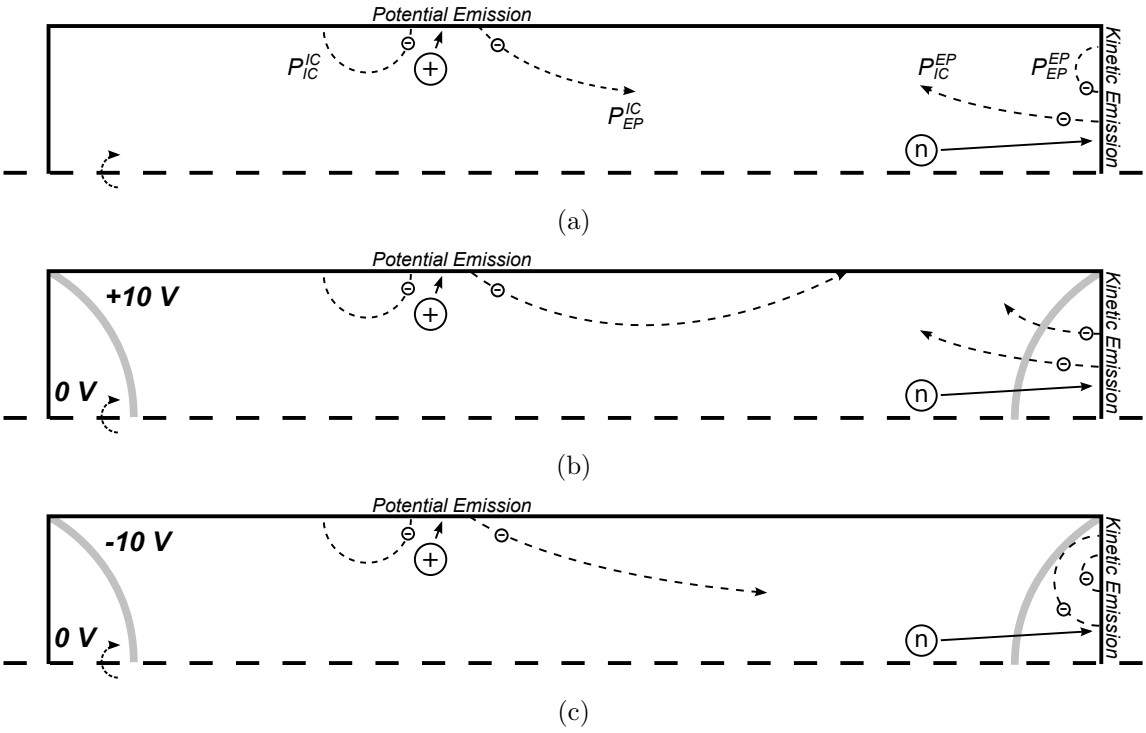

Figure 5.8: Illustrations of the unbiased (a), +10 V biased (b), and −10 V biased (c) electron behaviors of the Test Cell. Each of these illustrations attempts to visualize the populations of emitted and collected electrons, including those which are back-streamed.

These data are then used to calculate updated currents at the Inner Cylinder and Exit Plate relying on the principle that an emitted electron is indistinguishable from a collected ion from a current-collection standpoint. Using the naming convention of the percentage of back-streaming Inner Cylinder-emitted electrons as "P_{IC}^{IC}" and Inner Cylinder-emitted/Exit Plate-collected electrons as "P_{EP}^{IC}", using emitting electrode as the superscript and collecting electrode as the subscript, the current at each electrode can be calculated using the emitted electron currents in Equations 3.13 and 3.14 as

$$I_{EP,PIE} = \overbrace{I_{EP}}^{\substack{\text{Original EP} \\ \text{ion current}}} + \underbrace{I_{e,k}\left(1 - P_{EP}^{EP}\right)}_{\substack{\text{Backstreaming EP} \\ \text{electron current}}} - \overbrace{P_{EP}^{IC} I_{e,p}}^{\substack{\text{Cross-collected} \\ \text{IC}\rightarrow\text{EP electron current}}} \tag{5.1}$$

and

$$I_{IC,PIE} = \overbrace{I_{IC}}^{\substack{\text{Original IC} \\ \text{ion current}}} + \underbrace{I_{e,p}\left(1 - P_{IC}^{IC}\right)}_{\substack{\text{Backstreaming IC} \\ \text{electron current}}} - \overbrace{P_{IC}^{EP} I_{e,k}}^{\substack{\text{Cross-collected} \\ \text{EP}\rightarrow\text{IC electron current}}} . \tag{5.2}$$

These current values are then used in comparison with the original simulation and experimental values to observe the effect of the implemented PE and KE models. This behavior is illustrated phenomenologically in Figure 5.8, showing the unbiased case and the naming convention for the collector percentages as well as the positive and negative biased cases and their intrinsically different nature.

Using a mid-pressure operating condition of DSA as an example of an electron emission solution, contours of density and emission stream traces can be seen in Figure 5.9, showing PE electrons from the Inner Cylinder in Figure 5.9(a) and KE electrons from the Exit Plate in Figure 5.9(b). The PE emission in Figure 5.9(a) shows a large amount of electron flux travelling to both the Exit Plate and Upstream Plate regions with also a large amount of back-streaming. The KE emission in Figure 5.9(b), however, shows almost zero back-streaming characteristics of the electrons,

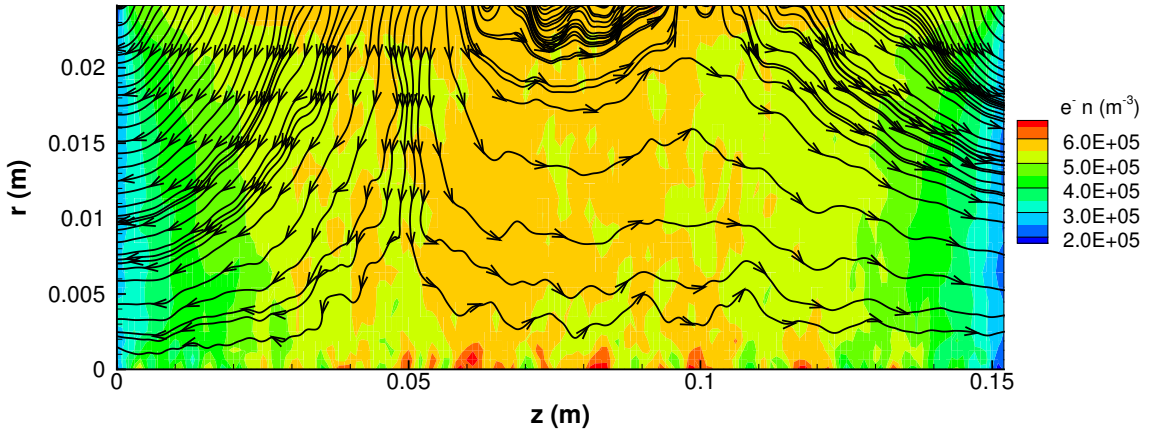

(a)

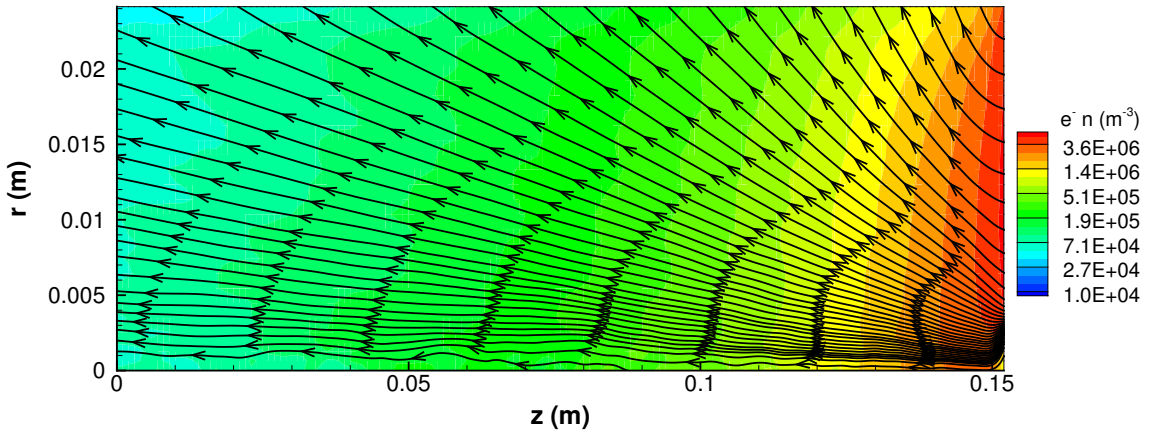

(b)

Figure 5.9: Contours of electron number density with accompanying stream-traces illustrating secondary emission of electrons from the Inner Cylinder (a) and Exit Plate (b) in which cases of back-streaming and cross-collection are prevalent.

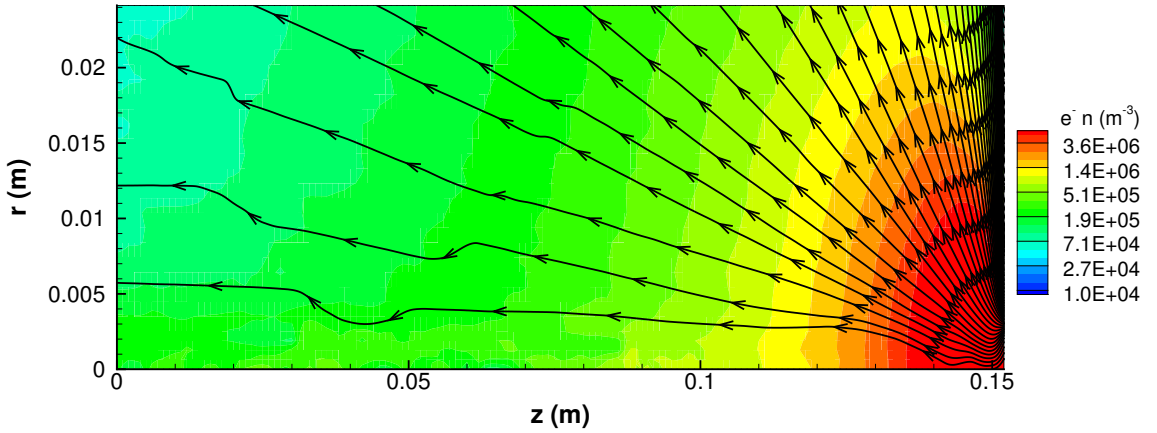

Figure 5.10: Contours of electron number density with accompanying stream-traces illustrating secondary emission of electrons from a localized region of 1 mm along the Exit Plate surrounding the Exit Orifice.

the majority of which travel radially and are cross-collected at the Inner Cylinder.

5.2.1 Localized emission study

The emission process is also varied to account for the focusing of threshold-level high-energy atom impacts occurring within the first few millimeters of the Exit Plate, a topic discussed in Section 4.4.1. The emission region is decreased in size to a radius of only 1 mm above the Exit Orifice and simulated. The resulting solutions can be seen in the contours of density and emission stream traces of Figure 5.10, illustrating this localized emission from the Exit Plate.

For this localized emission, the resulting fluxes of cross-collection and back-streaming electrons are found to be essentially equivalent to those of the full-EP emission with the majority of emitted electrons traveling from the Exit Plate to the Inner Cylinder. Even in an unbiased environment, this propensity of the emitted electrons to travel toward the Inner Cylinder is most likely due to a combination of basic elastic collisions and charge separation electrostatic forces from the bulk of the electrons emitted.

5.3 Effects of particle-induced electron emission

This section provides the results of current collection due to the previously described PIE models. The performance of the PIE model is largely related to the identification of the dominant electron emission mode (either PE or KE) which is determined by the behavior of the electrons when either attracted or repelled by the Inner Cylinder. As an example, when the Inner Cylinder is biased positively, it becomes electron-collecting and therefore KE emission from the Exit Plate dominates. Conversely, when the Inner Cylinder is biased negatively, it becomes electron-repelling and therefore PE emission from the Inner Cylinder will be dominant.

Changes in observed current at the Exit Plate and Inner Cylinder are made using the PIE current formulas of Equations 5.1 and 5.2. Unbiased results are discussed in Section 5.3.1 while positively- and negatively-biased results are discussed in Sections 5.3.2 and 5.3.3, respectively.

5.3.1 Unbiased Test Cell

Original and PIE-included current collection results can be seen in Figure 5.11 for the unbiased Test Cell environment. Current collection trends including PIE show an improvement in comparing with the experimental measurements, decreasing the amount of current collected at the Inner Cylinder and increasing the amount of current collected at the Exit Plate. This effect is most noticeable in the high-pressure region, the region of greatest current collection disparity between original simulation and experimental results.

This change in the Exit Plate current is due to the KE process which appears to be the dominant mode of electron emission in the Test Cell, illustrated in Figure 5.8(a). This mode is considered dominant because, as discussed in Section 5.1.1, the flux of threshold-level atoms at the Exit Plate is several orders of magnitude larger than the flux of low-energy ions at the Inner Cylinder, resulting in a more pronounced effect

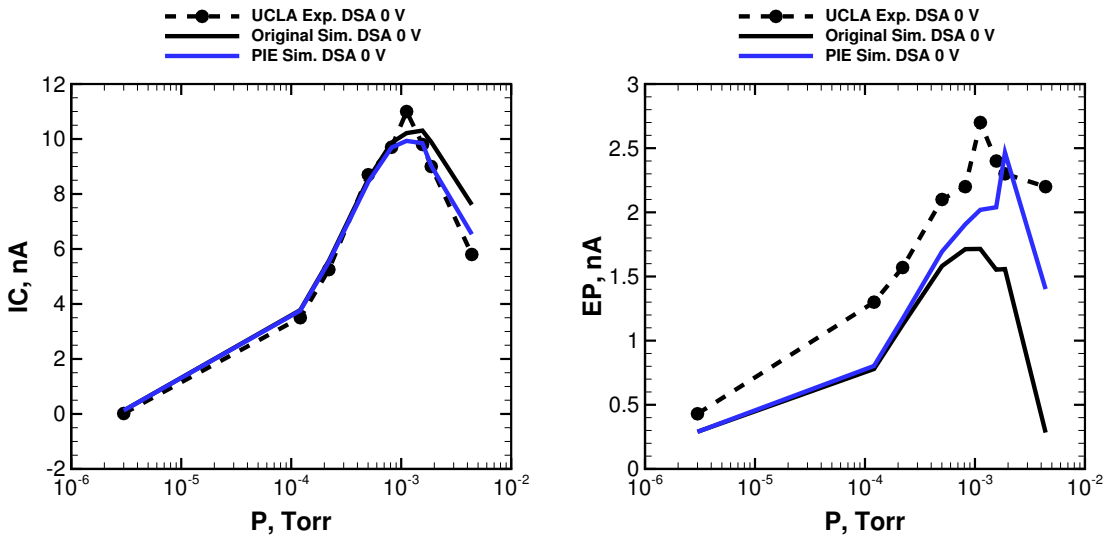

(a) (b)

Figure 5.11: Original and PIE-included current collection results for the unbiased data set at the Inner Cylinder (a) and Exit Plate (b).

on electrode-collected current due to the KE process. This can be considered to be directly related to the VHS cross-section compared to the MEX/CEX cross-sections; as high-energy atoms are created due to CEX, they are subject to VHS collisions with background xenon atoms which have cross-sections an order-of-magnitude less than MEX/CEX, therefore leading to a larger number of high-energy atoms approaching the Exit Plate. Additionally, because no significant electrostatic attraction or repulsion is present, it is concluded that KE from the Exit Plate is the dominant source of electron current in the Test Cell.

5.3.2 Positively-biased Test Cell

Original and PIE-included current collection results can be seen in Figure 5.12 for the positively biased +10 V Test Cell environment. Current collection trends due to PIE again show an improvement in comparing with the experimental measurements with an augmentation of predicted current at the Exit Plate due to KE and a de-

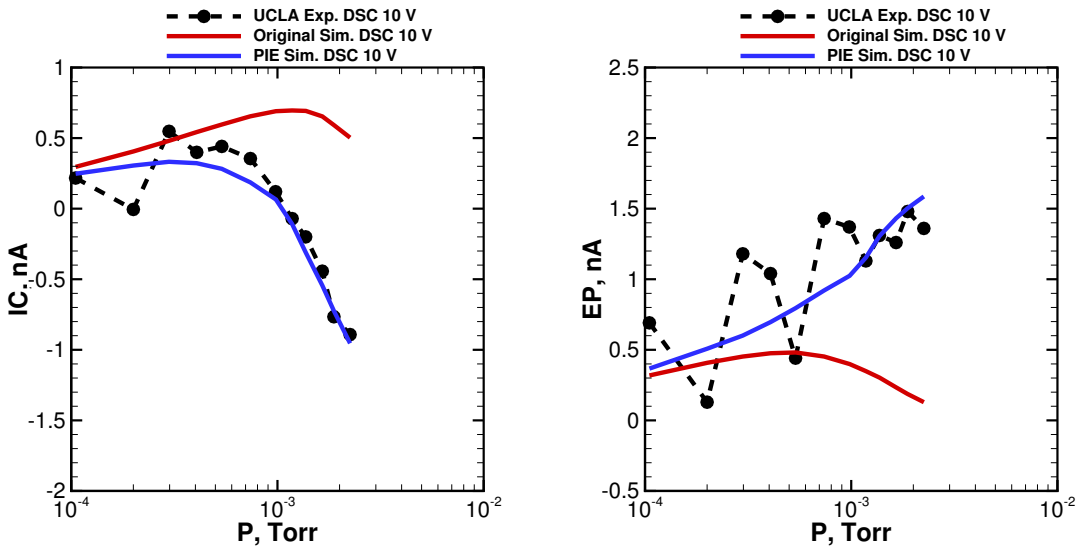

Figure 5.12: Original and PIE-included current collection results for the +10 V biased data set at the Inner Cylinder (a) and Exit Plate (b).

crease in current at the Inner Cylinder due to electron collection. In addition, this mode of PIE is able to capture the negative current trends seen in the experimental measurements, a result that is impossible given previous attempts using ion-only simulations [136].

Increased electron collection at the Inner Cylinder, and the resulting negative observed current collection, is due to the electrostatic attraction of secondarily-emitted electrons via the KE process at the Exit Plate to the positively-biased Inner Cylinder, illustrated in Figure 5.8(b). Described previously for the unbiased environment, this seems to be the dominant electron transport process in the Test Cell. Therefore, the positive bias established at the Inner Cylinder is simply further amplifying this process via electrostatic attraction on the KE electrons.

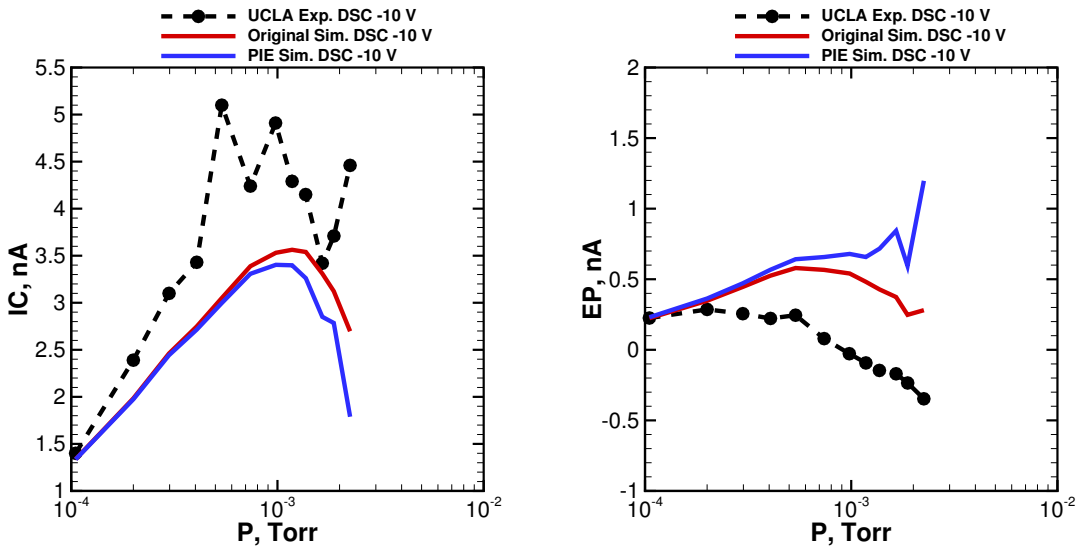

(a) (b)

Figure 5.13: Original and PIE-included current collection results for the -10 V biased data set at the Inner Cylinder (a) and Exit Plate (b).

5.3.3 Negatively-biased Test Cell

Original and PIE-included current collection results can be seen in Figure 5.13 for the negatively biased -10 V Test Cell environment. Current collection trends including PIE show an incorrect augmentation of observed current at the Exit Plate and an incorrect diminishing of current at the Inner Cylinder.

The reason for the poor trends in this environment is due to the inability to correctly resolve a dominant PE process from the Inner Cylinder. The PE process is considered dominant in this environment because the transport of KE electrons is hindered from the established electrostatic repulsion from the Inner Cylinder, illustrated in Figure 5.8(c). Therefore, PE electrons from the Inner Cylinder are expected to travel to the Exit Plate and cause negative current collection. It is obvious, however, that not enough PE electrons are collected at the Exit Plate. This phenomenon is discussed further in the next section as the total yields of the KE and PE process are analyzed. Furthermore, the interesting behavior in the high-pressure region due

to the flux of high-energy atoms at the Exit Plate can be seen in Figure 5.13, illustrating the sensitivity of the solution to wall flux predictions, even in the case of a non-dominant emission mode.

5.4 Sensitivity analysis

This section aims to study the accuracies of the PIE models as described and implemented in this present work. The models' efficacies are directly related to their abilities to capture the physical phenomenon while accurately simulating current collection in the Test Cell, the only physical source of measurement available for comparative analysis. The KE analysis is discussed in Section 5.4.1 and the PE analysis is discussed in Section 5.4.2.

5.4.1 Efficacy of the KE total yield

Simulations of the Test Cell environment in which the dominant mode of secondary electron creation is at the Exit Plate due to KE from high-energy atoms show good agreement with experimental measurement yet very much rely on the KE corrective factor, explained in Section 2.3.2.1. This corrective factor arises as a compromise between the lack of data for the xenon-stainless steel interaction at energies of interest and the need to build a physics-based model for the KE process. It is a semi-empirical parameter which, described earlier, is a combination of observed lower-magnitude emission due to neutral particles and the fitting of these reduced models with the Test Cell data. It is the goal of this work to keep parameter tuning to a minimum in order to arrive at a physics-based model.

Figure 5.14 shows the effect of varying the KE yields between $\gamma_k = 1, 2, 3, 4,$ and 5×10^{-6}, with the original value being 3×10^{-6}. It can be seen that the original yield is chosen because it lines up almost perfectly with the Test Cell data. The choice of corrective factor is highly dependant on the ability to gain more insight into the atom-

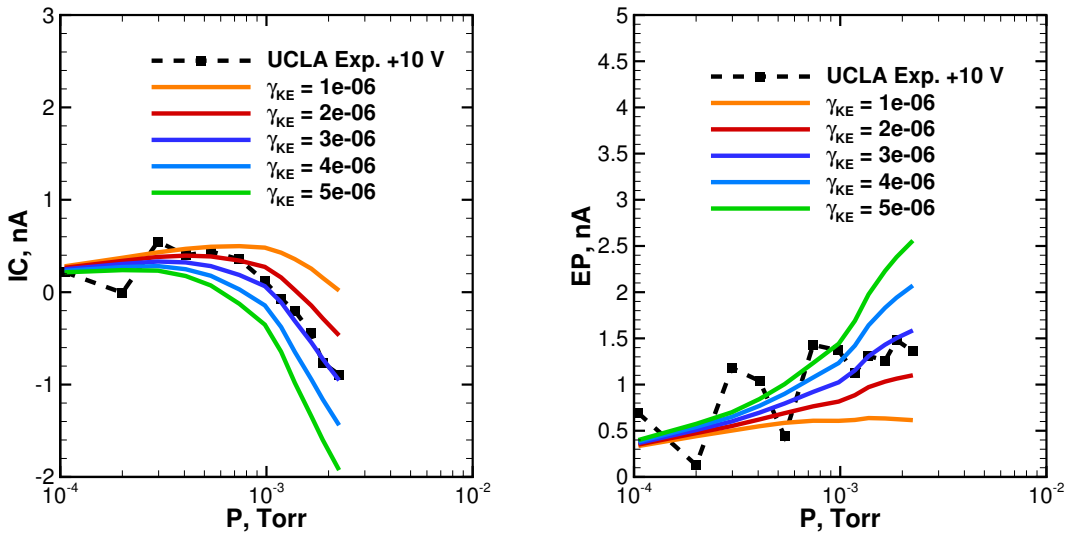

(a) (b)

Figure 5.14: Sensitivity analysis of current collection results for the +10 V biased data set at the Inner Cylinder (a) and Exit Plate (b) for a range of KE total yields, γ_k.

and ion-surface interactions through future experiments. Much of the data used in the extraction of the KE total yield is either *i*) extrapolated from the parameters of materials which are not stainless steel, or *ii*) interpolated from large data sets of yield from other similar projectiles and materials.

5.4.2 Efficacy of the PE total yield

The PE process is the key to simulating the negatively-biased environment as the Inner Cylinder becomes an electron-repelling surface. This means that electrons from the KE process, the naturally dominant process in the Test Cell due to the higher fluxes of threshold-level neutral particles resulting from CEX collisions, will not have as much of an effect on current collection because of back-streaming and deflection.

Figure 5.15 shows the effect of varying the total PE yield as γ_p = 0.016, 0.16, 0.32, 0.8, and 1.6. It can be seen that, while increasing the PE yield by about 50 to a value of 0.8 brings the magnitude of the simulated Exit Plate current to improved

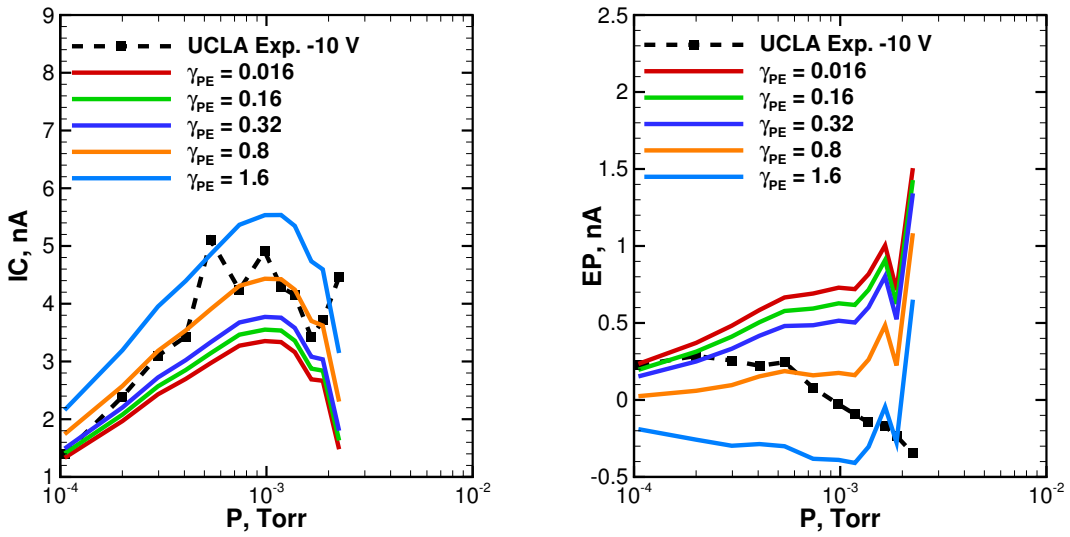

(a) (b)

Figure 5.15: Sensitivity analysis of current collection results for the -10 V biased data set at the Inner Cylinder (a) and Exit Plate (b) for a range of PE total yields, γ_p.

agreement with the measurements, there is a fundamental difference in the trend of the current collection. One possibility can be the effect of secondary emission on clean versus dirty surfaces, an assumption which is not taken into account in this work and discussed further in Section 6.3. It is hypothesized, however, that this is not an issue with the yield but rather the flux of a PE-augmenting species to the Inner Cylinder which is not being captured by the present simulations.

Unlike the KE process, the PE process is related to the internal properties of the projectile. Therefore, rather than the inaccuracies being rooted in material interaction properties, the reason for the inability to resolve a higher PE yield is most likely due to the inability to resolve the entirety of the Auger neutralization process for the ground state and various metastable states of low-energy particles at the surface of the Inner Cylinder. Despite the Auger process being a form of neutralization, Auger neutralization is sometimes preceded by resonance ionization [70] in which ground state excited atoms are first ionized so that neutralization can occur. These metastable

states, both charged and uncharged, have varying ionization energies related to the energies of the valence electrons of the projectile. This allows for PE electrons to be emitted by a flux of species that is not, *a priori*, a charged ion, thus augmenting the PE process. This phenomenon, however, is much more difficult to characterize in a reduced model already built on unknown parameters and assumptions.

Previous work by Pullins [21] and Dressler [54] suggested that metastables could exist as a small percentage of both xenon atom and ion populations in plume-like environments such as the Test Cell. Taking the case of xenon ions, for example, a distribution of 16 metastable states exists with ionization energies between 23.4 eV and 28.69 eV above the ground state of neutral xenon. These different internal energies means that every metastable population can be described by an entirely new set of PE yields, all higher than for the basic ground state population used in the present work. Additionally, there would be a probability associated with resonance ionization occurring for each state. A full characterization of these populations could lead to an augmented PE yield; furthermore, this would further assist in the characterization of the KE process, by comparison.

5.5 Summary of PIE-included current collection

This chapter was successful in illustrating the ability of the PIE models to capture electron emission and transport for most of the conditions of the Test Cell.

Section 5.1 illustrated the important populations of high-energy atoms and low-energy ions in the Test Cell, resulting in quantified peak values of flux to be used as inputs to the PIE models. The behavior of the heavy species wall fluxes showed the response of the heavy species collision models, resulting in distinct peaks of high- and low-energy ions and atoms.

Section 5.2 provided a quantification of the electron transport within the Test Cell, showing the varying nature of the electron back-streaming and cross-collection as the

environment changed. A method of including current due to this electron behavior was established so that the effect of the PIE models could be observed in terms of collector current.

After including the electron transport behavior into the simulations, final results of PIE-modeled current collection in the Test Cell were presented in Section 5.3, showing the ability to capture the unbiased and positively biased environments very well. The efficacy of the KE and PE models was then studied in Section 5.4. This analysis showed the sensitivities of the yields of both models, paying particular attention to the inability of the PE model to resolve certain physical phenomena.

The combination of heavy species and electron-emission transport models has led to a better characterization of the transport physics within this representative environment and resulted in a validation of the models used to characterize the Test Cell.

CHAPTER VI

Conclusions

The purpose of this chapter is to summarize the work described in the dissertation, outline the specific contributions made, and suggest future directions for the work. Section 6.1 provides a detailed summary and review of all the work of this dissertation. Section 6.2 then details specific contributions in the context of the goals outlined in Chapter I. Finally, Section 6.3 expands on various topics which are important to future investigations of the Test Cell, heavy species collision modeling, and secondary electron emission.

6.1 Summary and Review

The goal of this dissertation involved the modeling of fundamental plasma physics processes occurring within environments that are similar to that of the discharge and plume regions of electric propulsion devices such as Hall effect thrusters. The research was conducted as a collaborative effort with the Plasma & Space Propulsion Laboratory at UCLA as part of the University of Michigan/AFRL Center for Excellence in Electric Propulsion (MACEEP). Transport physics, such as particle-particle collisions and particle-induced electron emission, were simulated within the UCLA experimental facility and its representative electric propulsion environment in order to both validate the models as well as investigate newly-implemented, reduced-order

models.

Introduction

Chapter I provided motivation and background for the dissertation. It was introduced in Section 1.1 that there exist unresolved physics in electric propulsion (EP) device plumes which have affected the ability to confidently study and investigate these devices. The basis for EP devices was established in Sections 1.2.1 and 1.2.2 and the Hall effect thruster (HET) was introduced as the primary device of focus in Section 1.2.3. The simplified experimental facility which would be the basis of all comparisons with measurement, the UCLA Test Cell, was then introduced in Section 1.2.4, giving a brief overview of the basic setup of the accelerated ion beam and the controlled background-gas environment. The field of computational plasma physics as applied to EP and the various attempts at modelling heavy-species and secondary electron emission was introduced in Sections 1.2.5 to 1.2.7. The goals and organization of the dissertation were then presented in Sections 1.3 through 1.4.

Theory of Heavy Species Collisions and Electron Emission

Chapter II introduced and explained in detail the various theoretical models required in the simulation of the various transport physics within the Test Cell. The basis of rarefied gas dynamics was introduced in Section 2.1, defining the flow regime as rarefied in Section 2.1.1, an assumption which most of the theories are based upon. The concept of a collision cross-section was introduced in Section 2.1.2 including the differential cross-section which provides information about the post-collisional scattering nature of an interaction and proves to be very important for atom-ion interactions. The transport models of interest for heavy-species interactions were then explained in detail in Section 2.2. The isotropic Variable Hard Sphere (VHS) collision model for atom-atom collisions was presented in Section 2.2.1 followed by the anisotropic

momentum exchange (MEX) and charge exchange (CEX) atom-ion collision models in Section 2.2.2 in which both total and differential cross-sections were detailed.

Lastly, the theory of particle-induced electron emission (PIE) was presented in Section 2.3. The theory of potential emission (PE) was first introduced in Section 2.3.1 as a source of secondary electrons for low-energy charged particles at the surface, dependent on the internal properties of the projectile and independent of kinetic effects. The theory of kinetic emission (KE) was then introduced in Section 2.3.2 as the primary source of secondary electrons from a surface bombarded with particles which have a large kinetic energy. In each of these sections, a total yield and electron energy distribution function (EEDF) was established based on reduced order models and assumptions for material surface properties which were derived from highly-repeatable historical data. Lastly, an elastic scattering model for the electrons was described in Section 2.3.3.

Numerical Implementation of Transport Models and the Experimental Domain

Chapter III described the numerical implementation of the theoretical models of Chapter II. The DSMC-PIC approach to the simulation of charged, rarefied flows was outlined in Section 3.1, covering the direct simulation Monte Carlo (DSMC) and particle-in-cell (PIC) algorithms, the simulation package MONACO-PIC developed at the University of Michigan, and details on the special treatment of particle weighting and boundary conditions throughout Sections 3.1.1 to 3.1.5.

Section 3.2 then described the numerical implementation of the UCLA Test Cell and how its well-characterized boundary conditions translate to a numerical domain. The method for solving for the non-quasineutral electric potentials within the Test Cell was described in Section 3.3, detailing previous implementations, assumptions of non-neutrality, and the finite-element implementation and validation of the new

method of solving the Poisson equation directly.

The numerical implementation of the collision models detailed in Chapter II were then described in Section 3.4, outlining the No Time Counter method of colliding neutral heavy species in Section 3.4.1 and differential cross-section curve-fit method of choosing post-collision scattering angle in Section 3.4.2. Lastly, the implementation of the reduced PIE models are outlined in Section 3.5 focusing on the implementation of PE and KE total yields in Section 3.5.1 and EEDFs in Section 3.5.2.

Heavy Species Simulations of the Unbiased and Biased Test Cell Environment

Chapter IV presented the results of comparisons between experimental measurement and atom- and ion-only simulation of current collection at the various electrodes of the Test Cell. Section 4.1 began with an analysis of current collection in the unbiased Test Cell environment, considering both Data Set A (DSA) and Data Set B (DSB) in Section 4.1.1 and how a very repeatable trend could be established in both low- and high-pressure conditions of Test Cell operation. These trends followed a slight over-prediction of current collected at the Inner Cylinder and an under-prediction of current collected at the Exit Plate, also showing a large disparity in Exit Plate comparisons occurring at approximately 1 mTorr. Additionally, the physics and modeling assumptions which dominate the transport within the Test Cell were varied in Section 4.1.2 by simulating the environment *i*) without collisions, *ii*) without electrostatic forces, and *iii*) with an isotropic rather than anisotropic collision model, proving that not only is the Test Cell a collision-dominated rather than electrostatics-dominated environment, but that the success of current collection predictions relied on the anisotropic nature of post-collision scattering properties.

The results of heavy species simulation of the environment while biasing the Inner Cylinder positively and negatively were then compared to measurements in Sec-

tion 4.2. The positively-biased simulation cases for Data Set C (DSC) and Data Set D (DSD) were detailed in Section 4.2.1 and displayed repeatable trends of under-predicting current collected at the Exit Plate while being unable to resolve negative current collection at the Inner Cylinder. Opposite trends were observed for the negatively-biased cases of Section 4.2.2 which under-predicted Inner Cylinder current while being unable to resolve negative current collection at the Exit Plate.

A small, but finite, beam divergence was introduced in Section 4.3 which closed the gap between the low-pressure current disparities but still left the high-pressure current collection trends unchanged. Additionally, work was carried out in Section 4.4 which attempted to predict future modification to the Test Cell. The results of this chapter, however, portrayed a need for inclusion of electron physics in order to resolve negative currents at certain electrodes as well as the under-prediction of current at the opposite electrodes.

Simulation of Particle-Induced Electron Emission in the Test Cell

Chapter V presented results which describe how the flux of heavy species at the electrodes of the Test Cell affects the behavior of emitted electrons from these electrodes and the total current collected at these electrodes. Section 5.1 began by describing the fluxes of the xenon populations of interest at the walls of the Test Cell: low-energy ions and high-energy atoms. These fluxes directly determine the fluxes of electrons from the emitting electrodes and are essential in determining the dominant mode of emission in the various environments (either PE or KE). Sections 5.1.1 through 5.1.3 detailed the magnitudes of these populations at the Inner Cylinder and Exit Plate, defining the peak values at these electrodes which would be used as the input values in the numerical implementation of the PIE models.

The behavior of secondary electrons was then described in Section 5.2 in which steady-state percentages of back-streaming and cross-collected electrons were pre-

sented in order to build a complete phenomenological model of the KE and PE processes. Number density contours and stream traces of electron travel illustrated the general behavior of electrons as they emit from one electrode and travel to the other electrodes (or back to the source, in the case of back-streaming). The behavior of electrons was also varied to account for a localized region of emission in Section 5.2.1 in the case that the PIE processes were only located near the Exit Orifice.

Final results of current collection including PIE were then described in Section 5.3. Unbiased current collection results in Section 5.3.1 and positively-biased results in Section 5.3.2 showed very good prediction of current collection when PIE models were included. It was hypothesized that this is because these environments are dominated by the KE process of emission from the Exit Plate which is captured well in the simulations. However, the negatively-biased results of Section 5.3.3 still showed disparities in the current collection comparisons, most likely due to the inability to resolve all of the physics of the PE process.

The sensitivities of these models were then investigated in Section 5.4. Section 5.4.1 first considered the efficacy of the KE model which is limited by its high sensitivity to material parameters which are mostly unknown values or extrapolated from similar materials. However, it is inferred that the reduced KE model is close to capturing much of the phenomena as its effect on current collection showed good trends. The efficacy of the PE model was then investigated in Section 5.4.2. Unlike the KE process, the PE process is related to the internal properties of the projectile. Therefore, rather than the inaccuracies being rooted in material interaction properties, it was postulated that the reason for the inability to resolve a higher PE yield is most likely due to the inability to resolve the entirety of the Auger neutralization process for the ground state and various metastable states of low-energy particles at the surface of the Inner Cylinder.

6.2 Contributions

As laid out in Section 1.3, the scope of this project and dissertation is to improve the understanding and accuracy of the modeling of fundamental physics behind certain heavy species and electron transport physics in a well-defined environment which mimics that of a HET plume. This work has resulted in the following specific contributions.

6.2.1 Validation of heavy species collision models

The ability to reproduce current collection in the Test Cell from an anisotropic set of transport models between atoms and ions has been presented. Chapters II and III described the theoretical and numerical implementations of the heavy species collision models and Chapter IV presented the results of ion-only current collection in the Test Cell. This approach was successful in showing that the method for choosing a differential cross-section curve-fit can be extended to higher collision energies. These results also portrayed a collision-dominated regime in which collisions-alone, without electrostatics, could nearly reproduce the current collection behavior in an unbiased environment. Additionally, it was shown that an isotropic implementation of these heavy species transport models over-predicts high-angle scattering current collection at the Inner Cylinder and under-predicts low-angle current collection at the Exit Plate. All of these observations were made from simulations of current collection on a novel facility. Efforts were also made to predict future observations taking into consideration modifications to the facility. Lastly, a method for solving the Poisson equation directly without using assumptions of electron density was implemented in the simulation package in order to minimize unnecessary assumptions and represent a more physics-based environment.

These contributions to HET plume-like, heavy-species transport models are important in the characterization of electric propulsion devices and the reconciliation of

disparities often found in the measurements made by Faraday probes in high-angle regions, as discussed in Section 1.2.6.

6.2.2 Introduction of PIE as relevant physics and transport mechanism

The governing equations of PIE were gathered and condensed to reduced-order models in Chapter II. The two major modes of PIE emission, KE and PE, were each investigated as the two sources of current disparity within the Test Cell environment, made apparent by the repeatable negative current collection of certain regimes. The PIE theory was reduced to models for total yield and EEDF for both emission modes. PIE was justified as a source of electrons within the Test Cell due to the fluxes of energetic and charged particles on the stainless steel walls.

This environment, containing a mixture of low-energy charged particles and high-energy particles, is often seen in EP device plumes and could interact with widely used diagnostics such as Faraday probes. Furthermore, the lack of specific data and parameters for xenon-stainless steel interactions for both atoms and ions is addressed. Many assumptions are presented and justified about these interactions in order to create a physics-based model while still relying on semi-empirical models which can further be refined as more information is gathered about the secondary emission parameters for materials specific to the advancement of electric propulsion measurements and Faraday probes.

6.2.3 Implementation and analysis of PIE reduced-order models

The reduced-order PIE models introduced in Chapter II were implemented into the DSMC-PIC framework of MONACO-PIC via the methodology of Chapter III in a way which is straightforward and computationally inexpensive. Rather than perform a fully kinetic simulation attempting to resolve all physics simultaneously, it was shown that MONACO-PIC could be run to a steady-state atom-ion solution

and then subsequently run to steady-state electron emission solutions from the two separate electrodes, the Inner Cylinder and Exit Plate, independently. The theorized yields and EEDFs were simulated as current fractions and probability distribution function curve fits, respectively. The resulting current collection behavior including PIE physics was presented in Chapter V and showed successful current collection behavior for most of the environments of the Test Cell. Both modes of emission, KE and PE, were analyzed for sensitivities, focusing on those environments for which PIE theory did or did not positively affect current comparisons.

As computational efficiency is often an important factor in the simulation of HETs and other electric propulsion devices, this method of implementing PIE in an electric propulsion context could lead to further analysis of the Faraday probe plume measurements and the effect of secondary electrons on device characterization.

6.3 Recommendations for Future Work

There are several topics and issues related to the Test cell, heavy species collision modeling, and PIE theory which are raised by this dissertation in which future efforts are needed.

6.3.1 Upstream Test Cell current collection

As described in Section 4.4.2, there are regions in the Test Cell which, at the time of this dissertation, do not contain an electrode to collect current. More specifically, the Upstream Plate (UP) was suggested at the upstream location of the Test Cell in order to fully characterize the total current of the scattering ions and emitting electrons in the upstream location. In the original conception of the Test Cell, the regimes at which back-scattering becomes non-trivial were possibly not taken into consideration. This is because back-scattering will only occur in a multi-collisional environment which, for the Test Cell, occurs at approximately 1 mTorr. However,

as the Test Cell is advanced and modified to perform experiments and make further observations, care must be taken to have a robust facility which has high measurement fidelity at all possible operating regimes.

6.3.2 Spatial current collection along electrodes

Spatial resolution of current collection at the electrodes of the Test Cell is another modification which would help increase the fidelity of both the heavy species collision models and the PIE models. While the large aspect ratio of the Test Cell allows for the separation of MEX and CEX atom-ion interactions due to the post-collision scattering properties of the interactions, the differential cross-sections used in these post-collision properties could be further verified by resolving the location of the scattered ions. Additionally, the ability to control the electric potential or material properties of specific sections of an electrode would allow for a study on the effects of varying these parameters on secondary electron emission, an example being the isolation of certain sections as the focus of dirty versus clean studies of secondary electron emission (SEE) from stainless steel. More information about the interaction of these heavy species with stainless steel would help refine the assumptions used in the PIE theory which currently relies on many assumed material parameters and conditions of the surface.

6.3.3 A dynamic, energy-dependent anisotropic collision model

One major limitation of the anisotropic MEX/CEX collision models as implemented here is the fitting of the differential cross-sections associated with only one collision energy. While this model is justifiable for a mono-collisional regime, such as the rarefied, low-pressure operating conditions of the Test Cell, the high-pressure region greater than approximately 1 mTorr represents a transition region which becomes multi-collisional. In this multi-collisional environment, subsequent collisions

after the initial beam ion and background atom collision will be at a lower collision energy and will involve post-collision scattering properties which are derived in the current work for an energy that is higher than the actual collision energy.

For example, as a high-energy ion and low-energy atom interact via a CEX collision, the low-energy atom becomes a low-energy ion in the bulk of the Test Cell. If the background pressure of the Test Cell is relatively high, that low-energy ion will interact with another low-energy atom with a thermal relative velocity, <1 eV, using the post-collision scattering properties derived for a 1.5 keV interaction. A more robust model would allow for the selection of post-collision scattering properties using a "set" of differential cross-section curve-fits which are appropriate for various collision energies between atoms and ions. Therefore, as a collision is paired for selection, both the total and differential cross-sections will be a function of the relative collision energy instead of relying on a pre-calculated distribution of differential cross-sections for post-collision scattering angle.

6.3.4 Inclusion of metastable populations in transport modeling

The dependence of the PE model on the internal energy of the impacting particle poses a limitation for ground-state simulations such as those implemented in these MONACO-PIC analyses. As described in Section 5.4.2, there are many metastable states of xenon which could feasibly have nontrivial populations in the Test Cell environment at the multi-collisional, higher-pressure operating conditions. Section 5.4.2 illustrated not only a disparity in magnitude for PE-induced current but also a fundamental difference in the fluxes used in the PE model.

Including fluxes of metastable populations in the PE would augment the PE emission process from the Inner Cylinder. A set of data for metastable xenon atoms and ions could be implemented into the simulation package, all with unique cross-sections and input parameters for the Test Cell environment. As the simulation reaches steady

state, wall fluxes of all metastable populations could be monitored rather than just the ground and singly-ionized states. Furthermore, these fluxes could be implemented into the PE model with each flux associated with a unique potential energy according to the metastable species, and would help quantify the amount of current emitting from the Exit Plate from the KE process.

6.3.5 Full characterization of stainless steel alloys and surface cleanliness

One of the key sets of assumptions made in Section 2.3 is that all unknown material parameters in both the KE and PE models can be approximated using data from either similar materials or historical trends. This approach, however, has a drawback in that much of the past theory and experimental measurements of PIE are for experiments on metals which are not stainless steel alloys. The majority of collections of historical data are focused on gold or refractory metals due to the genesis of this theory in the field of Ion Neutralization Spectroscopy.

6.3.6 Application of model using Faraday probe and plume data

Lastly, the PIE models were developed and implemented in a general way which simply requires total yields, EEDFs, and *a posteriori* fluxes of heavy species to the emitting walls. Therefore, with sufficient atom and ion plume data, a "correction" could be made to Faraday probe measurements to account for the effects of secondary emission of electrons. This data set could be a combination of numerical and experimental data.

For example, numerical predictions could provide a simplified description of the fluxes and currents to a simulated Faraday probe according to the operating conditions of a well-characterized HET. Experimental measurements could provide the observed current at their associated operating conditions. Combining these flux data with the material properties of the Faraday probe could lead to a zeroth-order approximation of

how much current disparity should arise from PIE, always comparing to experimental measurements in the analysis and validation of the model. Furthermore, Faraday probes are often made out of refractory metals for which there is more of a wealth of secondary emission material parameters.

APPENDICES

APPENDIX A

Data Set A (DSA) operating conditions and total current

The following table describes the details of the total beam current used for DSA, represented as the curve-fit formula used to map total beam current to Test Cell operating condition as well as the specific total currents and operating pressures of the experimental data.

For DSA, the total beam current may be represented using the following formula,

$$I_{\mathrm{DSA}} = 17.74e^{-178.5P} \ \ \mathrm{nA}, \tag{A.1}$$

P (Torr)	I_{DSA} (nA)
3.00×10^{-6}	17.727
1.21×10^{-4}	17.357
2.20×10^{-4}	17.053
5.02×10^{-4}	16.216
8.17×10^{-4}	15.329
1.12×10^{-3}	14.522
1.56×10^{-3}	13.418
1.88×10^{-3}	12.689
4.39×10^{-3}	8.108

Table A.1: Total current values used in MONACO-PIC for DSA fit to the experimental data and using Equation A.1.

using operating condition pressure P in Torr and providing beam current in nanoAmps. Taking this formula and fitting to the pressure and total current conditions provided by UCLA results in the values found in Table A.

APPENDIX B

Data Set B (DSB) operating conditions and total current

The following table describes the details of the total beam current used for DSB, represented as the curve-fit formula used to map total beam current to Test Cell operating condition as well as the specific total currents and operating pressures of the experimental data.

For DSB, the total beam current may be represented using the following formula,

$$I_{\mathrm{DSB}} = 16.74e^{-174.7P} \ \ \mathrm{nA}, \tag{B.1}$$

using operating condition pressure P in Torr and providing beam current in nanoAmps. Taking this formula and fitting to the pressure and total current conditions provided by UCLA results in the values found in Table B.

P (Torr)	I_{DSB} (nA)
3.17×10^{-6}	16.73
1.47×10^{-5}	16.70
3.75×10^{-5}	16.63
7.43×10^{-5}	16.52
1.77×10^{-4}	16.23
3.26×10^{-4}	15.81
9.45×10^{-4}	14.19
1.42×10^{-3}	13.07
2.13×10^{-3}	11.55
3.19×10^{-3}	9.59
4.78×10^{-3}	7.26

Table B.1: Total current values used in MONACO-PIC for DSB fit to the experimental data and using Equation B.1.

APPENDIX C

Data Set C (DSC) operating conditions and total current

The following table describes the details of the total beam current used for DSC, represented as the curve-fit formula used to map total beam current to Test Cell operating condition as well as the specific total currents and operating pressures of the experimental data.

For DSC, the total beam current may be represented using the following formulas,

$$V_{\text{bias}} = -10 \text{ V}, \;\; I_{\text{DSC}} \;\; = \;\; 7.61e^{-362.42P} \;\; \text{nA}, \tag{C.1}$$

$$V_{\text{bias}} = 0 \text{ V}, \;\; I_{\text{DSC}} \;\; = \;\; 7.28e^{-485.84P} \;\; \text{nA}, \tag{C.2}$$

$$V_{\text{bias}} = +10 \text{ V}, \;\; I_{\text{DSC}} \;\; = \;\; -1.39\ln(P) - 7.61 \;\; \text{nA}, \tag{C.3}$$

using operating condition pressure P in Torr and providing beam current in nanoAmps. Taking these formula and fitting to the pressure and total current conditions provided by UCLA results in the values found in Table C.

V_{bias} =	-10 V	0 V	10 V
P, Torr	I_{DSC}, nA	I_{DSC}, nA	I_{DSC}, nA
1.05×10^{-4}	7.33	6.92	5.12
2.00×10^{-4}	7.08	6.61	4.22
2.98×10^{-4}	6.83	6.30	3.67
4.06×10^{-4}	6.57	5.98	3.24
5.37×10^{-4}	6.27	5.61	2.85
7.39×10^{-4}	5.82	5.09	2.41
9.79×10^{-4}	5.34	4.53	2.02
1.18×10^{-3}	4.97	4.11	1.76
1.37×10^{-3}	4.63	3.74	1.55
1.65×10^{-3}	4.19	3.27	1.29
1.88×10^{-3}	3.85	2.92	1.11
2.25×10^{-3}	3.37	2.44	0.86

Table C.1: Total current values used in MONACO-PIC for DSC fit to the experimental data and using Equations C.1 through C.3.

APPENDIX D

Data Set D (DSD) operating conditions and total current

The following table describes the details of the total beam current used for DSD, represented as the curve-fit formula used to map total beam current to Test Cell operating condition as well as the specific total currents and operating pressures of the experimental data.

For DSD, the total beam current may be represented using the following formulas,

$$V_{\text{bias}} = -10 \text{ V}, \;\; I_{\text{DSD}} \;\; = \;\; 12.51e^{-239.32P} \;\; \text{nA}, \tag{D.1}$$

$$V_{\text{bias}} = 0 \text{ V}, \;\; I_{\text{DSD}} \;\; = \;\; 12.30e^{-358.05P} \;\; \text{nA}, \tag{D.2}$$

$$V_{\text{bias}} = +10 \text{ V}, \;\; I_{\text{DSD}} \;\; = \;\; 14.55e^{-1260.73P} \;\; \text{nA}, \tag{D.3}$$

using operating condition pressure P in Torr and providing beam current in nanoAmps. Taking these formula and fitting to the pressure and total current conditions provided by UCLA results in the values found in Table D.

V_{bias} =	-10 V	0 V	10 V
P, Torr	I_{DSD}, nA	I_{DSD}, nA	I_{DSD}, nA
2.30×10^{-5}	12.44	12.19	14.13
7.40×10^{-5}	12.29	11.97	13.25
1.43×10^{-4}	12.09	11.68	12.15
2.63×10^{-4}	11.75	11.19	10.44
4.31×10^{-4}	11.28	10.54	8.45
6.06×10^{-4}	10.82	9.90	6.78
7.81×10^{-4}	10.38	9.30	5.43
9.96×10^{-4}	9.86	8.61	4.14
1.73×10^{-3}	8.27	6.62	1.64
2.07×10^{-3}	7.61	5.85	1.06
3.66×10^{-3}	5.20	3.31	0.14
4.60×10^{-3}	4.16	2.37	0.04

Table D.1: Total current values used in MONACO-PIC for DSD fit to the experimental data and using Equations D.1 through D.3.

BIBLIOGRAPHY

BIBLIOGRAPHY

[1] R. G. Jahn, *Physics of Electric Propulsion*. New York: McGraw-Hill, Inc., 1968.

[2] D. M. Goebel and I. Katz, *Fundamentals of Electric Propulsion: Ion and Hall Thrusters*. JPL Space Science and Technology Series, 2008.

[3] F. Wilson, D. King, M. Willey, R. Aadland, D. Tilley, and K. DeGrys, "Development Status of the BPT Family of Hall Current Thrusters," in *35th Joint Propulsion Conference*, (Los Angeles, CA), pp. AIAA–99–2573, 1999.

[4] J. S. Miller, S. H. Pullins, D. J. Levandier, Y.-H. Chiu, and R. A. Dressler, "Xenon charge exchange cross sections for electrostatic thruster models," *Journal of Applied Physics*, vol. 91, no. 3, pp. 984–991, 2002.

[5] D. Rapp and W. E. Francis, "Charge Exchange between Gaseous Ions and Atoms," *The Journal of Chemical Physics*, vol. 37, p. 2631, Dec. 1962.

[6] S. Sakabe and Y. Izawa, "Cross sections for resonant charge transfer between atoms and their positive ions: Collision velocity less than 1 a.u.," *Atomic Data and Nuclear Data Tables*, vol. 49, pp. 257–314, Nov. 1991.

[7] H. Hagstrum, "Theory of Auger Ejection of Electrons from Metals by Ions," *Physical Review*, vol. 96, pp. 336–365, Oct. 1954.

[8] P. Varga, W. Hofer, and H. Winter, "Auger neutralization of multiply charged noble gas ions at a tungsten surface," *Surface Science*, vol. 117, pp. 142–153, May 1982.

[9] O. Hachenberg and W. Brauer, "Secondary Electron Emission from Solids," *Advances in Electronics and Electron Physics*, vol. 11, pp. 413–499, 1959.

[10] J. Schou, "Transport theory for kinetic emission of secondary electrons from solids," *Physical Review B*, vol. 22, no. 5, 1980.

[11] E. V. Alonso, M. A. Alurralde, and R. A. Baragiola, "Kinetic electron emission from solids induced by slow heavy ions," *Surface Science Letters*, vol. 166, no. 2-3, pp. 155–160, 1986.

[12] M. Rösler, *Particle induced electron emission I.* Springer tracts in modern physics ;v. 122, Berlin/New York: Springer-Verlag, 1991.

[13] G. Wehner, "Energieverteilung der von 2, 5, 10 und 15 keV He- und Ar-Ionen an Molybdän ausgelösten Elektronen," *Zeitschrift für Physik A Hadrons and Nuclei*, vol. 193, no. 3, pp. 439–442, 1966.

[14] M. K. Scharfe, J. W. Koo, and G. M. Azarnia, "DSMC Implementation of Experimentally-Based Xe++ Xe Differential Cross Sections for Electric Propulsion Modeling," in *27th International Symposium on Rarefied Gas Dynamics*, pp. 1085–1090, DTIC Document, 2011.

[15] T. D. Huismann, *Improving Hall Thruster Plume Simulation through Refined Characterization of Near-field Plasma Properties*. PhD thesis, University of Michigan, 2011.

[16] G. A. Bird, *Molecular Gas Dynamics and the Direct Simulation of Gas Flows*. Clarendon, 1994.

[17] C. R. Koppel, F. Marchandise, M. Prioul, D. Estublier, and F. Darnon, "The SMART-1 Electric Propulsion Subsystem around the Moon: In Flight Experience," in *41st AIAA/ASME/SAE/ASEE Joint Propulsion Conference & Exhibit*, (Tucson, AZ), pp. 1–10, 2005.

[18] J. Brophy, M. G. Marcucci, G. B. Ganapath, J. Gates, C. E. Garner, M. Klatte, J. Lo, B. Nakazono, and G. Pixler, "Implementation of the DAWN ion propulsion system," in *41st AIAA/ASME/SAE/ASEE Joint Propulsion Conference & Exhibit*, (Tucson, AZ), pp. AIAA–2005–4071, 2005.

[19] N. Wallace, P. Jameson, C. Saunders, M. Fehringer, C. Edwards, and R. Floberghagen, "The GOCE Ion Propulsion Assembly Lessons Learnt from the First 22 Months of Flight Operations," in *32nd International Electric Propulsion Conference*, (Wiesbaden, Germany), pp. IEPC–2011–327, 2011.

[20] J. P. Squire, C. S. Olsen, F. R. Chang-Díaz, L. D. Cassady, B. W. Longmier, M. G. Ballenger, M. D. Carter, T. W. Glover, G. E. McCaskill, and E. A. Bering, "VASIMR VX-200 Operation at 200 kW and Plume Measurements: Future Plans and an ISS EP Test Platform," in *32nd International Electric Propulsion Conference*, (Wiesbaden, Germany), pp. IEPC–2011–154, 2011.

[21] S. Pullins, R. A. Dressler, Y.-H. Chiu, and D. J. Levandier, "Ion Dynamics in Hall Effect and Ion Thrusters: Xe++ - Xe Symmetric Charge Transfer," in *38th Aerospace Sciences Meeting*, (New York, NY), pp. AIAA–2000–0603, 2000.

[22] R. R. Hofer, I. Katz, I. Mikellides, D. M. Goebel, K. K. Jameson, R. M. Sullivan, and L. K. Johnson, "Efficacy of Electron Mobility Models in Hybrid-PIC Hall Thruster Simulations," *44th AIAA/ASME/SAE/ASEE Joint Propulsion Conference*, pp. AIAA–2008–4924, 2008.

[23] W. A. Hargus and G. Reed, "The Air Force Clustered Hall Thruster Program," *Technical Report*, 2002.

[24] I. Newton, *Philosophiae Naturalis Principia Mathematica*, vol. I–III. Edmond Halley, 1687.

[25] W. Moore, "A Treatise on the Motion of Rockets. To which is added, An Essay on Naval Gunnery," tech. rep., Military Academy at Woolwich, London, 1813.

[26] K. E. Tsiolkovsky, "The exploration of cosmic space by means of reaction devices," *The Science Review*, 1903.

[27] L. Uribarri and E. Y. Choueiri, "Relationship Between Anode Spots and Onset Voltage Hash in Magnetoplasmadynamic Thrusters," *Journal of Propulsion and Power*, vol. 24, no. 3, pp. 571–577, 2008.

[28] V. V. Zhurin, H. R. Kaufman, and R. S. Robinson, "Physics of closed drift thrusters," *Plasma Sources Science and Technology*, vol. 8, pp. R1–R20, Feb. 1999.

[29] R. R. Hofer, *Development and Characterization of High-Efficiency, High-Specific Impulse Xenon Hall Thrusters*. PhD thesis, University of Michigan, 2004.

[30] E. H. Hall, "On a New Action of the Magnet on Electric Currents," *American Journal of Mathematics*, vol. 2, pp. 287–292, Sept. 1879.

[31] E. Y. Choueiri, "Fundamental difference between the two Hall thruster variants," *Physics of Plasmas*, vol. 8, p. 5025, Nov. 2001.

[32] G. A. Bird, "Approach to Translational Equilibrium in a Rigid Sphere Gas," *Physics of Fluids*, vol. 6, no. 10, pp. 1518–1519, 1963.

[33] C. K. Birdsall and A. B. Langdon, *Plasma Physics via Computer Simulation (Series in Plasma Physics)*. Taylor & Francis, 1 ed., Oct. 2004.

[34] J. J. Szabo Jr., *Fully kinetic numerical modeling of a plasma thruster*. PhD thesis, Massachusetts Institute of Technology, 2001.

[35] S. Yoshikawa and D. J. Rose, "Anomalous diffusion of a plasma across a magnetic field," *Physics of Fluids*, vol. 5, p. 334, Mar. 1962.

[36] J. W. Koo and I. D. Boyd, "Modeling of Anomalous Electron Mobility in Hall Thrusters," *Physics of Plasmas*, vol. 13, no. 033501, 2006.

[37] R. E. Wirz, M. I. Patino, and L. E. Chu, "Simple Plasma Experiments for Investigation of Plasma Behavior and Model Validation," *Plasma Sources Science and Technology (submitted)*, 2012.

[38] R. Wirz, M. Patino, and L. Chu, "Ion Neutral Collision Analysis for a Well Characterized Plasma Experiment," in *48th AIAA/ASME/SAE/ASEE Joint Propulsion Conference & Exhibit*, Joint Propulsion Conferences, pp. AIAA–2012–4119, American Institute of Aeronautics and Astronautics, July 2012.

[39] R. E. Wirz, L. Chu, M. Patino, H. Mao, and S. Araki, "Well-Characterized Plasma Experiments for Validation of Computational Models, IEPC-2011-122," in *32nd International Electric Propulsion Conference*, (Wiesbaden, Germany), pp. IEPC–2011–122, 2011.

[40] S. J. Araki and R. E. Wirz, "Collision Modeling for High Velocity Ions in a Quiescent Gas, AIAA 2011-3740," in *42nd AIAA Plasmadynamics and Lasers Conference*, (Honolulu, HI), pp. AIAA–2011–3740, 2011.

[41] S. J. Araki and R. E. Wirz, "Ion-Neutral Collision Modeling Using Classical Scattering with Spin-Orbit Free Interaction Potential," *Journal of Applied Physics (submitted)*, 2012.

[42] I. G. Mikellides, I. Katz, R. R. Hofer, and D. M. Goebel, "Hall-Effect Thruster Simulations with 2-D Electron Transport and Hydrodynamic Ions," in *31st International Electric Propulsion Conference*, (Ann Arbor, MI), pp. IEPC–2009–114, 2009.

[43] I. G. Mikellides, I. Katz, R. R. Hofer, D. M. Goebel, K. de Grys, and A. Mathers, "Magnetic shielding of the channel walls in a Hall plasma accelerator," *Physics of Plasmas*, vol. 18, p. 033501, Mar. 2011.

[44] F. Taccogna, S. Longo, and M. Capitelli, "Very-near-field plume simulation of a stationary plasma thruster," *The European Physical Journal Applied Physics*, vol. 28, pp. 113–122, Oct. 2004.

[45] F. Taccogna, R. Schneider, S. Longo, and M. Capitelli, "Kinetic simulations of a plasma thruster," *Plasma Sources Science and Technology*, vol. 17, p. 024003, May 2008.

[46] I. D. Boyd, "Review of Hall Thruster Plume Modeling," *Journal of Spacecraft and Rockets*, vol. 38, pp. 381–387, May 2001.

[47] I. D. Boyd, L. Garrigues, J. Koo, and M. Keidar, "Progress in development of a combined device/plume model for Hall thrusters," in *36th AIAA Joint Propulsion Conference*, (Huntsville, AL), pp. AIAA–00–3520, American Institute of Aeronautics and Astronautics, 2000.

[48] I. D. Boyd and R. A. Dressler, "Far field modeling of the plasma plume of a Hall thruster," *Journal of Applied Physics*, vol. 92, p. 1764, Aug. 2002.

[49] S. Cheng and M. Martinez-Sanchez, "Comparison of Numerical Simulation to Hall Thruster Plume Shield Experiment," in *40th AIAA/ASME/SAE/ASEE Joint Propulsion Conference and Exhibit*, Joint Propulsion Conferences, pp. AIAA–2004–3635, American Institute of Aeronautics and Astronautics, July 2004.

[50] C. S. Niemela, L. Brieda, M. R. Nakles, J. M. Ekholm, and W. A. Hargus Jr, "Comparison of Hall Thruster Plume Expansion Model with Experimental Data," in *42nd AIAA/ASME/SAE/ASEE Joint Propulsion Conference*, (Sacramento, CA), pp. AIAA–2006–4480, 2006.

[51] I. Boyd, "Numerical Simulation of Hall Thruster Plasma Plumes in Space," *IEEE Transactions on Plasma Science*, vol. 34, pp. 2140–2147, Oct. 2006.

[52] I. D. Boyd and J. T. Yim, "Modeling of the near field plume of a Hall thruster," *Journal of applied physics*, vol. 95, no. 9, p. 4575, 2004.

[53] Y.-H. Chiu, R. A. Dressler, D. J. Levandier, C. Houchins, and C. Y. Ng, "Large-angle xenon ion scattering in Xe-propelled electrostatic thrusters: differential cross sections," *Journal of Physics D: Applied Physics*, vol. 41, p. 165503, Aug. 2008.

[54] R. Dressler, Y.-H. Chiu, O. Zatsarinny, K. Bartschat, R. Srivastava, and L. Sharma, "Near-infrared collisional radiative model for Xe plasma electrostatic thrusters: the role of metastable atoms," *Journal of Physics D: Applied Physics*, vol. 42, p. 185203, Sept. 2009.

[55] I. G. Mikellides, I. Katz, R. A. Kuharski, and M. J. Mandell, "Elastic scattering of ions in electrostatic thruster plumes," *Journal of Propulsion and Power*, vol. 21, no. 1, pp. 111–118, 2005.

[56] T. D. Huismann and I. D. Boyd, "Improving Hall-thruster Plume Simulation through Investigation of the Near-field Environment," in *International Electric Propulsion Conference*, (Wiesbaden, Germany), pp. IEPC–2011–227, 2011.

[57] K. K. Jameson, *Investigation of Hollow Cathode Effects on Total Thruster Efficiency in a 6 kW Hall Thruster*. PhD thesis, UCLA, 2008.

[58] B. M. Reid, *The Influence of Neutral Flow Rate in the Operation of Hall Thrusters*. PhD thesis, The University of Michigan, 2009.

[59] E. Teloy and D. Gerlich, "Integral cross sections for ionmolecule reactions. I. The guided beam technique," *Chemical Physics*, vol. 4, pp. 417–427, June 1974.

[60] P. N. Giuliano and I. D. Boyd, "Analysis of a plasma test cell including non-neutrality and complex collision mechanisms," in *48th AIAA/ASME/SAE/ASEE Joint Propulsion Conference*, (Atlanta, GA), pp. AIAA–2012–3736, 2012.

[61] G. D. Hobbs and J. A. Wesson, "Heat flow through a Langmuir sheath in the presence of electron emission," *Plasma Physics*, vol. 9, pp. 85–87, Jan. 1967.

[62] E. Ahedo, "Presheath/sheath model with secondary electron emission from two parallel walls," *Physics of Plasmas*, vol. 9, no. 10, pp. 4340–4347, 2002.

[63] F. Taccogna, S. Longo, and M. Capitelli, "Plasma-surface interaction model with secondary electron emission effects," *Physics of Plasmas*, vol. 11, no. 3, p. 1220, 2004.

[64] L. Garrigues, G. J. M. Hagelaar, C. Boniface, and J. P. Boeuf, "Anomalous conductivity and secondary electron emission in Hall effect thrusters," *Journal of Applied Physics*, vol. 100, p. 123301, Dec. 2006.

[65] Y. Raitses, A. Smirnov, D. Staack, and N. J. Fisch, "Measurements of secondary electron emission effects in the Hall thruster discharge," *Physics of Plasmas*, vol. 13, p. 014502, Jan. 2006.

[66] D. Sydorenko, a. Smolyakov, I. Kaganovich, and Y. Raitses, "Kinetic simulation of secondary electron emission effects in Hall thrusters," *Physics of Plasmas*, vol. 13, no. 1, p. 014501, 2006.

[67] E. Ahedo and V. De Pablo, "Combined effects of electron partial thermalization and secondary emission in Hall thruster discharges," *Physics of Plasmas*, vol. 14, no. 8, p. 083501, 2007.

[68] J. J. Boerner, *Computational simulation of Faraday probe measurements*. PhD thesis, University of Michigan, 2008.

[69] M. L. R. Walker, "Ion Collection in Hall Thruster Plumes," *Journal of propulsion and power*, vol. 22, no. 1, 2006.

[70] D. Hasselkamp, *Particle induced electron emission II*. Springer tracts in modern physics ;v. 123, Berlin/New York: Springer-Verlag, 1992.

[71] R. Baggett, W. Hulgan, J. Dankanich, and R. Bachtel, "In-Space Propulsion Solar Electric Propulsion Program Overview of 2006," in *42nd AIAA/ASME/SAE/ASEE Joint Propulsion Conference & Exhibit*, Joint Propulsion Conferences, pp. AIAA–2006–4463, July 2006.

[72] Y. N. Demkov, "Quantum-mechanical calculation of the probability of charge-exchange in collisions," *Scientific Notes, Leningrad State University*, vol. 146, no. 8, p. 74, 1952.

[73] Y. N. Demkov, "Charge Exchange with Small Energy Transfer," in *The Proceedings of the 3rd International Conference on the Physics of Electronic and Atomic Collisions* (M. R. C. McDowell, ed.), (London, England), pp. 831–838, North-Holland, 1964.

[74] A. Dalgarno, "The Mobilities of Ions in their Parent Gases," *Philosophical Transactions of the Royal Society of London. Series A, Mathematical and Physical Sciences*, vol. 250, no. 982, pp. 426–439, 1958.

[75] A. Dalgarno, M. R. C. McDowell, and A. Williams, "The Mobilities of Ions in Unlike Gases," *Philosophical Transactions of the Royal Society of London. Series A, Mathematical and Physical Sciences*, vol. 250, pp. 411–425, Apr. 1958.

[76] M. S. Child, *Molecular Collision Theory*. Academic Press, 1974.

[77] H. D. Hagstrum, "Instrumentation and Experimental Procedure for Studies of Electron Ejection by Ions and Ionization by Electron Impact," *Review of Scientific Instruments*, vol. 24, p. 1122, Dec. 1953.

[78] H. Hagstrum, "Auger Ejection of Electrons from Tungsten by Noble Gas Ions," *Physical Review*, vol. 96, pp. 325–335, Oct. 1954.

[79] H. Hagstrum, "Auger Ejection of Electrons from Molybdenum by Noble Gas Ions," *Physical Review*, vol. 104, pp. 672–683, Nov. 1956.

[80] H. Hagstrum, "Metastable Ions of the Noble Gases," *Physical Review*, vol. 104, pp. 309–316, Oct. 1956.

[81] H. Hagstrum, "Effect of Monolayer Adsorption on the Ejection of Electrons from Metals by Ions," *Physical Review*, vol. 104, pp. 1516–1527, Dec. 1956.

[82] H. D. Hagstrum, "Low energy de-excitation and nuetralization processes near surfaces," in *Inelastic Ion-Surface Collisions* (N. H. Tolk, J. C. Tully, W. Heiland, and C. W. White, eds.), ch. 1, p. 89, New York: Academic Press, 1977.

[83] H. D. Hagstrum, "Studies of Adsorbate Electronic Structure Using Ion Neutralization and Photoemission Spectroscopies," in *Electron and Ion Spectroscopy of Solids* (L. Fiermans, J. Vennik, and W. Dekeyser, eds.), p. 273, New: Plenum Press, 1978.

[84] L. M. Kishinevskii, "Estimation of electron potential emission yield dependence on metal and ion parameters," *Radiation Effects*, vol. 19, pp. 23–27, Jan. 1973.

[85] R. A. Baragiola, E. V. Alonso, J. Ferron, and A. Oliva-Florio, "Ion-induced electron emission from clean metals," *Surface Science*, vol. 90, pp. 240–255, Dec. 1979.

[86] W. M. Haynes and D. R. Lide, eds., *CRC Handbook of Chemistry and Physics*. CRC Press, 92nd ed., 2012.

[87] M. K. Covo, A. Molvik, A. Friedman, G. Westenskow, J. Barnard, R. Cohen, P. Seidl, J. Kwan, G. Logan, D. Baca, F. Bieniosek, C. Celata, J.-L. Vay, and J. Vujic, "Beam energy scaling of ion-induced electron yield from K+ impact on stainless steel," Tech. Rep. 6, Lawrence Berkeley National Laboratory, Berkeley, CA, June 2006.

[88] W. Sesselmann, B. Woratschek, J. Küppers, G. Ertl, and H. Haberland, "Auger neutralization spectroscopy of clean and adsorbate-covered transition-metal surfaces by deexcitation of metastable noble-gas atoms," *Physical Review B*, vol. 35, pp. 8348–8359, June 1987.

[89] W. Sesselmann, B. Woratschek, J. Küppers, G. Ertl, and H. Haberland, "Interaction of metastable noble-gas atoms with transition-metal surfaces: Resonance ionization and Auger neutralization," *Physical Review B*, vol. 35, pp. 1547–1559, Feb. 1987.

[90] E. Hood, F. Bozso, and H. Metiu, "A simple phenomenological model for the interpretation of ion neutralization spectra," *Surface Science*, vol. 161, pp. 491–512, Oct. 1985.

[91] P. Varga, W. Hofer, and H. Winter, "Ion Neutralization of Multiply Charged Particles near a Surface," *Journal of Scanning Electron Microscopy*, vol. 1, pp. 967–971, 1982.

[92] B. Sinkovic, E. Shekel, and S. L. Hulbert, "Spin-resolved iron surface density of states," *Physical Review B*, vol. 52, no. 12, pp. 8696–8699, 1995.

[93] S. Davison, *Basic theory of surface states*. New York: Clarendon Press, 1996.

[94] M. Abramowitz and I. A. Stegun, *Handbook of Mathematical Functions*. Dover Publications, 1965.

[95] P. Villard, "The positive charges carried by the canal rays," *Journal de Physique*, vol. 3, no. 8, p. 1, 1899.

[96] J. J. Thomson, "On the positive electrification of a rays, and the emission of slowly moving cathode rays by radio-active substances," in *Proceedings of the Cambridge Philosophical Society*, p. 49, 1904.

[97] E. Rutherford, "Charge carried by the α and β Rays of Radium," *Philosophical Magazine*, p. 193, 1905.

[98] B. A. Brusilovsky, "Kinetic ion-induced electron emission from the surface of random solids," *Applied Physics A: Materials Science & Processing*, vol. 50, pp. 111–129, 1990.

[99] H. Winter and J. Burgdörfer, *Slow heavy-particle induced electron emission from solid surfaces*. Springer tracts in modern physics,0081-3869 ;v. 225, Berlin ; New York: Springer, 2007.

[100] E. Alonso, R. Baragiola, J. Ferrón, M. Jakas, and A. Oliva-Florio, "Z_{1} dependence of ion-induced electron emission from aluminum," *Physical Review B*, vol. 22, pp. 80–87, July 1980.

[101] R. Baragiola, E. Alonso, and A. Florio, "Electron emission from clean metal surfaces induced by low-energy light ions," *Physical Review B*, vol. 19, pp. 121–129, Jan. 1979.

[102] J. Lindhard and M. Scharff, "Energy Dissipation by Ions in the keV Region," *Physical Review*, vol. 124, pp. 128–130, Oct. 1961.

[103] O. B. Duchemin, *An Investigation of Ion Engine Erosion by Low Energy Sputtering*. PhD thesis, California Institute of Technology, 2001.

[104] H. A. Bethe, "On the theory of secondary emission," *Physical Review*, vol. 59, p. 940, 1941.

[105] J. C. Ashley, C. J. Tung, R. H. Ritchie, and V. E. Anderson, "Calculations of mean free paths and stopping powers of low energy electrons (10 keV) in solids using a statistical model," *IEEE Transactions on Nuclear Science*, vol. 23, pp. 1833–1837, Dec. 1976.

[106] H. Salow, "Sekundarelektronen-emission," *Physik Zeitschrift*, vol. 41, p. 434, 1940.

[107] E. J. Sternglass, "Theory of secondary electron emission by high-speed ions," *Physical Review*, vol. 108, no. 1, 1957.

[108] E. S. Parilis and L. M. Kishinevskii, "Kinetic Secondary Electron Ejection from Molybdenum by Cesium Ions," *Soviet Phys.-Solid State*, vol. 3, p. 885, 1960.

[109] J. Schou, "Secondary Electron Emission From Solids by Electron and Proton Bombardment," *Scanning Microscopy*, vol. 2, no. 2, pp. 607–632, 1988.

[110] H. Winter, F. Aumayr, and G. Lakits, "Recent advances in understanding particle-induced from metal surfaces," *Nuclear Instruments and Methods in Physics Research B*, vol. 58, pp. 301–308, 1991.

[111] G. Lakits and H. Winter, "Electron emission from metal surfaces bombarded by slow neutral and ionized particles," *Nuclear Instruments and Methods in Physics Research B*, vol. 48, pp. 597–603, 1990.

[112] G. Lakits, A. Arnau, and H. Winter, "Slow-particle-induced kinetic electron emission from a clean metal surface: A comparison for neutral and ionized projectiles," *Physical Review B*, vol. 42, no. 1, pp. 15–24, 1990.

[113] H. J. Frischkorn and K. O. Groeneveld, "Heavy Ion Induced Electron Emission from Solid Surfaces," *Physica Scripta*, vol. T6, pp. 89–93, Jan. 1983.

[114] N. Benazeth, "Review on kinetic ion-electron emission from solid metallic targets," *Nuclear Instruments and Methods in Physics Research*, vol. 194, pp. 405–413, Mar. 1982.

[115] E. W. Weisstein, "Regularized Hypergeometric Function, http://mathworld.wolfram.com/RegularizedHypergeometricFunction.html," 2012.

[116] C. Ramsauer, "Über den Wirkungsquerschnitt der Gasmoleküle gegenüber langsamen Elektronen. II. Fortsetzung und Schluß," *Annalen der Physik*, vol. 377, no. 21, pp. 345–352, 1923.

[117] C. Ramsauer and R. Kollath, "Über den Wirkungsquerschnitt der Edelgasmoleküle gegenüber Elektronen unterhalb 1 Volt," *Annalen der Physik*, vol. 395, no. 4, pp. 536–564, 1929.

[118] M. Dababneh, W. Kauppila, J. Downing, F. Laperriere, V. Pol, J. Smart, and T. Stein, "Measurements of total scattering cross sections for low-energy positrons and electrons colliding with krypton and xenon," *Physical Review A*, vol. 22, pp. 1872–1877, Nov. 1980.

[119] S. Dietrich and I. D. Boyd, "Scalar and Parallel Optimized Implementation of the Direct Simulation Monte Carlo Method," *Journal of Computational Physics*, vol. 126, no. 2, pp. 328–342, 1996.

[120] C. Cai, *Theoretical and Numerical Studies of Plume Flows in Vacuum Chambers*. Phd dissertation, University of Michigan, 2005.

[121] Y. Choi, *Modeling an anode layer Hall thruster and its plume*. Doctoral dissertation, University of Michigan, 2008.

[122] G. A. Bird, "Monte-Carlo simulation in an engineering context," *Progress in Astronautics and Aeronautics*, vol. 74, pp. 239–255, 1981.

[123] G. A. Bird, "Recent advances and current challenges for DSMC," *Computers & Mathematics with Applications*, vol. 35, no. 1, pp. 1–14, 1998.

[124] E. S. Oran, C. K. Oh, and B. Z. Cybyk, "Direct Simulation Monte Carlo: Recent Advances and Applications," *Annual Review of Fluid Mechanics*, vol. 30, pp. 403–441, Jan. 1998.

[125] G. A. Bird, "Forty years of DSMC, and now?," *AIP Conference Proceedings*, vol. 585, pp. 372–380, Aug. 2001.

[126] L. Boltzmann, "Weitere Studien über das Wärmegleichgewicht unter Gasmolekülen," *Wiener Berichte*, vol. 66, pp. 275–370, 1872.

[127] L. Boltzmann, *Über einige fragen der kinetischen gastheorie*. Wien, 1887.

[128] G. A. Bird, "Direct Simulation and the Boltzmann Equation," *Physics of Fluids*, vol. 13, p. 2676, Nov. 1970.

[129] S. Olson and A. Christlieb, "Gridless DSMC," *Journal of Computational Physics*, vol. 227, pp. 8035–8064, Sept. 2008.

[130] J. Dawson, "Particle simulation of plasmas," *Reviews of Modern Physics*, vol. 55, pp. 403–447, Apr. 1983.

[131] C. K. Birdsall, "Particle-in-cell charged-particle simulations, plus Monte Carlo collisions with neutral atoms, PIC-MCC," *Plasma Science, IEEE Transactions on*, vol. 19, no. 2, pp. 65–85, 1991.

[132] D. B. VanGilder, G. I. Font, and I. D. Boyd, "Hybrid Monte Carlo - Particle-in-Cell Simulation of an Ion Thruster Plume," in *International Electric Propulsion Conference*, pp. IEPC–97–182, 1997.

[133] S. Roy and B. Pandey, "Plasma-wall interaction inside a hall thruster," *Journal of Plasma Physics*, vol. 68, no. 4, pp. 305–319, 2002.

[134] J. W. Koo, *Hybrid PIC-MCC Computational Modeling of Hall Thrusters*. Doctoral dissertation, University of Michigan, 2005.

[135] J. D. Huba, *NRL Plasma Formulary*. The Office of Naval Research, 2011.

[136] P. N. Giuliano and I. D. Boyd, "Particle simulation of collision dynamics for ion beam injection into a rarefied gas," *Physics of Plasmas (submitted)*, 2012.

[137] P. N. Giuliano and I. D. Boyd, "Effects of detailed charge exchange interactions in DSMC-PIC simulation of a simplified plasma test cell," in *32nd International Electric Propulsion Conference*, (Wiesbaden, Germany), pp. IEPC–2011–112, 2011.

[138] W. H. Press, S. A. Teukolsky, W. T. Vetterling, and B. P. Flannery, *Numerical Recipes in C: The Art of Scientific Computing*. Cambridge University Press, 2 ed., Nov. 1992.

[139] K. Roach, "Hypergeometric function representations," in *Proceedings of the 1996 international symposium on Symbolic and algebraic computation*, ISSAC '96, (New York, NY, USA), pp. 301–308, ACM, 1996.

[140] J. Pearson, *Computation of Hypergeometric Functions*. Masters dissertation, University of Oxford, 2009.

[141] M. Furman and M. Pivi, "Probabilistic model for the simulation of secondary electron emission," *Physical Review Special Topics - Accelerators and Beams*, vol. 5, pp. 124404–, Dec. 2002.